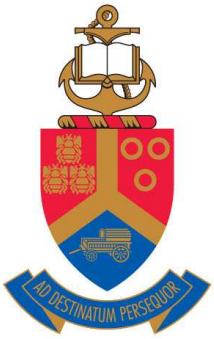

UNIVERSITEIT VAN PRETORIA
UNIVERSITY OF PRETORIA
YUNIBESITHI YA PRETORIA

INDUSTRIAL AND OFFICE WIDEBAND MIMO CHANNEL PERFORMANCE

LR NAIR

2009

INDUSTRIAL AND OFFICE WIDEBAND MIMO CHANNEL PERFORMANCE

By

Lakshmi Ravindran Nair

Study leader: Dr BTJ Maharaj (University of Pretoria, South Africa)

Submitted in partial fulfillment of the requirements for the degree

Master of Engineering (Electronic)

in the

Department of Electrical, Electronic & Computer Engineering

in the

School of Engineering

in the

Faculty of Engineering, Built Environment & Information Technology

UNIVERSITY OF PRETORIA

March 2009

SUMMARY

INDUSTRIAL AND OFFICE WIDEBAND MIMO CHANNEL PERFORMANCE

by

Lakshmi Ravindran Nair

Study leader: Dr BTJ Maharaj (University of Pretoria, South Africa)

Department of Electrical, Electronic & Computer Engineering

Master of Engineering (Electronic)

The aim of this dissertation is to characterize the MIMO channel in two very distinct indoor scenarios: an office building and an industrial environment. The study investigates the use of single- and dual-polarized antenna MIMO systems, and attempts to model the channel using well-known analytical models. The suitability of MIMO architectures employing either single- or dual-polarization antennas is presented, with the purpose of identifying not only which architecture provides better average capacity performance, but also which is more robust for avoiding low channel rank. A measurement campaign employing dual-polarized 8×8 patch arrays at 2.4 GHz and 5.2 GHz is analyzed. For both environments the performance of three 4×4 subsystems (dual-polarized, vertical-polarized and horizontal-polarized) are compared in terms of the average capacities attained by these systems and their eigenvalue distributions. Average capacities are found to be only marginally different, indicating little advantage of dual-polarized elements for average performance. However, an eigenvalue analysis indicates that the dual-polarized system is most robust for full-rank MIMO communications, by providing orthogonal channels with more equal gain. The analysis of the analytical models shows that the Kronecker and Weichselberger models underestimate the measured data. Kronecker models are known to perform poorly for large antenna sizes and the performance of the Weichselberger model can be attributed to certain parts of the channel not fading enough.

Keywords:

MIMO systems, Polarization, Average capacity, Eigenvalue analysis, Robustness, Analytical models.

OPSOMMING

INDUSTRIAL AND OFFICE WIDEBAND MIMO CHANNEL PERFORMANCE

deur

Lakshmi Ravindran Nair

Studieleier: Dr BTJ Maharaj (University of Pretoria, South Africa)

Departement Elektriese, Elektroniese & Rekenaar Ingenieurswese

Meester in Ingenieurswese (Elektronies)

Die doel van hierdie studie is om ’n VIVU kanaal te karakteriseer in twee verskillende interieur omgewings nl: kantoor gebou en industriële opset. Die studie bestudeer die gebruik van enkel- en bi-gepolariseerde antenna VIVU stelsels en poog om die kanaal te modelleer deur gebruik te maak van bekende analitiese modelle. Die geskiktheid van VIVU strukture met enkel- en bi-gepolariseerde antennas word voorgestel met die doel om nie net die struktuur te identifiseer wat die beste gemiddelde kapasiteit gee nie, maar ook wat die meeste robuust is om lae kanaal rang te vermy. ’n Metings proses wat bi-gepolariseerde 8×8 laslap strukture gebruik teen 2.4 GHz en 5.2 GHz word ge-analiseer. Vir beide omgewings word die prestasie van drie 4×4 sub-stelsels (bi-gepolariseerd, vertikaal gepolariseerd en horisontaal gepolariseerd) vergelyk in terme van die gemiddelde kapasiteit wat bereik is deur die stelsels en hulle eigenwaarde distribusies. Dis bevind dat die gemiddelde kapasiteit net marginaal verskil, wat dui op ’n klein voordeel ten opsigte van bi-gepolariseerde elemente vir gemiddelde prestasie. Eigenwaarde analise dui egter daarop dat die bi-geploariseerde stelsel mees robuust is vir volle rang VIVU kommunikasie deur ortogonale kanale met meer gelyke versterking te verskaf. Die modelle analise wys dat die Kronecker en Weichselberger modelle die metings data onderskat. Kronecker modelle is bekend vir hulle swak prestasie ten opsigte van groot antenna groottes en die prestasie van die Weichselberger model is gevolg van sekere dele van die kanaal wat nie genoeg attenueer nie.

Sleutelwoorde:

VIVU sisteme, Polarisasie, Gemiddelde kapasiteit, Eigenwaarde ontleding, Robuustheid, Analitiese modelle.

To all those who have supported and motivated me through my years of study

ACKNOWLEDGEMENTS

Firstly I would like to express my gratitude to my supervisor, Dr. Sunil Maharaj, for giving me the opportunity to work in this upcoming and exciting field of Multiple-Input Multiple-Output wireless systems, and without whose constant guidance and motivation the completion of this dissertation would not have been possible.

Secondly, to Prof. Jon Wallace, of Jacobs University, Bremen, Germany, for finding time in his busy schedule to advise me on the work I was doing. His invaluable insight in this field equipped me with the information necessary to ensure successful completion of this dissertation.

Thirdly, to my parents for having always been a pillar of strength, and for never allowing me to lose faith in myself.

Last, but not least, to my husband, Aravind, for his patience and understanding these last few years.

CONTENTS

List of Abbreviations

1-D	One-dimensional
2-D	Two-dimensional
3-D	Three-dimensional
3GPP	3rd Generation Partnership Project
5-D	Five-dimensional
AM	Amplitude Modulation
AoA	Angle of Arrival
AoD	Angle of Departure
AWGN	Additive White Gaussian Noise
BPSK	Binary Phase Shift Keying
CCDF	Complementary Cumulative Distribution Function
CDF	Cumulative Distribution Function
CDMA	Code-Division Multiple Access
CEFIM	Carl and Emily Fuchs Institute of Microelectronics
COST	European Cooperation in the Field of Scientific and Technical Research
dB	Decibels
DCM	Directional Channel Model
DoA	Direction of Arrival
DoD	Direction of Departure
EMI	Electromagnetic Interference
ESV	Extended Saleh Valenzuela
FM	Frequency Modulation
GBSM	Geometry Based Stochastic Model
HML	Heavy Machinery Lab
H-pol	Horizontal polarization

IEEE	Insitute of Electrical and Electronic Engineers
i.i.d.	independent and identically distributed
LOS	Line of Sight
MIMO	Multiple-Input Multiple-Output
MISO	Multiple-Input Single-Output
MPC	Multipath Component
NLOS	Non-Line of Sight
OFDM	Orthogonal Frequency-Division Multiplexing
PDF	Probability Density Function
RF	Radio Frequency
RFID	Radio Frequency Identification
RMSE	Root Mean Square Error
Rx	Receiver
SCM	Spatial Channel Model
SIMO	Single-Input Multiple-Output
SINR	Signal to Interference and Noise Ratio
SISO	Single-Input Single-Output
SNR	Signal-To-Noise Ratio
TDMA	Time-Division Multiple Access
Tx	Transmitter
ULA	Uniform Linear Array
VCR	Virtual Channel Representation
VOIP	Voice Over Internet Protocol
V-pol	Vertical polarization
WCDMA	Wideband Code-Division Multiple Access
WiFi	Wireless Fidelity
WiMax	Worldwide Interoperability for Microwave Access
WLAN	Wireless Local Area Network
XPD	Cross-Polarization Discrimination Factor

LIST OF FIGURES

LIST OF TABLES

CHAPTER ONE

RESEARCH OVERVIEW

1.1 INTRODUCTION

Increasing demand for bandwidth and the development of wireless communication systems for higher data rate transmission and high quality information exchange has sparked interest in the use of MIMO (Multiple-Input Multiple-Output) systems for wireless communication.

MIMO systems consist of multiple antennas at the transmitter (Tx) and the receiver (Rx), which take advantage of multipath signals, making them carry more information by sending and receiving multiple data signals over the same frequency channel. MIMO systems are thus multidimensional and by sending multiple signals across the channel, spectral efficiency is improved which in turn improves capacity, range and reliability.

The increasing use of wireless technologies in homes and businesses has resulted in high interest in MIMO architectures for indoor environments. Although indoor propagation has been studied extensively (both from analytical and experimental perspectives) relatively few studies consider MIMO systems in industrial environments [9]- [11].

The deployment of wireless systems in industrial environments can lead to savings compared to wired networks due to swift deployment, easier maintenance and reconfigurability. However, wireless communications in industrial environments may be more challenging due to factors such as:

- high temperatures and vibration,

- signal obstruction due to heavy machinery,
- large coverage areas for communicating nodes, and
- higher levels of electromagnetic interference.

Industrial applications are also expected to be more demanding [12], requiring a high degree of robustness, reliability, and efficiency.

Propagation within buildings is strongly influenced by the structure of the building, the layout of the rooms, the type of construction materials used [13], objects within the building, etc. Industrial environments contain an abundance of metallic scatterers, which can result in dense multipath scattering. It is important to investigate the behavior of the MIMO channel in industrial environments so that incorrect assumptions of the channel are not made when assessing the potential performance. Therefore, the focus of this work is to identify any differences for MIMO systems in office and industrial environments, as well as to identify array types that are robust to random channel conditions. Since dual-polarized (dual-pol) MIMO systems are more robust to low multipath and random array orientation, they are obvious candidates for demanding industrial applications. This study presents the results of investigations that were conducted in an office and an industrial environment, based on wideband measurements recorded at 2.4 GHz and 5.2 GHz using dual-pol antenna arrays.

1.2 RESEARCH SCOPE

In order to characterize the wideband MIMO channel, data obtained from measurement campaigns conducted at the University of Pretoria in an office and industrial environment are analyzed. The measurements were conducted at 2.4 GHz and 5.2 GHz with an 8×8 MIMO system, employing a linear dual-pol patch array, at different locations within the two environments and for different antenna orientations.

The scope of the work done for this dissertation encompasses the following:

1. Obtaining data from measurements that were carried out in the two environments.
2. Normalizing the channel matrices.

3. Determining channel capacities at the different frequencies, locations, orientations, and polarizations.

4. Determining the effect of polarization on the performance of the MIMO system.

5. Establishing which polarization subsystems are more robust.

6. Establishing the effect of frequency scaling.

7. Comparing the capacities obtained in the two environments.

8. Fitting the measured data to the following models:

   (a) i.i.d. Gaussian model,

   (b) Kronecker product model, and

   (c) the Weichselberger model.

From the results obtained, conclusions about the performance of a MIMO system in an industrial and office environment will be established.

1.3 RESEARCH CONTRIBUTION

Observations of the channel performance under different conditions and the development of the various models will provide researchers with a better understanding of the MIMO propagation channel in an indoor, industrial type environment. Furthermore, considering that no previous detailed analysis, similar to the one motivated above has been done to characterize MIMO channels in industrial scenarios, this research will provide invaluable information that will contribute to reliable and efficient MIMO systems being developed to meet industrial needs.

1.4 ORGANIZATION OF THE DISSERTATION

The dissertation is organized into seven chapters wherein the performance of the MIMO system is established.

Chapter 2 reviews the development of MIMO systems. The advantages of MIMO systems, especially in terms of the capacities they achieve, as well as various applications and MIMO

standards are discussed. Studies based on the use of polarization diversity with MIMO systems are also described, specifically focusing on dual-polarization.

In Chapter 3 various MIMO channel models and measurement techniques are discussed, with emphasis being placed on the Kronecker and Weichselberger models.

An overview of the measurement campaign is presented in Chapter 4. A brief description of the MIMO channel sounder used for making the channel measurements is provided and the extraction and processing of the measured data for use in calculations are discussed. The two environments in which the measurements are carried out are described in terms of their structure, the materials in the environments and the position of the receiver and the transmitter of the MIMO system. The normalization, capacity and correlation equations used for the analysis of the data are also provided.

In Chapter 5 comparisons between the two environments are made. Firstly, the average capacities in the two environments are compared to determine whether the performance of the MIMO system in one environment is better than the other. Following that, comparisons are made between the single-polarization (single-pol) elements of the MIMO system and the dual-pol elements to determine whether there is an advantage when using dual-pol systems. Comparisons between the different orientations of the receiver and the transmitter are made to determine the effect of scattering in the environments. Finally, the effect of the center frequency on the performance of the MIMO system in the two environments are established and the effect, if any, of frequency scaling is also determined.

The results of the Kronecker and Weichselberger modeling are presented in Chapter 6. The Cumulative Distribution Function (CDF) of the average capacities of the models are compared with that of the measured data, and the 8×8 i.i.d. Gaussian model. The results of the models are also fitted to the measured data.

Chapter 7 concludes the dissertation with a summary of the work covered in this study and highlighting the most significant results. Some suggestions for future work are also provided.

CHAPTER TWO
MIMO COMMUNICATION

This chapter describes the development of the MIMO system and its impact on wireless systems, with emphasis being placed on the capacity performances of such a system and the effect of polarization diversity.

2.1 AN OVERVIEW OF MIMO TECHNOLOGY

Signals traveling from a transmitter to a receiver do not necessarily travel in a straight line. Instead, as a result of reflections from large objects, diffraction of electromagnetic waves around objects and signal scattering, signals can take multiple paths to the receiver [14].

Traditional radio systems consider multipath signals as wasteful and/or harmful, and neither do anything to combat the multipath interference, expecting the main signal to outperform the interfering copies, or employ multipath mitigation techniques [1] such as:

- using antennas to capture the strongest signal at each moment in time, or
- adding different delays to the received signals to force the peaks and troughs back into alignment.

However, recent studies have shown that multipath propagation can increase the capacity of a wireless communication system, provided that multiple antennas are used at the receiver and/or the transmitter [15, 16]. Multiple antenna structures can be divided into three groups: multiple antennas only at the receiver, or SIMO[1]; multiple antennas at the transmitter, or MISO[2]; and

[1] Single-Input Multiple-Output
[2] Multiple-Input Single-Output

multiple antennas at both the transmitter and the receiver, or MIMO[3].

When "smart" signal processing is applied to the above antenna structures, these smart antennas improve the performances and techniques of wireless systems. However, the smart antenna systems are one dimensional (1-D), transmitting one data stream per channel and offering only improvements of 1 b/s/Hz or 2 b/s/Hz at a time.

Different types of smart antenna techniques are discussed below [17].

- Selection diversity: multiple antennas with overlapping coverage are used at the receiver as shown in Figure 2.1. The antenna with the highest received power is then chosen as this mitigates fading. This is a simple SIMO technique requiring only one RF[4] link. However it does not use all the energy available at the antennas and interference suppression is limited.

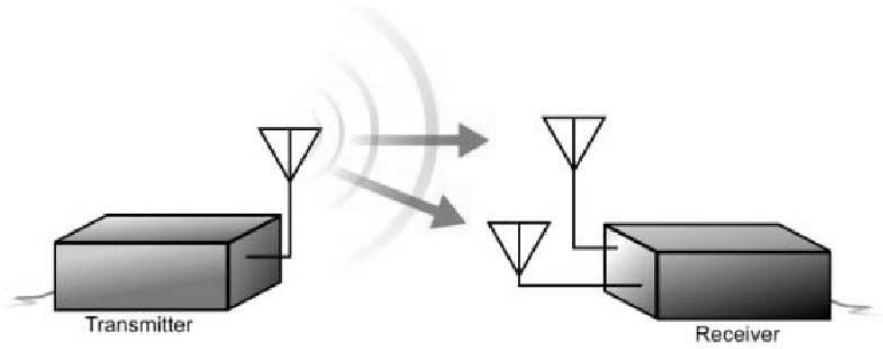

FIGURE 2.1: Selection diversity uses multiple receiver antennas to capture the best multipath signal [1].

- Switched multi-beam (phased array systems): arrays with multiple fixed beams are used at the transmitter as shown in Figure 2.2. With the beams pointing in different directions, the receiver then picks the beam with the highest SNR[5]. This is a MISO system using basic signal processing and the receiver only needs to search for the correct beam every few seconds.

- Adaptive array (adaptive beamforming): multiple antennas are used at the transmitter

[3] Multiple-Input Multiple-Output
[4] Radio Frequency
[5] Signal-To-Noise Ratio

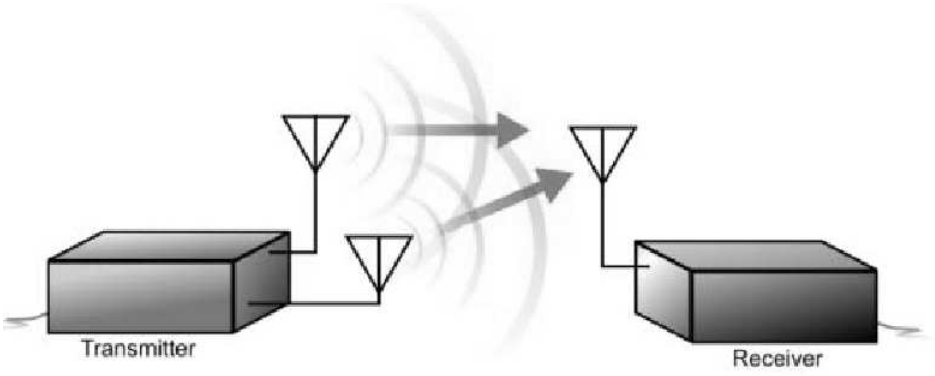

FIGURE 2.2: Beamforming employs multiple transmitter antennas to deliver the best multipath signal [1].

and receiver as shown in Figure 2.3. The signals reached by each antenna are weighted and combined to improve the output signal performance. In reality only a single signal is sent over one channel with the system requiring m complete RF chains and the weight calculation requires more computational complexity.

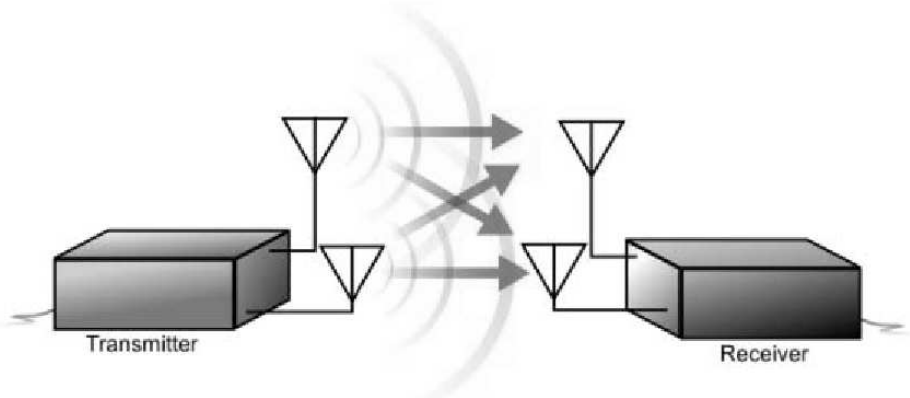

FIGURE 2.3: Combination of beamforming and diversity [1].

As shown in Figure 2.4, MIMO systems make smart antennas multi-dimensional by allowing multiple data streams in the same channel. Signals are therefore transmitted from each of the transmitter antennas and the receiver then weighs and combines the received signal in m (where m is the number of transmitters) different ways in order to obtain each signal. Although the data rate can increase m-fold for the same transmitting power and bandwidth, it is dependent on the richness of the multipath environment.

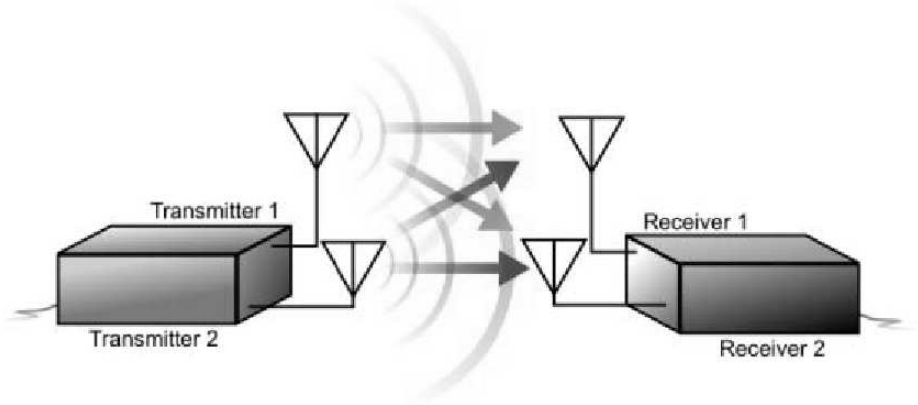

FIGURE 2.4: MIMO systems using multiple transmitters and multiple receivers [1].

The transmission of multiple data streams enables multipath signals to carry more information over the same frequency channel. This results in a linear increase in spectral efficiency rather than the logarithmic increases obtained in traditional systems using just receiver or no diversity [18]. The high spectral efficiency attained by a MIMO system is achieved by the fact that in a rich scattering environment, independent transmission paths for the signals are provided from each transmitter to each receiver. The signals from each individual transmitter thus appear highly uncorrelated at each of the receiving antennas [19]. The signals corresponding to each individual transmitter have different spatial signatures. The receiver can then use these differences to separate the signatures from the different transmitters [18], simultaneously and at the same frequency .

The improvement in MIMO performance can be attributed to the following [2, 3].

- Array gain: results in an increase in the average receiver SNR and is made available through processing at the transmitter and the receiver.
- Diversity gain: reduces fading in the wireless link by transmitting the signal over multiple (ideally) independent fading paths in time/frequency/space. Spatial diversity is used in MIMO systems and space-time coding is used to extract spatial diversity in the absence of channel knowledge at the transmitter by using suitably designed transmitting signals.
- Spatial multiplexing gain: results in the linear increase in capacity $(\min(Tx, Rx))$ for no additional power or bandwidth, and is realized by transmitting independent data signals from individual antennas. In a rich scattering environment the receiver can separate the different streams yielding the linear increase in capacity.

- Interference reduction: because multiple antennas are used, differentiation between spatial signatures of the desired signal and co-channel signals can be exploited to reduce interference. Therefore co-channel interference due to frequency re-use does not occur.

It is not possible to use these enhancements simultaneously due to conflicting demands on the number of antennas used. The degree to which these conflicts are resolved depends on the signaling scheme and the transceiver's design.

MIMO technology is currently the only advanced antenna technology that simultaneously offers high bandwidth, improved coverage, and high mobility at low cost [2, 20]. The capacity gains by MIMO systems have been so enormous, that even the possibility of 1 Gb/s wireless links are becoming possible (Figure 2.5). The next section shows how this improvement in capacity is achieved.

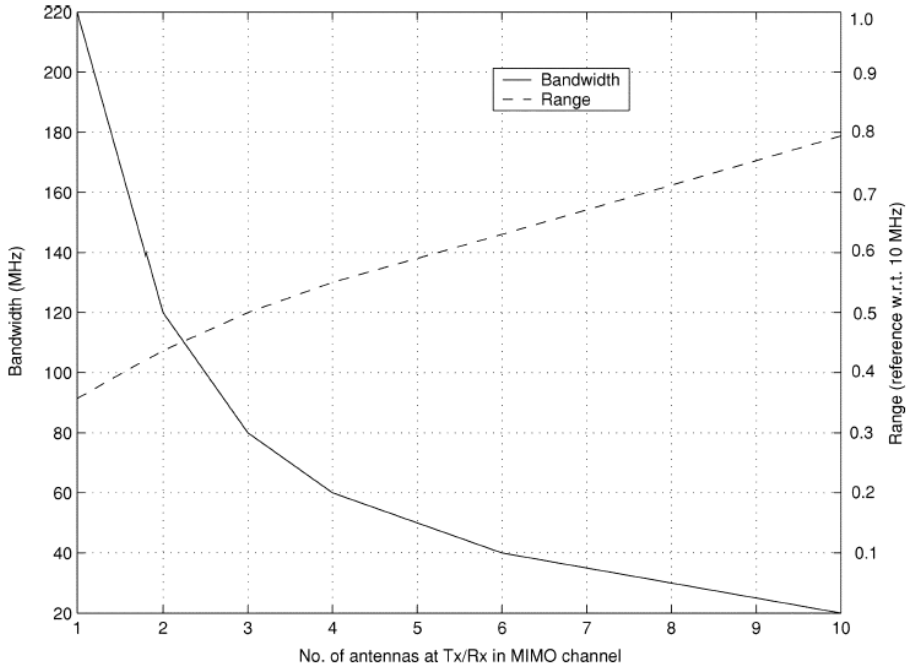

FIGURE 2.5: Bandwidth requirement and range of a 1Gb/s MIMO link [2].

2.2 THE MIMO MODEL AND CHANNEL CAPACITY

A single user MIMO system is shown in Figure 2.6 and the link model for this system can be represented as:

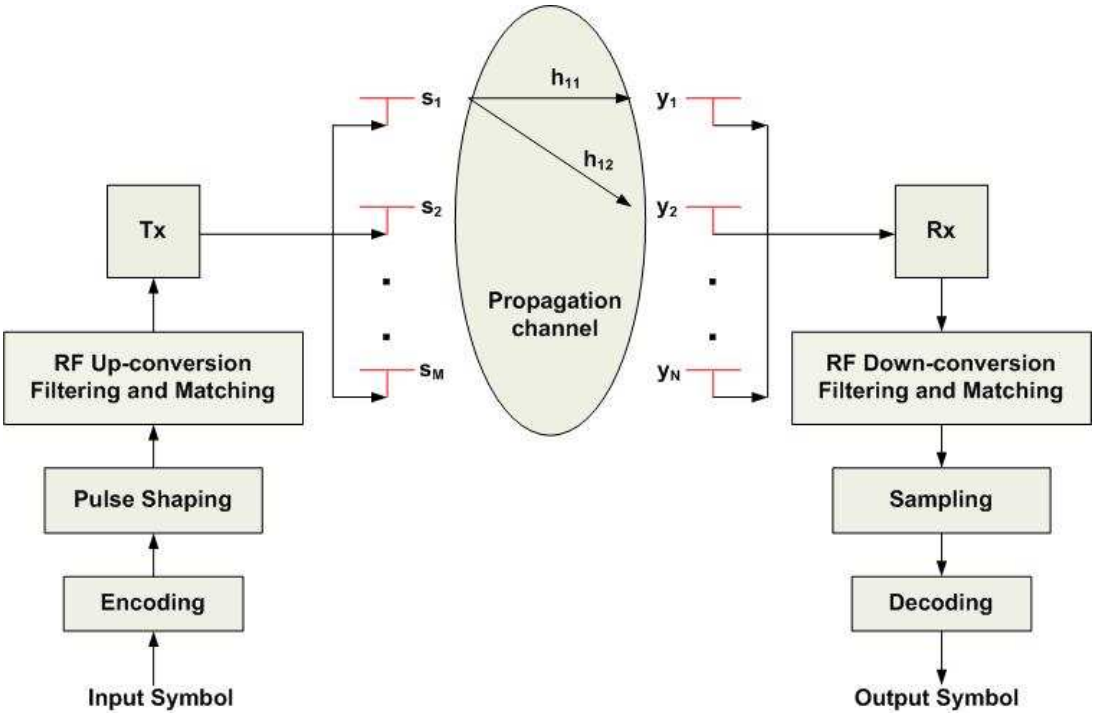

FIGURE 2.6: A single user MIMO system.

$$\mathbf{y} = \mathbf{H}\mathbf{s} + \mathbf{n} \tag{2.1}$$

where $\mathbf{y}$ and $\mathbf{s}$ are the receiving and transmitting vectors respectively, $\mathbf{n}$ is the zero-mean complex Gaussian noise and $\mathbf{H}$ is the $n \times m$ channel matrix.

This MIMO system as described above has been modeled on the following assumptions:

- the channel is random;
- a Rayleigh fading environment where there is enough separation between the receiving and transmitting antennas, to such an extent that the fades for each transmitter-receiver antenna pair are independent [15];
- the receiver has perfect channel knowledge; and
- the channel is memory-less (for each use of the channel an independent realization of $\mathbf{H}$ is drawn).

The channel is represented in matrix form as follows:

$$\mathbf{H} = \begin{bmatrix} \mathrm{h}_{11} & \mathrm{h}_{12} & ..... & \mathrm{h}_{1\mathrm{m}} \\ \mathrm{h}_{21} & \mathrm{h}_{22} & ..... & \mathrm{h}_{2\mathrm{m}} \\ . & . & ..... & . \\ \mathrm{h}_{\mathrm{n}1} & \mathrm{h}_{\mathrm{n}2} & ..... & \mathrm{h}_{\mathrm{nm}} \end{bmatrix} \tag{2.2}$$

where h_{ij}, a complex Gaussian random variable that models fading gain between the *i*th transmitting and *j*th receiving antenna, can be represented as:

$$\begin{aligned} \mathrm{h}_{\mathrm{ij}} &= \alpha + \iota\beta \\ &= \sqrt{\alpha^2 + \beta^2} e^{-\iota \arctan \frac{\beta}{\alpha}} \\ &= |\mathrm{h}_{\mathrm{ij}}| \, e^{\iota\phi_{ij}} \end{aligned} \tag{2.3}$$

where h_{ij} is a Rayleigh distributed random variable if α and β are independent and normal distributed random variables.

2.2.1 Channel Capacity

When data is transmitted through a random wireless channel, random noise is also added to the data which may result in two different input sequences with the same output sequence, causing different input sequences to be confused at the output. To avoid this a distinct subset of input sequences must be chosen so that with a high probability there is only one input sequence causing a particular output, thus making it possible to reconstruct all the input sequences at the output with a negligible probability of error [18].

The information rate of a channel encoder is given as follows [21]:

$$R = \frac{H(S)T_c}{T_s} \tag{2.4}$$

where the channel encoder receives a source symbol every T_s seconds, $H(S)$ represents the entropy rate of the set of all source symbols S and the channel codeword leaves the channel encoder every T_c seconds. Thus R information bits per channel symbol are transmitted and the maximum information rate that can be used which causes a negligible probability of error at the output is called the capacity of the channel.

When transmitting information at rate R, using the channel every T_c seconds, the channel capacity is measured in bits/channel use. If the channel has a bandwidth W, the capacity is measured in bits/s. Then, if the capacity is represented within a unit bandwidth of the channel, it is measured in bits/s/Hz.

Using the input and output of a memory-less channel, capacity can be defined as follows [18, 21]:

$$C = \max_{p(x)} I(X;Y) \tag{2.5}$$

where X and Y are random variables representing the input and output of the memory-less channel, while $I(X;Y)$ represents the mutual information between X and Y and is maximized with respect to all possible statistical distributions $p(x)$. The mutual information can also be represented as:

$$I(X;Y) = H(Y) - H(Y|X) \tag{2.6}$$

where $H(Y|X)$ is the conditional entropy between the random variables X and Y. The entropy of a random variable can be described as a measure of the average amount of information required to describe a random variable. Thus mutual information can also be defined as a measure of the amount of information that one random variable contains about another variable and depends on [18]:

1. the properties of the channel, and
2. the properties of X.

By using the mutual information the capacities of the channel can be computed as shown in the following section.

2.2.2 SISO and MIMO Channel Capacity

Ergodic (mean) SISO channel capacity, with power constraint of P_T, can be defined by the following equation [18]:

$$C = \mathrm{E_H}\{\max_{p(x):P\leq P_T} I(X;Y)\} \tag{2.7}$$

where P is the average power of a single channel codeword transmitted over the channel and $\mathrm{E_H}$ denotes the expectation over all channel realizations. The capacity is now defined as the maximum of the mutual information between the input and the output over all statistical distributions of the input that satisfy the power constraint.

If each symbol at the transmitter is denoted by s, the average power constraint is given as:

$$P = \mathrm{E}\left[|s|^2\right] \leq P_T \tag{2.8}$$

According to [16], Equation 2.7 can be expressed with a random complex channel gain h_{11} as follows:

$$C = \mathrm{E_H}\{\log_2(1 + \rho.\,|h_{11}|^2\} \tag{2.9}$$

where ρ is the average SNR at the receiver branch. If $|h_{11}|$ is Rayleigh, $|h_{11}|^2$ follows a chi-squared distribution with two degrees of freedom. The capacity can then be expressed as:

$$C = \mathrm{E_H}\{\log_2(1 + \rho.\chi_2^2)\} \tag{2.10}$$

where χ_2^2 is a chi-squared distributed random variable with two degrees of freedom.

The ergodic capacity of a MIMO channel, with a power constraint P_T, is defined as follows [18]:

$$C = \mathrm{E_H}\{\max_{p(x):t_r(\mathbf{\Phi})\leq P_T} I(\mathbf{x};\mathbf{y})\} \tag{2.11}$$

where $\mathbf{\Phi} = \mathrm{E}\{\mathbf{x}\mathbf{x}^{\mathrm{H}}\}^2$. This is the covariance matrix of the transmit signal vector $\mathbf{x}$ and the total transmit power is P_T, regardless of the number of transmitters. The mutual information $I(\mathbf{x};\mathbf{y})$ can be expanded as follows by using Equation 2.1 and the relationship between mutual information and entropy:

$$\begin{aligned} I(\mathbf{x};\mathbf{y}) &= h(\mathbf{y}) - h(\mathbf{y}|\mathbf{x}) \\ &= h(\mathbf{y}) - h(\mathbf{H}\mathbf{x} + \mathbf{n}|\mathbf{x}) \\ &= h(\mathbf{y}) - h(\mathbf{n}|\mathbf{x}) \\ &= h(\mathbf{y}) - h(\mathbf{n}) \end{aligned} \tag{2.12}$$

where $h(.)$ denotes the differential entropy of a continuous random variable.

When $\mathbf{y}$ is Gaussian, Equation 2.12 is maximized because the entropy of a given variance is maximized by the normal distribution. The differential entropy of a real Gaussian vector with zero mean and covariance matrix $\mathbf{K}$ is equal to $\frac{1}{2}\log_2(2\pi e \det \mathbf{K})$. The differential entropy of a complex Gaussian vector is less than $\log_2 \det(\pi e \mathbf{K})$, with equal values, if and only if, $\mathbf{y}$ is a circularly symmetric complex Gaussian with $\mathrm{E}\{\mathbf{y}\mathbf{y}^{\mathrm{H}}\} = \mathbf{K}$, where $(.)^{\mathrm{H}}$ denotes the conjugate matrix transpose. The covariance of the received vector $\mathbf{y}$ can then be expressed as:

$$\begin{aligned} \mathrm{E}\{\mathbf{y}\mathbf{y}^{\mathrm{H}}\} &= \mathrm{E}\{(\mathbf{H}\mathbf{x}+\mathbf{n})(\mathbf{H}\mathbf{x}+\mathbf{n})^{\mathrm{H}}\} \\ &= \mathrm{E}\{\mathbf{H}\mathbf{x}\mathbf{x}^{\mathrm{H}}\mathbf{H}^{\mathrm{H}}\} + \mathrm{E}\{\mathbf{n}\mathbf{n}^{\mathrm{H}}\} \\ &= \mathbf{H}\mathbf{\Phi}\mathbf{H}^{\mathrm{H}} + \mathbf{K}^n \\ &= \mathbf{K}^d + \mathbf{K}^n \end{aligned} \tag{2.13}$$

where d and n denote the desired part and the noise part respectively. The maximum mutual information of a random MIMO channel is then given by:

$$\begin{aligned} I &= h(\mathbf{y}) - h(\mathbf{n}) \\ &= \log_2[\det(\pi e(\mathbf{K}^d + \mathbf{K}^n))] - \log_2[\det(\pi e \mathbf{K}^n)] \\ &= \log_2[\det((\mathbf{K}^d + \mathbf{K}^n))] - \log_2[\det(\mathbf{K}^n)] \\ &= \log_2[\det((\mathbf{K}^d + \mathbf{K}^n)(\mathbf{K}^n)^{-1})] \\ &= \log_2[\det(\mathbf{K}^d(\mathbf{K}^n)^{-1} + \mathbf{I}_{nR})] \\ &= \log_2[\det(\mathbf{H}\mathbf{\Phi}\mathbf{H}^{\mathrm{H}}(\mathbf{K}^n)^{-1} + \mathbf{I}_{nR})] \end{aligned} \tag{2.14}$$

When the transmitter has no knowledge about the channel, it is optimal to use a uniform power distribution. The transmit covariance matrix is then given by $\mathbf{\Phi} = \frac{P_T}{n_T}\mathbf{I}_{nT}$. Uncorrelated noise in each receiver branch can be described by the covariance matrix $\mathbf{K}^n = \sigma^2\mathbf{I}_{nR}$. The ergodic capacity for a complex Additive White Gaussian Noise (AWGN) MIMO channel can then be given by:

$$C = \mathrm{E}_{\mathrm{H}}\left\{\log_2\left[\det\left(I_{nR} + \frac{P_T}{\sigma^2 n_T}\mathbf{H}\mathbf{H}^{\mathrm{H}}\right)\right]\right\} \tag{2.15}$$

It can also be given as:

$$C = \mathrm{E_H}\left\{\log_2\left[\det\left(I_{nR} + \frac{\rho}{n_T}\mathbf{H}\mathbf{H}^{\mathrm{H}}\right)\right]\right\} \tag{2.16}$$

where $\rho = \frac{P_T}{\sigma^2}$ is the average SNR at each receiver branch.

The MIMO channel capacity in Equation 2.16 can be further analyzed by diagonalizing the channel product matrix $\mathbf{H}\mathbf{H}^{\mathrm{H}}$ either by eigenvalue decomposition or singular value decomposition.

The eigenvalue decomposition of the channel product matrix can be written as:

$$\mathbf{H}\mathbf{H}^{\mathrm{H}} = \mathbf{E}\mathbf{\Lambda}\mathbf{E}^{\mathrm{H}} \tag{2.17}$$

where $\mathbf{E}$ is the eigenvector matrix with orthonormal columns. $\mathbf{\Lambda}$ is the diagonal matrix with eigenvalues on the main diagonal and the *k*th eigenvalue representing the power gain of the *k*th subchannel. The capacity in Equation 2.16 can thus be written as:

$$C = \mathrm{E_H}\left\{\log_2\left[\det\left(I_{nR} + \frac{\rho}{n_T}\mathbf{E}\mathbf{\Lambda}\mathbf{E}^{\mathrm{H}}\right)\right]\right\} \tag{2.18}$$

The singular value decomposition of the channel matrix can be written as:

$$\mathbf{H} = \mathbf{U}\mathbf{\Sigma}\mathbf{V}^{\mathrm{H}} \tag{2.19}$$

where $\mathbf{U}$ and $\mathbf{V}$ are unitary matrices of the left and right singular vectors, respectively and $\mathbf{\Sigma}$ is a triangular matrix with singular values on the main diagonal. The the capacity in Equation 2.16 can thus be written as:

$$C = \mathrm{E_H}\left\{\log_2\left[\det\left(I_{nR} + \frac{\rho}{n_T}^{\mathrm{H}}\mathbf{U}\mathbf{\Sigma}\mathbf{\Sigma}^{\mathrm{H}}\mathbf{U}^{\mathrm{H}}\right)\right]\right\} \tag{2.20}$$

From Equations 2.17 and 2.19 it can be seen that all elements on the diagonal are zero except for the first k elements. The number of non-zero singular values k equals the rank of the channel matrix. As can be seen from Equations 2.18 and 2.20, the capacity formulas of the MIMO channel includes unitary and diagonal matrices only. Thus the total capacity of a MIMO channel is made up by the sum of parallel AWGN SISO subchannels. The number of subchannels is determined by the rank of the channel matrix. The rank of the channel matrix is given by:

$$\mathrm{rank}(\mathbf{H}) = k \leq \min\{n_T, n_R\} \tag{2.21}$$

From Equation 2.21 as well as the fact that the determinant of a unitary matrix is equal to 1, Equations 2.17 and 2.19 can be respectively expressed as:

$$C \leq \mathrm{E_H}\left\{\sum_{i=1}^{k}\log_2(1+\frac{\rho}{n_T}\lambda_i)\right\} \tag{2.22}$$

$$= \mathrm{E_H}\left\{\sum_{i=1}^{k}\log_2(1+\frac{\rho}{n_T}\sigma_i^2)\right\} \tag{2.23}$$

where λ_i represents the eigenvalues of the diagonal matrix $\mathbf{\Lambda}$ and σ_i^2 represents the squared singular values of the diagonal matrix $\mathbf{\Sigma}$. Thus the maximum capacity of a MIMO channel is reached when each of the n_T transmitted signals is received by the same set of n_R antennas without interference.

Finally, by optimally combining at the receiver, the channel matrix follows a chi-squared distribution of $2n_R$ degrees of freedom and the capacity can be expressed as follows:

$$C = \mathrm{E_H}\left\{n_T \cdot \log_2\left[1+\frac{\rho}{n_T}\chi^2_{2n_R}\right]\right\} \tag{2.24}$$

Thus far it has been shown mathematically how the capacities of a MIMO system are achieved. Figure 2.7 compares SISO capacity with Shannon's capacity. Figure 2.8 does the same but with MIMO capacity. Performance gains of the MIMO system is greater than that of the SISO system. From Equation 2.21 it is evident that capacity scales linearly with $\min\{n_T, n_R\}$, Figure 2.9 shows an increase in capacity as the number of antennas increase.

As seen from the capacity equations in this section, the properties of the channel matrix play an important part in the performance of the MIMO system. The channel matrix in turn can be influenced by the following [22]:

1. array size and configuration,
2. mutual coupling,
3. antenna impedance matching,
4. element pattern and polarization properties, and
5. multipath propagation.

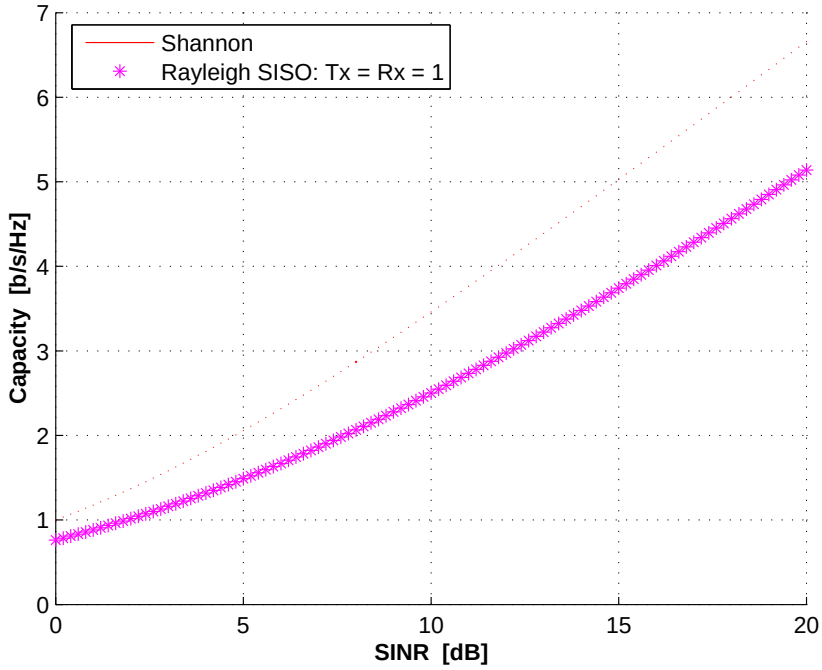

FIGURE 2.7: Ergodic capacity of a SISO channel.

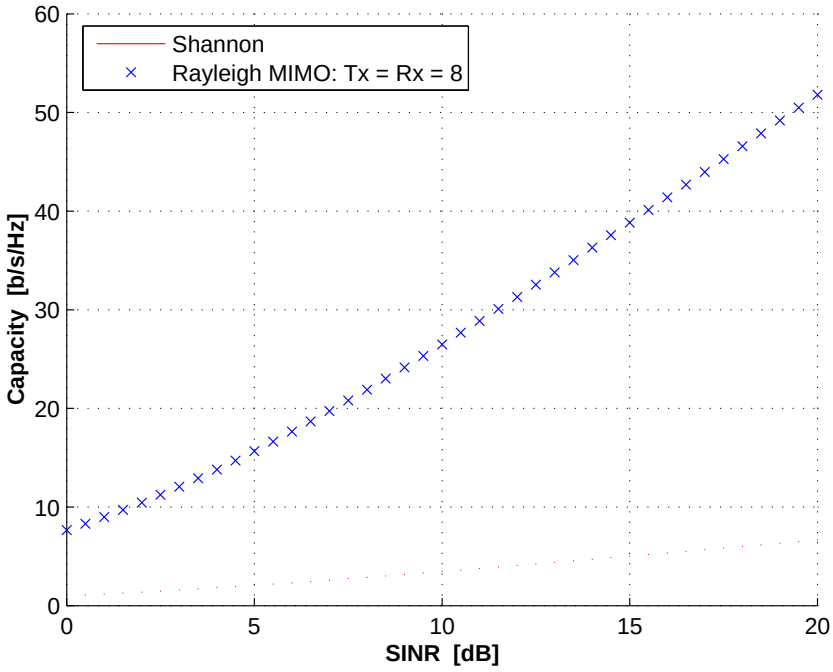

FIGURE 2.8: Ergodic capacity of a MIMO channel.

Considering that this study involves the use of polarized antennas, the factor “element pattern and polarization” will be discussed in more detail in the next section.

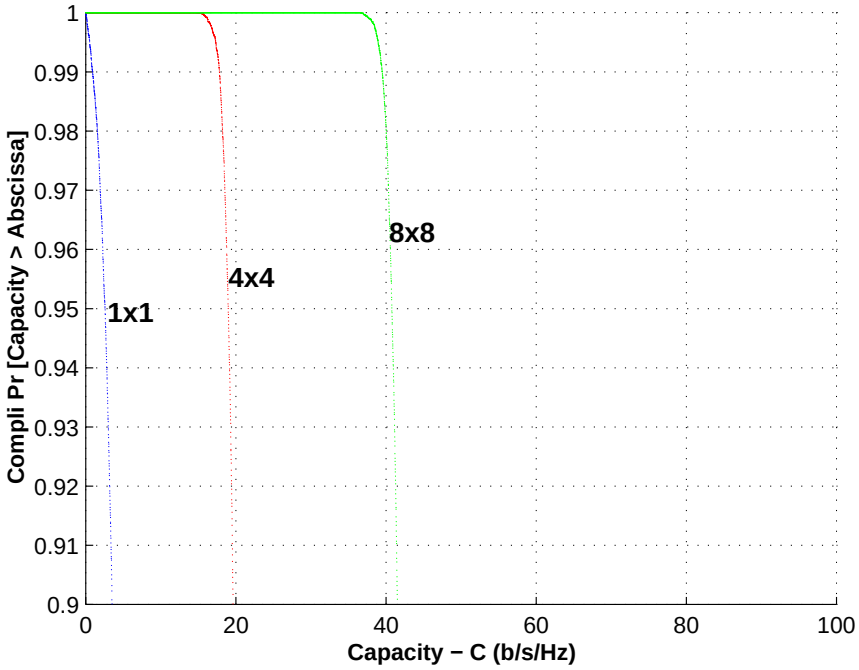

FIGURE 2.9: CCDF of the capacity of an incremental MIMO system in Rayleigh fading.

2.3 POLARIZATION DIVERSITY

Antenna diversity aims to achieve fading at each antenna, independent of the other antennas, so as to minimize the likelihood of all signals fading identically. Independent fading can be achieved by doing the following:

- Spacing antennas far apart (spatial diversity), this is especially useful for signals coming from far away.
- Pointing antennas in different directions or using antennas with different patterns (pattern diversity), thus signals on different paths can be received on each antenna.
- Using different polarizations (polarization diversity), because orthogonal polarizations have independent fading.

Spatial multiplexing ensures a large diversity gain. However, with increased numbers of antennas being implemented in mobile phones and similar devices where space is highly limited, it places a restriction on the number of antennas that can be used on such devices. Achieving antenna spacings of several tens of wavelengths at the receiver and up to a

wavelength at the transmitter is also expensive [23].

Polarization diversity is both a cost and space effective alternative where two spatially separated single polarized antennas can be replaced by a single antenna structure employing orthogonally polarized elements.

The polarization of an antenna is determined by the electric field of the energy radiated by the antenna. Three types of polarizations can be defined [24]:

- Elliptical polarization: the electric field has two linear components, orthogonal to each other, and at any point along the direction of propagation the total electric field traces out an ellipse as a function of time.
- Circular polarization: consists of two linear polarized electric fields that are orthogonal and of equal amplitude, but 90^0 out of phase.
- Linear polarization: consists of a single electric field component and the propagation wave is traced out as a straight line.

Several polarization diversity configurations have been developed to enhance signal reception, namely [25]:

- an array of dual-polarized elements;
- an array of spatially separated orthogonally polarized elements (hybrid); and
- an array of circularly polarized elements.

The configurations mentioned above take advantage of the fact that many linearly polarized multipath signals with different orientations exist and consequently they have a better chance of receiving more total signals than a single linear polarized antenna. Since the system used in this study is dual-polarized, a brief description thereof will follow.

The MIMO channel matrix of a dual-polarized system in Figure 2.10 can be represented as follows:

$$\mathbf{H} = \begin{bmatrix} \mathbf{H_{VV}} & \mathbf{H_{HV}} \\ \mathbf{H_{VH}} & \mathbf{H_{HH}} \end{bmatrix} \tag{2.25}$$

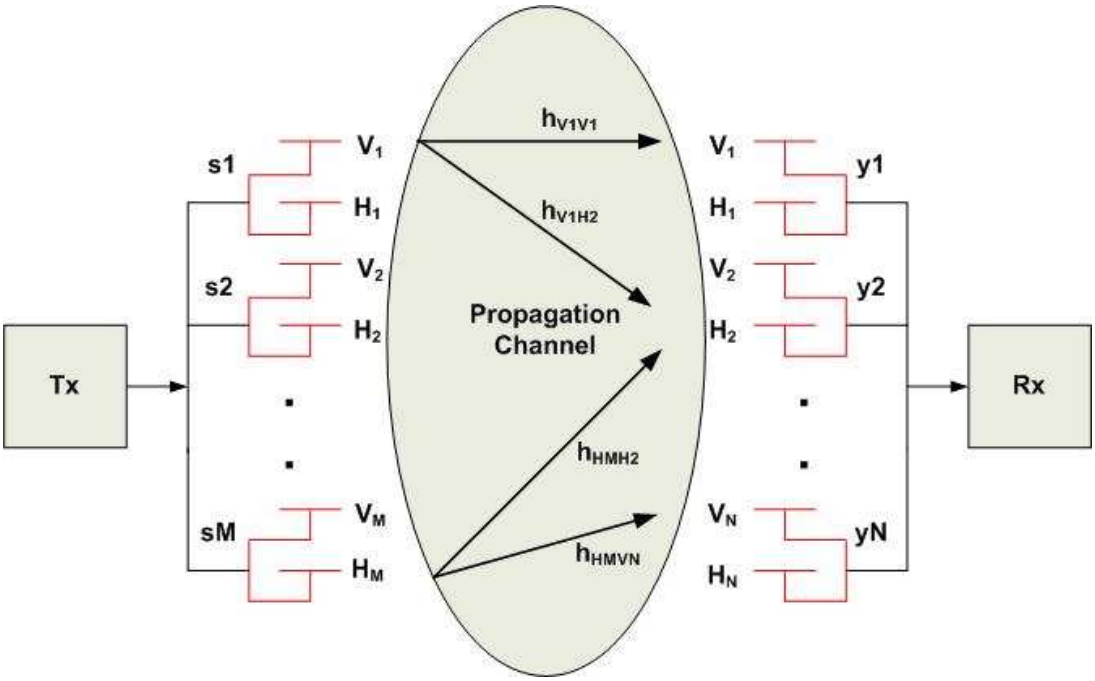

FIGURE 2.10: Dual-polarized co-located antennas.

where $\mathbf{H_{IJ}}$ is a sub-channel matrix consisting of the polarization I and J at the Rx and Tx respectively. $\mathbf{H_{IJ}}$ can be further represented as:

$$\mathbf{H_{IJ}} = [h_{I_i J_j}] \quad i, j \in \{M, N\} \tag{2.26}$$

where $h_{I_i J_j}$ is the narrowband radio channel from a single antenna port at the transmitter, I_i, to a single antenna port at the receiver, J_j as shown in Equation 2.27.

$$\mathbf{H} = \begin{bmatrix} \mathrm{h_{V1V1}} & \mathrm{h_{V1H1}} & \mathrm{h_{V1V2}} & \mathrm{h_{V1H2}} & \ldots & \mathrm{h_{V1Vn}} & \mathrm{h_{V1Hn}} \\ \mathrm{h_{H1V1}} & \mathrm{h_{H1H1}} & \mathrm{h_{H1V2}} & \mathrm{h_{H1H2}} & \ldots & \mathrm{h_{H1Vn}} & \mathrm{h_{H1Hn}} \\ . & . & . & . & \ldots & . & . \\ . & . & . & . & \ldots & . & . \\ \mathrm{h_{VmV1}} & \mathrm{h_{VmH1}} & \mathrm{h_{VmV2}} & \mathrm{h_{VmH2}} & \ldots & \mathrm{h_{VmVn}} & \mathrm{h_{VmHn}} \\ \mathrm{h_{HmV1}} & \mathrm{h_{HmH1}} & \mathrm{h_{HmV2}} & \mathrm{h_{HmH2}} & \ldots & \mathrm{h_{HmVn}} & \mathrm{h_{HmHn}} \end{bmatrix} \tag{2.27}$$

By multiplexing data streams not only over the spatially separated antenna elements, but also over the two branches of the dual-polarized antennas, the number of subchannels in a MIMO communication system increases [26]. The achievable separation of the data streams at the receiver depends on the available polarization diversity, which is also dependent on the cross

polarization discrimination factor (XPD).

Multiple reflections between the transmitter and the receiver lead to the depolarization of radio waves, coupling some of the transmitted signal energy into the orthogonal polarized wave. As a result of this, vertically/horizontally polarized transmitted waves can also have a horizontal/ vertical component. In the case of insufficient depolarization, significant power imbalance between the average power of the co-polarized and cross-polarized signals can make the whole diversity system worthless. The parameter that indicates this power difference is denoted as XPD. High XPD values lead to significant degradation of the system's performance, i.e. lower diversity gain. The XPD of the vertical and horizontal polarizations can be given as follows:

$$\mathrm{XPD_V} = \frac{\mathrm{E}\left\{|\mathrm{h_{VV}}|^2\right\}}{\mathrm{E}\left\{|\mathrm{h_{HV}}|^2\right\}} \tag{2.28}$$

$$\mathrm{XPD_H} = \frac{\mathrm{E}\left\{|\mathrm{h_{HH}}|^2\right\}}{\mathrm{E}\left\{|\mathrm{h_{VH}}|^2\right\}} \tag{2.29}$$

Due to symmetry $\mathrm{XPD_V}$ and $\mathrm{XPD_H}$ are often assumed to be equal. However this is dependent on the environment and the antenna patterns of the vertical and horizontal elements [25].

Dual-polarization MIMO communication ensures that orthogonally polarized elements can be co-located which can lead to more compact antenna designs and as a result of this, various studies have been conducted to investigate the performance of this polarization diversity scheme.

Early work in this area showed that for a fixed SNR, dual-polarized antennas provide higher capacity than single-polarized antennas [27, 28]. However when that transmit power is fixed there is approximately a 3 decibel (dB) loss in receiver power, due to the limited level of depolarization for most propagation environments.

In a separate experimental analysis conducted by [29], it was demonstrated that capacity gains of around 10-20% were acheived from using dual-polarization over single polarization in an indoor environment. Monte Carlo simulations by [30] have also found that indoor MIMO capacity, using dual-polarization, results in higher capacity and that the channel capacity increases linearly with SNR. In [31], polarization diversity performance for 3×3

MIMO systems under Rayleigh-fading environments is evaluated through simulations and measurements. True polarization diversity was found to be as significant as spatial diversity at improving diversity gain, and hence MIMO system capacity.

The performance of a dual-polarized MIMO system using LOS (Line-of-Sight) and NLOS (Non-Line-of-Sight) measurements was investigated by [32]. Capacity was compared for constant transmit power and constant SNR between a 4×4 horizontally polarized (H-pol), vertically polarized (V-pol) and a hybrid MIMO system. Measurements were taken in a two-storey building, where the outside walls are made of glass and the inside walls of wood and wallboard. Different polarizations result in different reflection coefficients. The floor and the ceiling can be represented as a conducting material thus the reflection for both the H-pol and V-pol is high. Walls are dielectric materials and consequently waves parallel to the wall (the H-pol) undergo a Brewster angle[6] phenomenon and penetrate the walls without any reflection. Waves perpendicular to the wall, like the V-pol, do not undergo this phenomenon.

The LOS measurements were conducted in the hallway, where there is little local scattering and the angular spread is minimal. The power of the H-pol waves decay faster than the power of the V-pol waves and the XPD is about -15 dB. For both constant SNR and constant power, the hybrid system performs better than the H-pol or V-pol systems. At constant power, H-pol achieves lower capacity than V-pol, because it has lower received power. Coupling between the polarizations is due to scattering from indoor clutter and oblique incidence on the wall. The NLOS measurements were carried out in the laboratory (lab), where there is more scattering and the angular spread is greater. The power of the H-pol and V-pol waves are similar and XPD is 0 dB. H-pol and V-pol systems achieve similar capacities because both have the same average received powers. The hybrid system only performs slightly better as a result of co-polarization coupling for rich scattering.

In [25] measurements were conducted again in LOS (in a corridor lined with offices on one side and a lab on the other) and NLOS (in a lab) environments, taking into consideration the Ricean K-factor, XPD, and inter-element spacing. Capacity comparisons are made between single polarized, dual-polarized and hybrid-polarized systems. In the LOS scenario for small inter-element spacing, polarization-based configurations achieved lower channel correlations

[6] The angle of incidence that produces a 90^0 angle between the reflected and refracted ray.

than spatial configurations, which resulted in higher capacity. For higher inter-element spacing, spatial configurations tend to suffer less power loss and they have lower spatial correlation which results in higher capacities than hybrid- or dual-polarized systems. These systems suffer from subchannel power losses because of high XPD values and horizontally polarized transmissions. In the NLOS scenario with limited depolarization, dual-polarized and hybrid configurations achieved lower capacities when compared to their spatial counterparts. In scenarios where channels have a low K-factor but a high XPD, polarized MIMO systems tend to suffer a loss in SNR and diversity when compared to single polarized configurations. Therefore if space is not a constraint, then spatial configurations should be chosen over dual- or hybrid-polarizations.

Linear polarized transmitting and receiving antennas provide higher capacity when they are polarization matched. When the orientation of the antennas is not fixed (such as on a handset), the lost power can be largely due to misalignment and limited depolarization, in which case dual-polarized elements have higher capacity than single-polarized elements [32–34]. In [35] it was found that polarized elements offer good decorrelation and lower, but more stable, received powers. Linear polarized elements offer better receiving powers when the elements at both ends of the link are co-oriented, while cross-polarized elements result in better decorrelation and resilience for orientation.

Patch antennas provide a good degree of isolation, making them adequate for dual-polarization. However, the hemispheric pattern of the patch antenna, can result in a smaller radiation pattern with fewer multipath components being received, as well as a reduction of rich scattering that is required for high capacity gains. Patch antennas are also shown to have a limited XPD in [36]. Dual-polarized MIMO systems, using patch antennas as investigated in [37], were shown to achieve mean capacities of 21 bits/use.

Most of the studies have shown that there is an advantage to using dual-polarized MIMO systems. However, as indicated above and in studies by [23], the performance of dual-polarized systems are sensitive to:

- antenna spacing,
- angle spread,

- XPD, and
- antenna slant offset angles.

Furthermore, as indicated by [32], there are environments where the antenna placement and/or polarization is not the limiting factor in the capacity behavior of the system, but rather the channel itself is.

2.4 CHAPTER SUMMARY

This chapter firstly provides a background to MIMO technology. Wireless communication systems utilizing multiple antenna structures have been shown to take advantage of multipath signals to increase system capacity. Three groups of multiple antenna structures have been identified: SIMO, MISO, and MIMO. Applying "smart" signal processing to these antenna structures improves the performance of the wireless system. However, considering that only one data stream per channel is transmitted, capacity improvements of only 1 b/s/Hz or 2 b/s/Hz are offered.

On the other hand MIMO systems make smart antennas multi-dimensional, enabling multiple data streams to be transmitted and as a result more information can be transmitted in the same channel. This in turn results in a linear increase in capacity. Improvements in MIMO performance can be attributed to either array gain, diversity gain, spatial multiplexing gain, or interference reduction. It is not possible to use these enhancements simultaneously due to conflicting demands on the number of antennas used, and the degree to which these conflicts are resolved depends on the signaling scheme and the transceiver design.

The capacity gains achieved by using MIMO have been enormous that even 1 Gb/s rates are becoming possible. Comparison of the Rayleigh MIMO and SISO capacities with Shannon's capacity, as shown in Figure 2.7 and Figure 2.8, shows the performance gain of the MIMO system. Figure 2.9 indicates how the capacity of a MIMO system increases with increasing antenna size.

This chapter also focused on the use of polarization diversity with MIMO systems. Antenna diversity can be divided into three groups: spatial diversity, pattern diversity and polarization

diversity. Spatial diversity places a restriction on the number of antennas that can be implemented, especially on devices where space is highly limited. Polarization diversity offers an additional decorrelated channel, providing a polarization state orthogonal to the existing state, and thus lifting the restriction on the number of antennas that can be implemented.

Polarization of an antenna is determined by the electric field of the energy radiated by the antenna and three types of polarization were defined: elliptical, circular, and linear polarizations. Linear dual-polarized antennas have been gaining popularity for use with MIMO systems, and by multiplexing data streams, not only over the spatially separated antenna elements, but also over the two branches of the dual-polarized antennas, the number of subchannels in a MIMO communication system increases. The key advantage of using two polarizations is that, regardless of the environment, at least two parallel channels are enabled, each carrying different information. Measurement studies that were conducted using dual-polarized MIMO systems have shown that there is an advantage to using dual-polarized antennas over single polarized antennas.

CHAPTER THREE

MIMO MODELS AND MEASUREMENTS

Assessing the performance of MIMO systems in realistic environments requires a detailed description of the multipath channel [22]. This can be achieved through channel matrix measurements and/or channel modeling. Various channel models and channel measurement techniques that are found in literature are discussed below.

3.1 TRANSFER MATRIX MEASUREMENT

Transfer matrix measurement [38–46] is a direct way of measuring the $n \times m$ channel matrix ($\mathbf{H}$). The measurement campaign involves setting up a physical communication link to measure the impulse responses between the transmitter and receiver. Results from such measurement campaigns include channel capacity, the signal correlation structure, the channel matrix rank, path loss, delay spread, etc. Antenna arrays that are deployed in these measurements can be categorized into three types [3, 22], and are listed below.

- True or real array systems as shown in Figure 3.1: simultaneous measurements take place at all antenna elements. These systems closely model real-world MIMO communication and can accommodate channels that vary with regards to time. However mutual coupling can occur between antenna elements and the costs of parallel transmitting and receiving electronics are high.
- Switched or multiplexed array systems as shown in Figure 3.2: a single Tx and Rx antenna element is used to measure the transfer function with high speed switches sequentially connecting array elements to electronics. The switching times with these systems are

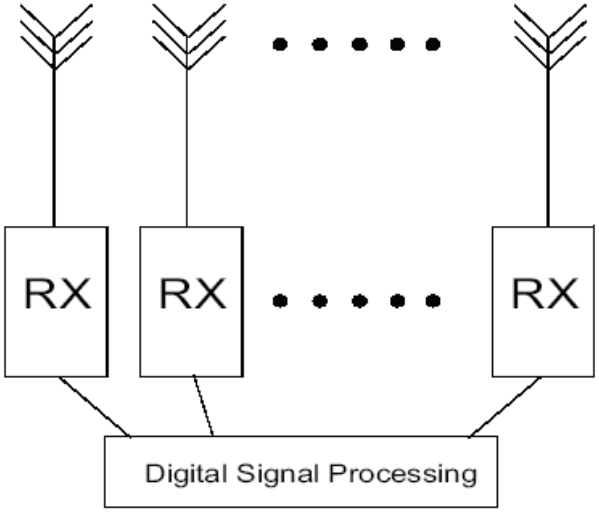

FIGURE 3.1: The real array system as taken from [3].

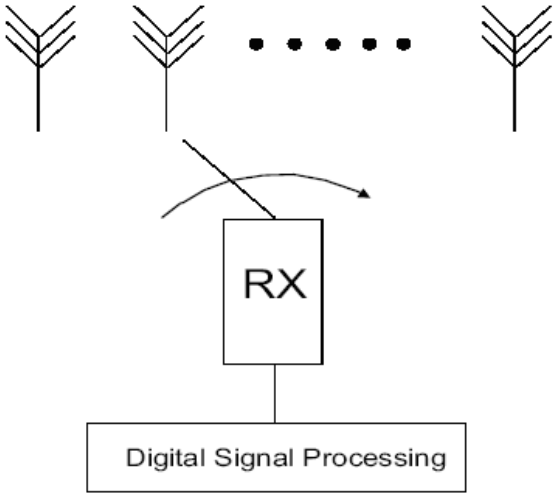

FIGURE 3.2: The switched array system as taken from [3].

generally fast, therefore measurement over all antenna pairs can be conducted before the channel changes appreciably.

- Virtual array systems as shown in Figure 3.3: a single antenna element is rotated precisely to prescribed locations. This technique is able to eliminate mutual coupling. However, a complete channel matrix measurement takes several minutes or seconds and it requires that the channel be stationary for a long time.

Although direct measurement techniques are able to capture real-world MIMO characteristics, the setting up of this measurement equipment can be time consuming, complex, and expensive.

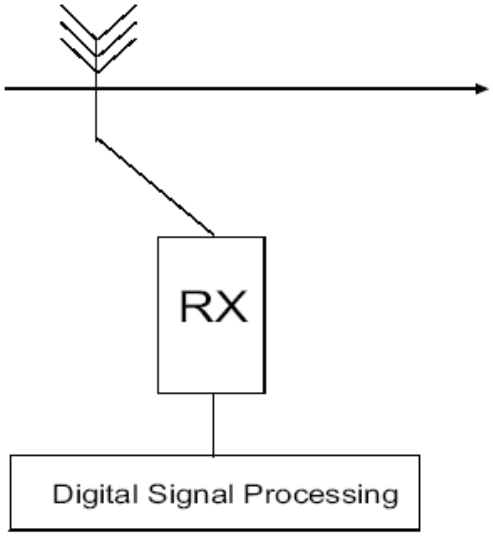

FIGURE 3.3: The virtual array system as taken from [3].

Physical models have thus been developed to characterize the physical multipath propagation between the transmitter and the receiver. They explicitly model radio wave propagation parameters such as DoA (Direction of Arrival), DoD (Direction of Departure), multipath component delay, etc. and are independent of antenna configurations such as antenna radiation patterns, antenna geometry, and system bandwidth. Physical models can be categorized into: deterministic, geometry-based stochastic and non-geometrical models. These models are discussed below.

3.2 DETERMINISTIC MODELS

Deterministic models reproduce the actual physical radio propagation process for a given environment. The geometric and electromagnetic characteristics of the environment and radio link can easily be stored in computer files. The corresponding propagation process can then be simulated through computer programs and represented as two-dimensional (2-D) or three-dimensional (3-D) models. The ray-tracing method is the most popular of the deterministic models and is discussed below.

3.2.1 The Ray-tracing Method

In this method the theory of geometrical optics is used to treat reflection and transmission on plane surfaces and diffraction on rectilinear edges [4]. The geometrical optics are based on

what is termed “ray approximation”, which assumes that the wavelength is sufficiently small compared to the dimensions of the obstacles in the environment. Electromagnetic fields are thus represented as a set of rays, each corresponding to a path connecting two terminals and each corner in the path represents an interaction with an obstacle (for example reflection off a wall). The ray-tracing method is able to show channel parameters such as spatial signal variation with small-scale movement, capacity variation with array location and antenna spacing, and angular clustering of multipath arrivals.

The following steps are applied with the method as presented in [4]:

- first the Tx and Rx positions are specified;
- all possible paths from the Tx to the Rx are then determined according to geometric considerations and rules of geometric optics;
- a visibility tree as shown in Figure 3.4 is then created to capture the individual propagation paths and is built in a recursive way; and
- finally a backtracking procedure is applied to determine the path of each ray by traversing the tree upward toward the root node, and applying the appropriate geometric optics rules at each traversed node.

The ray-tracing method has demonstrated reasonable accuracy [22] and, as already stated, can be used in place of more difficult and time-consuming direct measurement techniques. The method is site specific and over-simplification of the geometrical scenario that has been represented can lead to underestimation of the MIMO channel capacity. The computational costs of the ray-tracing simulations are also very high.

3.3 GEOMETRY-BASED STOCHASTIC CHANNEL MODELS

Geometry-based stochastic models (GBSM) model scatterers as discreet objects located about the transmitter and/or receiver in a stochastic (random) fashion and according to a certain probability distribution [47]. The channel impulse response is then found by the ray-tracing method.

Scatterers can be modeled in two ways as identified in [4], namely:

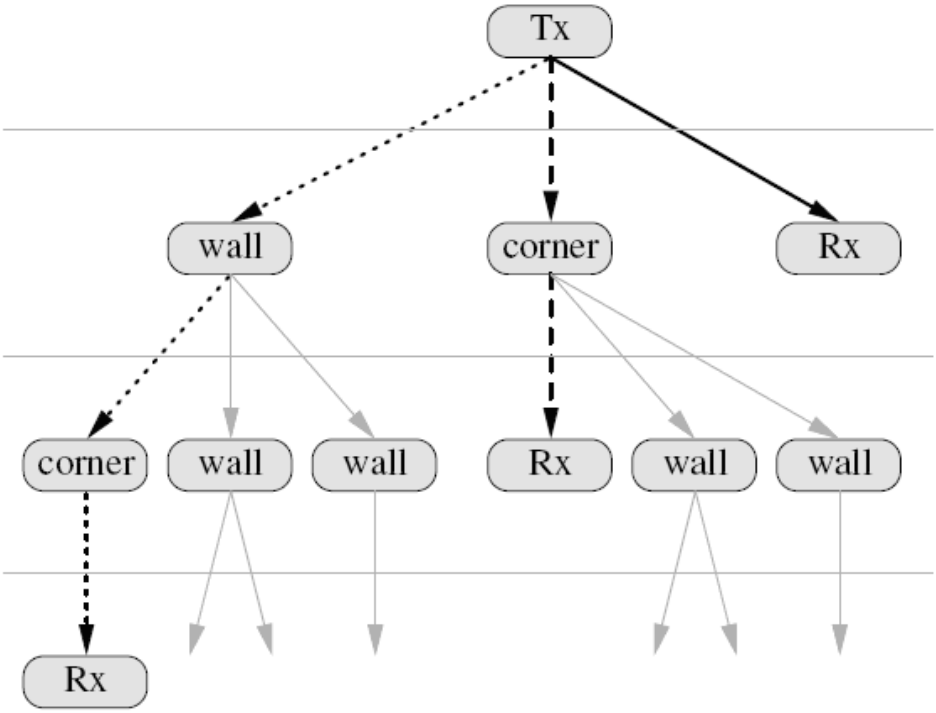

FIGURE 3.4: The ray-tracing visibility tree as taken from [4].

- Single bounce scattering: scatterers are randomly placed around the Tx or Rx and only a single scattering occurs (i.e. there is only one interacting object between the Tx and Rx). All paths thus consist of two sub-paths connecting the scatterer to the Tx and Rx, and the propagation is then modeled through the ray-tracing method. It is, however, restrictive in that the position of the scatterer completely determines the DoD, DoA, and the delay of the multipath component (MPC) that propagate via near scatterers.

- Multiple bounce scattering: this relates to real environments where radio waves undergo multiple reflection and diffractions and the DoA, DoD, and the delay are decoupled as shown in Figure 3.5.

The above-mentioned scatterings would not realistically represent a MIMO system and thus two other models have been proposed, which are discussed below.

3.3.1 The Double Scattering Model

In the model proposed by [5], double scattering occurs (i.e. there are scatterers around the Tx and Rx as shown in Figure 3.6), and coupling between the scatterers around the Tx and Rx are

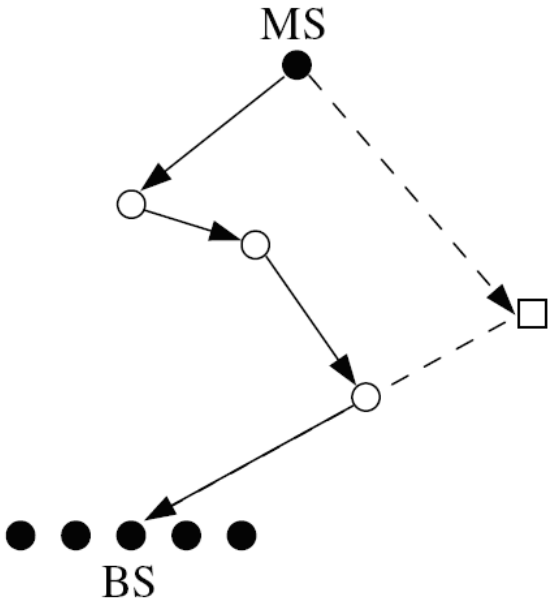

FIGURE 3.5: Multiple bounce scattering of the GBSM as taken from [4].

established by an illumination function (DoD spectrum relative to the scatterer).

The double scattering model moves away from the perception of existing models that the DoA and DoD are separable because waves can propagate from each Tx scatterer to each Rx scatterer with equal probability. This may be possible in macrocells (which provide the largest area of coverage for wireless communication), but not so for most microcells (which provide additional coverage area within a macrocell) and picocells (which provide coverage within a microcell) environments with specular reflection (mirror-like reflection of a wave from a surface) [5]. In this case, each scatterer near the Tx will only illuminate a few scatterers near the Rx, essentially with a certain angular spread that will depend on the surface roughness of the scatterers. Thus with this model, for each Tx scatterer, an angular distribution function and an angular spread that determines the number of scatterers that are illuminated by each Tx scatterer are defined. The model in [5] also includes clusters of far scatterers, waveguide propagation and diffraction.

The double scattering model provides a complete generic MIMO model taking many factors into consideration. However, a considerable number of parameters are needed and the establishment of the statistical distributions of these parameters is time consuming.

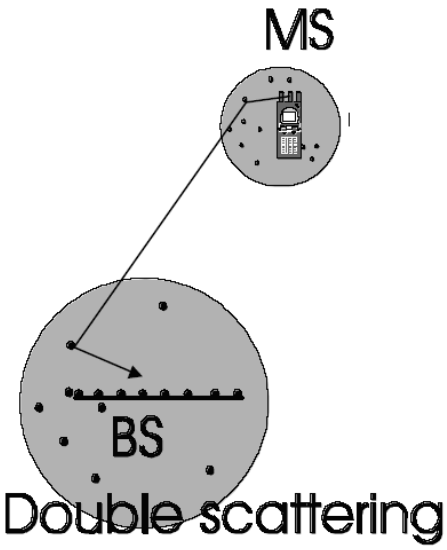

FIGURE 3.6: Scattering around the Tx and Rx as taken from [5].

3.3.2 The Distributed Scattering Model

This is a generic stochastic model, as shown in Figure 3.7, that separately captures the diversity and rank properties of the MIMO channel [6]. The propagation path between the arrays is obstructed on both sides of the link by a set of significant near-field scatterers, such as buildings and large objects. The model is mainly used for outdoor MIMO channels.

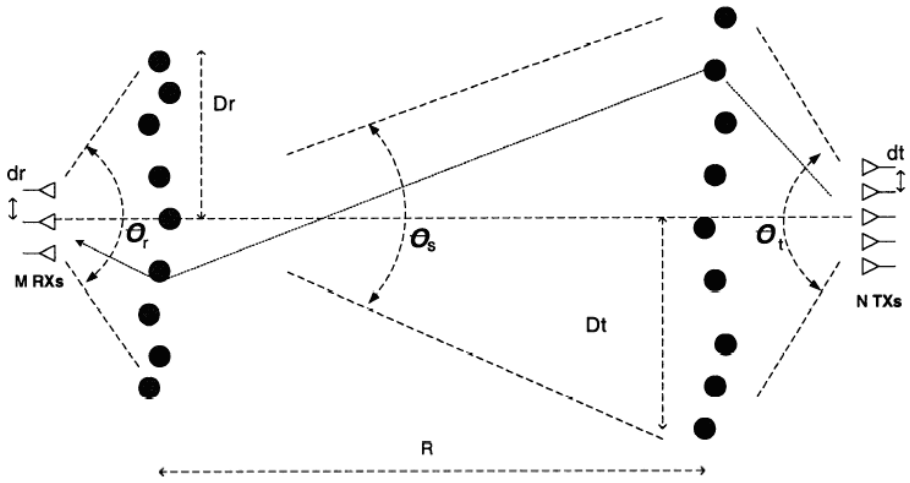

FIGURE 3.7: The distributed scattering model as taken from [6].

3.4 NON-GEOMETRICAL STOCHASTIC MODELS

Non-geometrical stochastic models describe paths from the transmitter to the receiver by statistical parameters only, without reference to the geometry of the physical environment. Two categories of the model are discussed below.

3.4.1 The Extended Saleh-Valenzuela (ESV) Model

This model uses the principle of grouping multipath components into clusters as in [48], where a single cluster of arrivals might correspond to a single scattering object and the arrivals within the cluster arise due to small object features. The model was then extended as in [27] to also include directional information. The ESV model is based on the assumption that DoA and DoD statistics are independent and identically distributed (i.i.d.) therefore the assumption allows for the characterization of spatial clusters in terms of the mean cluster angle and the cluster angular spread.

The ESV model can offer highly accurate statistical channel representation, provided that the underlying statistical distributions are properly specified [27]. The ESV model has also shown good agreement with measured data based on channel capacity probability density function (PDF).

3.4.2 The Zwick Model

Unlike the ESV model where the MPCs are treated as clusters, the MPCs in the Zwick model are treated individually [38]. The reason for this is that for indoor channels, clustering and multipath fading do not occur when the sampling rate is sufficiently large. Phase changes of the MPCs are however incorporated into the model which geometrically describes the Tx, Rx, and scatterer motion [4]. The geometry of the scenario also takes into account the “birth” and “death” of clusters due to the movement of the subscriber [22]. For NLOS MPCs the effect is modeled using a Poisson process while for LOS it is added in a separate step.

As already explained above, physical models take into account the propagation of the radio wave in a MIMO channel, without any direct measurements. Analytical models also characterize the channel transfer function without measurements in a mathematical way. Several analytical

methods are discussed below.

3.5 ANALYTICAL CHANNEL MODELS

Analytical models are MIMO channel models which provide analytical expressions, which in turn describes the transfer matrix of the channel between elements of the antenna arrays, i.e. the impulse response between the receiver and the transmitter.

Analytical models can be categorized into correlation-based analytical models and propagation-motivated analytical models [4], both of which are described below.

In this section, and in the sections to follow the vec$(.)$ operator stacks the columns of a matrix into one vector and the tr$(.)$ operator denotes the trace of a matrix. The superscripts $(.)^{\mathrm{T}}$, $(.)^{\mathrm{H}}$, and $(.)^*$ denote the matrix transpose, conjugate matrix transpose, and the complex conjugate respectively.

3.5.1 The Correlation-based Analytical Model

These models characterize the MIMO channel matrix statistically in terms of the correlations between matrix entries.

The $nm \times mn$ matrix is given by Equation. 3.1 below:

$$\mathbf{R}_{\mathrm{H}} = \mathrm{E}\{\mathbf{H}\mathbf{H}^{\mathrm{H}}\} \tag{3.1}$$

where $\mathbf{R}_{\mathrm{H}}$ is known as the full correlation matrix and contains the correlations of the channel matrix elements describing the spatial MIMO channel statistics. The realizations of the MIMO channel can then be obtained by Equation 3.2:

$$\mathbf{H} = \mathrm{unvec}\{\mathbf{R}_{\mathrm{H}}^{1/2}\mathbf{g}\} \tag{3.2}$$

where $\mathbf{R}_{\mathrm{H}}^{1/2}$ denotes the square root of the full correlation matrix, and $\mathbf{g}$ is an $nm \times 1$ vector with i.i.d. Gaussian elements with zero mean and unit variance.

The realization of Equation 3.2 above involves the use of $(nm)^2$ real-valued parameters. In order to reduce the large number of parameters several different models, which are described below, were proposed to impose a particular structure on the MIMO correlation matrix.

3.5.1.1 The Gaussian i.i.d. Model

This is the simplest, yet most idealistic, analytical model where $\mathbf{R}_{\mathrm{H}} = \rho^2\mathbf{I}$. Thus all elements of the MIMO channel matrix are uncorrelated (therefore also statistically independent) and have an equal variance of ρ^2. The Rayleigh channel model for the channel matrix can be expressed as follows [16]:

$$\mathrm{H}_{ij} = \mathrm{Normal}(0,{}^{1}\!/\!_{\sqrt{2}}) + \sqrt{-1} \cdot \mathrm{Normal}(0,{}^{1}\!/\!_{\sqrt{2}}) \tag{3.3}$$

where H_{ij} has i.i.d. complex, zero mean, and unit variance entries.

The physical interpretation of this model corresponds to a spatially white MIMO channel which occurs in a rich scattering environment characterized by independent MPCs uniformly distributed in all directions.

3.5.1.2 The Kronecker Model

In [49, 50] it was claimed that the correlation between the powers of two subchannels can be modeled by the product of the correlations as seen from the transmitter and receiver under the Rayleigh assumption. The focus of the Kronecker model is on the second-order moments of the MIMO channel, describing the covariance structure. The channel model is based on the assumption that correlation at the transmitter and receiver are independent of each other, and as such, the full correlation matrix can be separated into the Kronecker product of the transmitter and receiver covariance matrix [42, 51]:

$$\mathbf{R}_{\mathrm{H}} = \mathbf{R}_{\mathrm{H}}^{\mathrm{Tx}} \otimes \mathbf{R}_{\mathrm{H}}^{\mathrm{Rx}} \tag{3.4}$$

where $\mathbf{R}_{\mathrm{H}}^{\mathrm{Tx}}$ and $\mathbf{R}_{\mathrm{H}}^{\mathrm{Rx}}$ are the covariance matrices at the transmitter and receiver sides respectively and $\otimes$ is the Kronecker product matrix. As already mentioned, $\mathbf{R}_{\mathrm{H}}$ is the full channel covariance matrix. The covariance matrices can be defined as:

$$\mathbf{R}_{\mathrm{H}} = \frac{1}{N}\sum_{r=1}^{N}[\mathrm{vec}(\mathbf{H}(r))\mathrm{vec}(\mathbf{H}(\mathrm{r}))^{*}] \tag{3.5}$$

$$\mathbf{R}_{\mathrm{H}}^{\mathrm{Rx}} = \frac{1}{N}\sum_{r=1}^{N}\mathbf{H}(r)\mathbf{H}^{*}(r) \tag{3.6}$$

$$\mathbf{R}_{\mathrm{H}}^{\mathrm{Tx}} = \frac{1}{N}\sum_{r=1}^{N}\left(\mathbf{H}^{*}(r)\mathbf{H}(r)\right)^{\mathrm{T}} \tag{3.7}$$

where N is the number of channel realizations.

Assuming that the MIMO channel coefficients are complex Gaussian, the channel model can be modeled, as in [42, 43, 51], as:

$$\mathbf{H}_{\mathrm{Kron}} = \frac{1}{\sqrt{\mathrm{tr}\{\mathbf{R}_{\mathrm{Rx}}\}}}\mathbf{R}_{\mathrm{Rx}}^{1/2}\mathbf{G}(\mathbf{R}_{\mathrm{Tx}}^{1/2})^{\mathrm{T}} \tag{3.8}$$

where $\mathbf{G}$ is the Gaussian i.i.d. matrix with zero-mean complex normal entries with unit variance, $\sqrt{\mathrm{tr}\{\mathbf{R}_{\mathrm{Rx}}\}} = \sqrt{\mathrm{tr}\{\mathbf{R}_{\mathrm{Tx}}\}} = P_H$, the total energy of the channel, and $(.)^{1/2}$ is defined such that $\mathbf{R}^{1/2}\,(\mathbf{R}^{1/2})^{\mathrm{H}} = \mathbf{R}$.

This model is very popular because of its simple analytical treatment of the MIMO channel and it allows for independent array optimization at the transmitter and receiver. However, the separation of the channel into independent link ends does not accurately describe measured MIMO channels, and some deficiencies of the model have been reported [52, 53]. The inaccuracy becomes more significant with an increase in array size. To overcome the deficiency of the Kronecker model, the Weichselberger model (described next) was developed using eigenmodes.

3.5.1.3 The Weichselberger Model

Unlike the Kronecker model, this model separates the eigenstructure of the full channel covariance matrix, and not the matrix itself, into independent transmitter and receiver sides.

The eigenvalue decompositions of the full channel correlation matrix and the receiver and transmitter covariance matrices are given below:

$$\mathbf{R}_{\mathrm{H}} = \mathbf{U}_{\mathrm{RH}}\mathbf{\Lambda}_{\mathrm{RH}}\mathbf{U}_{\mathrm{RH}}^{\mathrm{H}}, \tag{3.9}$$

$$\mathbf{R}_{\mathrm{Rx}} = \mathbf{U}_{\mathrm{Rx}}\mathbf{\Lambda}_{\mathrm{Rx}}\mathbf{U}_{\mathrm{Rx}}^{\mathrm{H}}, \tag{3.10}$$

and

$$\mathbf{R}_{\mathrm{Tx}} = \mathbf{U}_{\mathrm{Tx}}\mathbf{\Lambda}_{\mathrm{Tx}}\mathbf{U}_{\mathrm{Tx}}^{\mathrm{H}} \tag{3.11}$$

where $\mathbf{U}_{\mathrm{RH}}$, $\mathbf{U}_{\mathrm{Rx}}$and $\mathbf{U}_{\mathrm{Tx}}$ are the spatial eigenbases of the full channel correlation matrix, and the receiver and transmitter covariance matrices respectively.

The eigenbases of the full channel correlation matrix can then be represented by the eigenbasis at the receiver and transmitter as follows:

$$\mathbf{U}_{\mathrm{RH}} = \mathbf{U}_{\mathrm{Rx}} \otimes \mathbf{U}_{\mathrm{Tx}} \tag{3.12}$$

The purpose of this model as described in [7], is to:

1. Describe the spatial structure of the channel jointly, as done with the Virtual Channel Representation (VCR) model, which is described in the next section.
2. Like the Kronecker model, adopt spatial eigenbases to the channel and the array configuration (which includes array geometry, element characteristics, and element polarization).
3. Formulate a model that includes the Kronecker and VCR models as special cases.

The Weichselberger model thus aims to combine the advantages of the Kronecker and VCR models and overcome their deficiencies, and can be represented as follows:

$$\mathbf{H}_{\mathrm{weichsel}} = \mathbf{U}_{\mathrm{Rx}} \left(\tilde{\mathbf{\Omega}} \odot \mathbf{G} \right) \mathbf{U}_{\mathrm{Tx}}^{\mathrm{T}} \tag{3.13}$$

where $\mathbf{G}$ is a random matrix with i.i.d. zero-mean complex normal entries with unit variance, $\odot$ is the element-wise product of two matrices (or the Hadamard product), and $\tilde{\mathbf{\Omega}}$ is the element-wise square root of the coupling matrix $\mathbf{\Omega}$ given by:

$$[\mathbf{\Omega}]_{\mathrm{m,n}} = \mathrm{E}_{\mathbf{H}} \left\{ \left| \mathbf{u}_{\mathrm{Rx,m}}^{\mathrm{H}} \mathbf{H} \mathbf{u}_{\mathrm{Tx,n}}^{*} \right|^2 \right\} \tag{3.14}$$

where $\mathbf{u}_{\mathrm{Rx,m}}$ is the mth eigenvector of the receiver and $\mathbf{u}_{\mathrm{Tx,n}}$ is the nth eigenvector of the transmitter.

Therefore the parameters needed for modeling the channel, as shown in Figure 3.8, are:

- the spatial eigenbasis at the Rx,
- the spatial eigenbasis at the Tx, and
- the average energy of the virtual SISO channel between each eigenmode of the Rx and each eigenmode of the Tx, $\mathbf{\Omega}$, linking the correlation properties of both ends.

FIGURE 3.8: The parameters of the Weichselberger model as taken from [7], where A and B represent Tx and Rx respectively.

When extracting the model parameters from the measured data, the eigenbases are obtained by the eigenvalue decomposition [54] of the transmitting and receiving correlations matrices in Equation 3.7 and Equation 3.6 above. The estimated power coupling matrix is obtained by:

$$\mathbf{\Omega}_{\mathrm{weichsel}} = \frac{1}{N}\sum_{r=1}^{N}\left(\mathbf{U}_{\mathrm{Rx}}^{\mathrm{H}}\mathbf{H}(r)\mathbf{U}_{\mathrm{Tx}}^{*}\right)\odot\left(\mathbf{U}_{\mathrm{Rx}}^{\mathrm{T}}\mathbf{H}(r)\mathbf{U}_{\mathrm{Tx}}\right) \tag{3.15}$$

where N is the number of channel realizations.

When looking at the physical interpretation of the model, the spatial correlation of the transmitting weights determine how much power is radiated into which directions and polarizations. The spatial eigenbases are not affected by the transmitting weights and they reflect the radio environment only, i.e. the number, positions, and strengths of the scatterers. The eigenvalues show how the scatterers are illuminated by the radio waves propagating from the transmitter, and thus they are dependent on the transmitting weights. The coupling matrix

shows the spatial arrangement of the scattering objects and it influences the capacity as well as the number of parallel data streams that can be multiplexed. The coupling matrix also influences the degrees of diversity that are present at the transmitter and receiver. A non-zero element of the coupling matrix establishes a link between the respective eigenmodes. A zero-element of the coupling matrix means that the respective eigenmodes do not couple with each other.

As can be see from Equation 3.13 and Equation 3.16, the Weichselberger and VCR models differ only in the choice of basis matrices where the eigenbases provide a partitioning matched to the radio environment and antenna configurations. Eigenbases are also the only possible basis matrices resulting from independent fading of the bin amplitudes [7]. It should also be noted that the Kronecker model is a special case of the Weichselberger model as it employs rank one coupling.

3.5.2 Propagation-motivated Analytical Models

These models characterize the MIMO channel in terms of propagation parameters.

3.5.2.1 The Virtual Channel Representation (VCR) Model

This model bridges the gap between physical modeling, which describes realistic scattering environments via angles and gains associated with different propagation paths, and stochastic modeling which provide geometric representations of the scattering environment [8]. It captures the essence of the physical model and it provides a linear channel characterization. The VCR model also provides a simple interpretation of the effects of scattering and array characteristics on channel capacity and diversity.

The VCR model, models the MIMO channel in the beamspace instead of the eigenspace and it models the joint spatial behavior of the channel. As shown in Figure 3.9, the angular range of the receiver or transmitter is divided into m Rx or m Tx discrete angular bins (where m is the number of transmitters or receivers). The spatial propagation of the environment between the transmitter and the receiver is partitioned into m Rx $\times$ m Tx virtual DoD-DoA bins.

Mathematically the model can be written as shown in [7]:

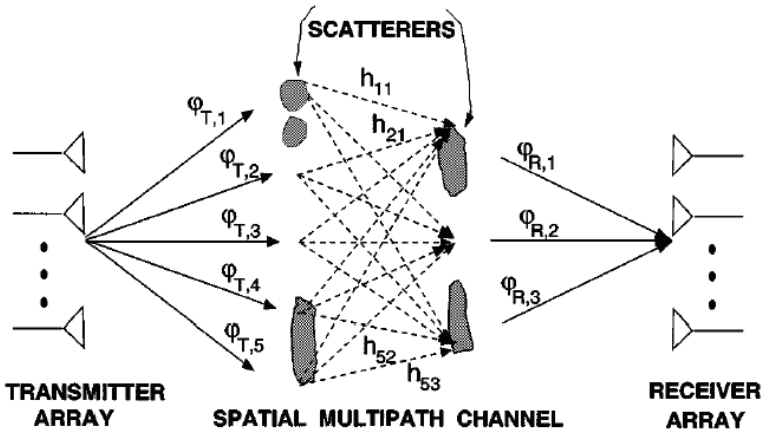

FIGURE 3.9: The virtual channel model as taken from [8].

$$\mathbf{H}_{\text{virtual}} = \mathbf{A}_{\text{Rx}} \left(\tilde{\mathbf{\Omega}}_{\text{virtual}} \odot \mathbf{G} \right) \mathbf{A}_{\text{Tx}}^{\text{T}} \tag{3.16}$$

where $\mathbf{G}$ is a random matrix with i.i.d. zero-mean complex normal entries with unit variance, $\tilde{\mathbf{\Omega}}_{\text{virtual}}$ is the element-wise square root of the coupling matrix given by $\mathbf{\Omega}_{\text{virtual}}$, whose positive read-valued elements determine the average power-coupling between the ith transmitting and jth receiving direction, and $\mathbf{A}_{\text{Rx}}$ and $\mathbf{A}_{\text{Tx}}$ are the steering matrices. The Hadamard product, $\tilde{\mathbf{\Omega}}_{\text{virtual}} \odot \mathbf{G}$, represents the "inner" propagation environment between virtual Tx and Rx scatterers.

The coupling matrix can then be calculated as follows:

$$\mathbf{\Omega}_{\text{virtual}} = \frac{1}{N} \sum_{r=1}^{N} \left(\mathbf{A}_{\text{Rx}}^{\text{H}} \mathbf{H}(r) \mathbf{A}_{\text{Tx}}^{*} \right) \odot \left(\mathbf{A}_{\text{Rx}}^{\text{T}} \mathbf{H}(r) \mathbf{A}_{\text{Tx}} \right) \tag{3.17}$$

where N is the number of channel realizations.

This model is restricted to single polarized uniform linear arrays (ULAs), because if dual polarized antenna configuration is used, the correlation between the two polarizations would have had to be defined a priori in order to be able to specify the steering vectors. Due to the predefined virtual directions, represented by the steering vectors, the assumption of uncorrelated bins becomes an issue [7]. However, with an increase in the number of antenna elements, different DoD-DoA bins see different scatterers [8], which are assumed to fade independently. However, regardless of the number of antenna elements, the angular pattern

of the steering vector shows significant side-lobes in the neighboring bin. Scatterers will thus lie between the virtual directions, resulting in significant contributions of a scatterer in neighboring DoD-DoA bins. Thus the fading amplitudes of neighboring DoD-DoA bins will, in general, be correlated.

Figure 3.10 shows a comparison between the Kronecker, Weichselberger, and VCR models in a study done by [7]. The results of this study will be referred to in Chapter 6.

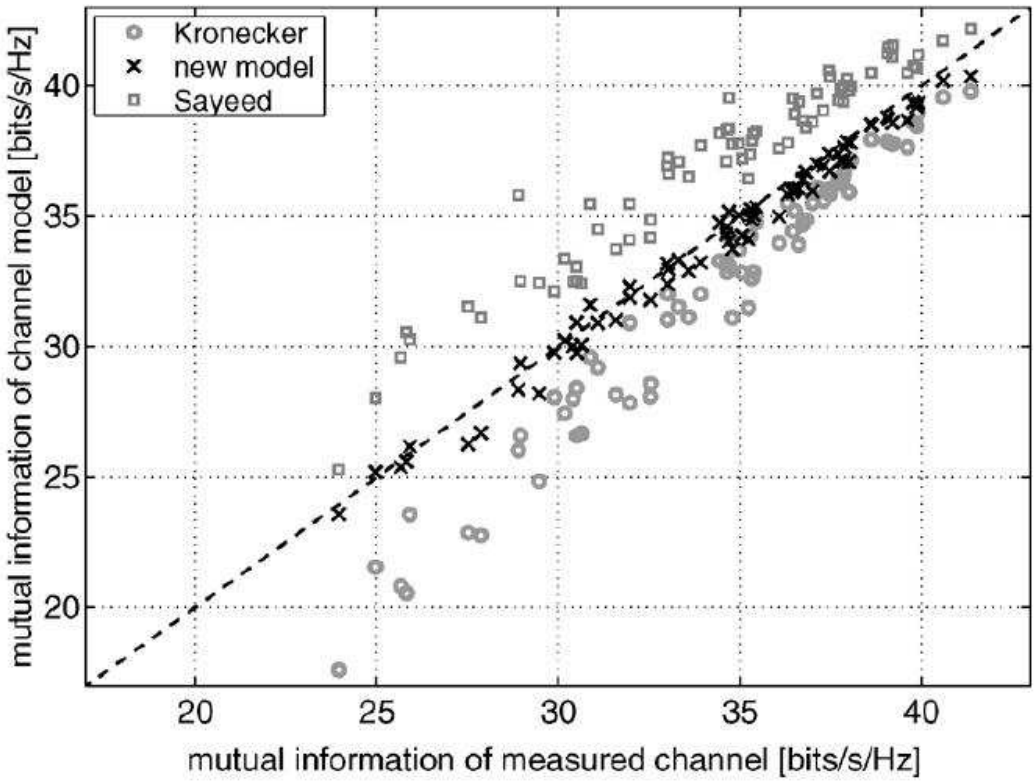

FIGURE 3.10: Comparison of the Kronecker, VCR and Weichselberger Models. As taken from [7].

3.5.2.2 The Finite Scatterer Model

The assumption made in this model is that propagation can be modeled in terms of a finite number of multipath components, and for each component a DoD, DoA, complex amplitude, and delay are specified [55].

As shown in Figure 3.11, the model allows for single-bounce and multi-bounce scattering. It also allows for “split” components, which have a single DoD but subsequently split into two or

more paths with different DoAs (or vice versa). The split can be treated as multiple components having the same DoD (or DoA).

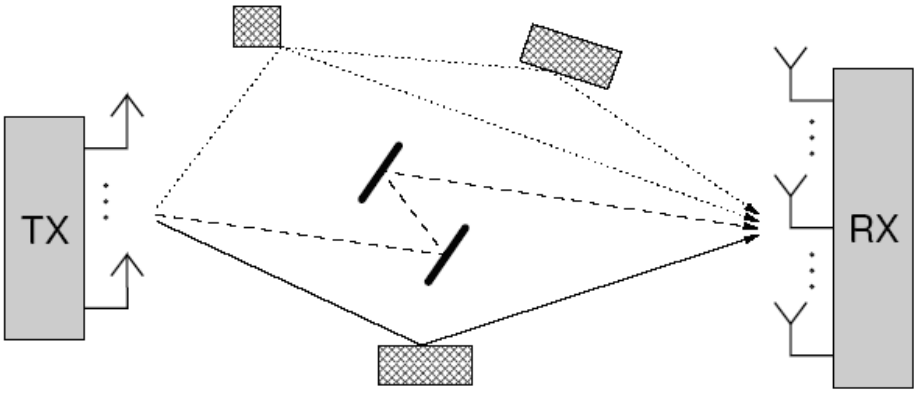

FIGURE 3.11: The finite scatterer model with single-bounce scattering (solid line), multiple-bounce scattering (dashed line), and split components (dotted line) as taken from [4].

3.5.2.3 The Maximum Entropy Model

In this model the distribution of the MIMO channel is determined based on a priori information which includes properties of the propagation environment and system parameters such as bandwidth, DoAs [56], etc. The principle of the model is justified by the objective to avoid any model assumptions not supported by the prior information. It was also shown in [56] that the target application for which the model has to be consistent can influence the proper choice of the model. To maintain consistency, the following axiom was enforced: if the prior information $\mathbf{I_1}$, which is the basis for channel model $\mathbf{H_1}$, is equivalent to the prior information $\mathbf{I_2}$ of the channel model $\mathbf{H_2}$, then both models must be assigned the same probability distribution.

The model is able to translate in a simple way an increase or decrease of prior information into the channel distribution model in a consistent fashion.

3.6 STANDARDIZED MODELS

Table 3.1 gives an overview of all current MIMO standards and their technologies [17]. Standardized models have been defined by various organizations with the intention of being

able to compare different MIMO systems and algorithms to enhance capacity and improve performance. Some of these models are discussed below.

TABLE 3.1: MIMO Standards and the corresponding technology.

Standard	Technology
WLAN 802.11n	OFDM
WiMAX 802.16-2004	OFDM
WiMAX 802.16e	OFDM
3GPP Release 7	WCDMA
3GPP Release 8	OFDM
802.20	OFDM
802.22	OFDM

3.6.1 3GPP Spatial Channel Model (SCM)

This model was developed by 3GPP/3GPP2 to be a common reference for evaluating different MIMO concepts in outdoor environments at a center frequency of 2 GHz and a system bandwidth of 5 MHz. The SCM consists of two parts [57].

3.6.1.1 Link Level Simulations

This is a simple calibration model which is used to compare the performance results of different implementations of a given algorithm. Comparing the performance of the algorithm enables one to determine whether two implementations are equivalent. The calibration model can be implemented as either a correlation model or a ray-tracing model. The SCM parameters that are used to characterize the path include angle spread, AoA (Angle of Arrival) of the Rx, the power azimuth spectrum, antenna pattern, the Tx AoD (Angle of Departure), and Doppler spectrum. The model assumes a single Tx and single Rx.

3.6.1.2 System Level Simulations

This is a physical model that is used for performance simulation. The model distinguishes between three different types of environments: suburban macrocell, urban macrocell, and urban microcell. The model structure and methodology are the same for the three environments, but

the parameters are different. The simulation of the system behavior is carried out as a sequence of "drops", where a "drop" is defined as one simulation run over a certain time period. For each drop, channel parameters are drawn according to distribution functions. The model is antenna independent. When all the parameters and antenna effects are defined, analytical formulations can be extracted from the physical model, where each drop results in a different correlation matrix for the analytical model.

3.6.2 The TGn Channel Model (IEEE 802.11n)

The TGn channel model [58] was developed for indoor Wireless Local Area Networks (WLAN) environments. The model first defines three models which were initially used for SISO WLAN models, and then three additional models are defined with distinct clusters. Each cluster consists of a tap, the power of which is determined so that the overlapping taps which correspond to different clusters, correspond to the sum of the powers of the original power delay profile. The parameters: angular spread, AoA, and AoD are assigned for each tap and cluster using statistical methods. The channel matrix is then determined. Each MIMO channel tap is modeled according to the Kronecker model. The Rx and Tx correlation matrices are determined by the power azimuth spectrum and by array geometry. The TGn model represents six different small environments with different delay spreads.

3.6.3 The COST (European Cooperation in the Field of Scientific and Technical Research) 259 and 273 Models

The COST models are the most general models discussed thus far and the 3GPP and 802.11n models can be viewed as subsets of this model. The two categories of COST models are described below.

3.6.3.1 The COST 259 Directional Channel Model (DCM)

This model is a physical model that gives a model for the delay and angle dispersion at the Tx and Rx for different radio environments [12]. It looks at the relationship between the Tx-Rx distance, delay dispersion and angular spread, etc. It is also defined for different environments (typical urban, bad urban, open square, indoor office, indoor corridor, etc.) which include macrocellular, microcellular, and picocellular scenarios. The modeling approaches for the three

scenarios are different.

Each environment is described by external parameters, such as the Tx position, frequency used, average Tx and Rx height etc., and global parameters which are sets of probability density functions and/or statistical moments characterizing a specific environment. The determination of the global parameters is partly geometric and partly stochastic. The Rx is placed randomly in a cell and a number of scatterer clusters are placed geometrically in the cell. From the positions the relative delay and mean angles of the different clusters that make up the double-directional impulse response can be determined, although the angular spread, delay spread, and shadowing are determined stochastically.

The local parameters are randomly-generated realizations of the global parameters and describe the instantaneous channel behavior. The double-directional channel impulse response is then obtained, from which the channel transfer function is obtained.

The model can handle the continuous movement of the Rx over several propagation environments and also across different environments. Scatterers are however considered stationary, thus channel time variations are only due to Rx movements, and consequently environments where people are moving around are excluded. Further delay attenuations are modeled as Gaussian random variables, which require a sufficiently large number of MPCs within each delay bin, also a condition which is not met in all cases.

3.6.3.2 COST 273

Even though the two COST models are similar there are a few important differences. Firstly, a number of new radio environments and parameters have been defined. The modeling approach for the macrocells, microcells, and picocells are all the same. However the modeling of the distribution DoAs and DoDs is different. Two representations of the cluster are defined: one as seen from the Tx and the other as seen from the Rx. Both cluster representations look identical and are linked via a stochastic cluster link delay, which is the same for all scatterers inside a cluster. The link delay ensures realistic path delays as per measurement campaigns, but the placement of the cluster is determined by the angular statistics of the cluster as observed from the Tx or Rx respectively.

3.7 CHAPTER SUMMARY

This chapter looked at MIMO channel models and measurement techniques. Transfer matrix measurements are a direct way of measuring the channel matrix. The measurement campaign involves setting up a physical communication link to measure the impulse responses between the transmitter and receiver. Although direct measurement techniques are able to capture real-world MIMO characteristics, the setting up of measurement equipment can be time consuming, difficult, and expensive.

Physical models have thus been developed to characterize the physical multipath propagation between the transmitter and the receiver and can be categorized as deterministic, geometry-based stochastic and non-geometrical stochastic models. Deterministic models reproduce the actual geometrical and electromagnetic characteristics of an environment. The ray-tracing method is the most popular of these models. Although the ray-tracing method is a reasonably accurate method, it is site specific and simplification of the geometry of the environment that is represented can lead to underestimation of the MIMO channel capacity. The computational costs of the ray-tracing simulations are also very high.

Geometry-based stochastic models model scatterers around the transmitter and the receiver in a stochastic fashion according to a certain probability distribution function. The double scattering model and distributed scattering model are examples of the geometry-based model. Non-geometrical stochastic models describe paths from the transmitter to the receiver by statistical parameters only, without reference to the geometry of the physical environment. The extended SVM and the Zwick model are two examples of this type of model. Another type of model that characterizes the channel transfer function in a mathematical way, without measurements, is the analytical model.

Analytical models can be categorized into correlation-based analytical models and propagation motivated analytical models. Correlation-based models characterize the MIMO channel matrix statistically in terms of the correlations between matrix entries. The Gaussian i.i.d. model, the Kronecker model and the Weichselberger model are examples of such a model. The propagation-motivated models characterize the MIMO channel in terms of propagation parameters. The virtual channel representation, the finite scatterer model, and the maximum

entropy models are examples of such a model.

Finally, standardized models have been established by using some of the models described above so that these models were agreed on by different organizations. Examples of these models include 3GPP SCM, link level simulations, system level simulations, IEEE 802.11n, and the COST 259 and 273 models.

CHAPTER FOUR
MEASUREMENT CAMPAIGN

This chapter describes the environment in which the MIMO system was used to take measurements. As this study does not involve the actual measurement of data, only a brief description of the system is given. The various steps involved in the analysis of the data are also discussed.

4.1 MEASUREMENT ENVIRONMENT

MIMO transfer matrix measurements were carried out at different locations in an industrial and office environment as described below.

The measurements in the industrial environment were carried out at the Heavy Machinery Lab (HML) at the University of Pretoria. As shown in Figure. 4.1, the transmitter (Tx) was placed at the entrance of the room and the receiver (Rx) was placed at six different locations within the room. Actual measurement pictures at various locations are given in Figures 4.2 - 4.4.

The HML environment is mainly comprised of brick walls, concrete floors, wooden doors (except for the entrance which consists of a glass door), and fluorescent lights. The equipment in the lab comprises machinery, a Gaussian cage, and metallic work benches with rubber surfaces.

The office measurements were carried out at the Carl and Emily Fuchs Institute of Microelectronics (CEFIM) also at the University of Pretoria. As shown in Figure 4.5, the Tx was placed at a single fixed position in the corridor and the Rx was placed at eleven

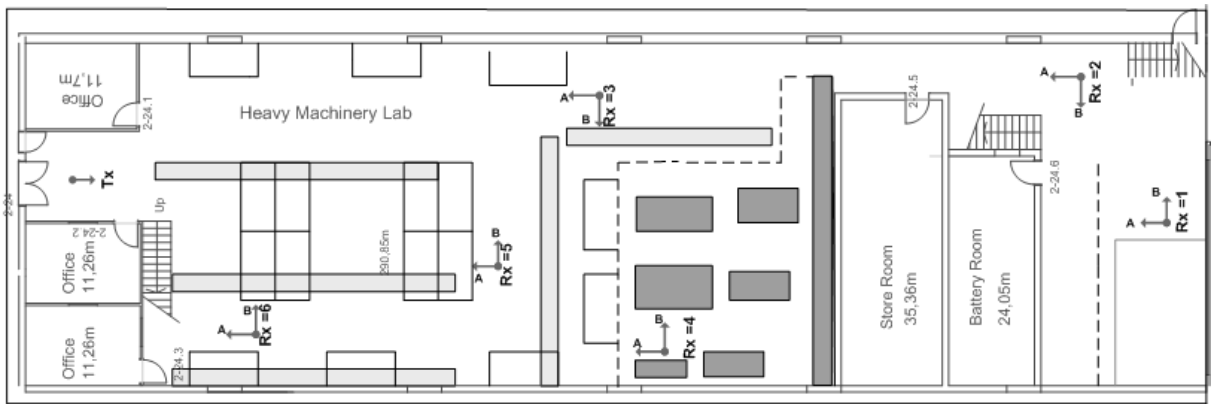

FIGURE 4.1: The HML layout showing the transmitter and the receiver. Rx = n refer to the locations where the receiver was placed. Arrows show the orientation of the arrays for the different cases.

FIGURE 4.2: The receiver at location 3 with orientation B, with the transmitter (encircled) shown in the background near the entrance of the lab.

FIGURE 4.3: The receiver at location 4 with orientation A.

FIGURE 4.4: The receiver at location 6 with orientation B.

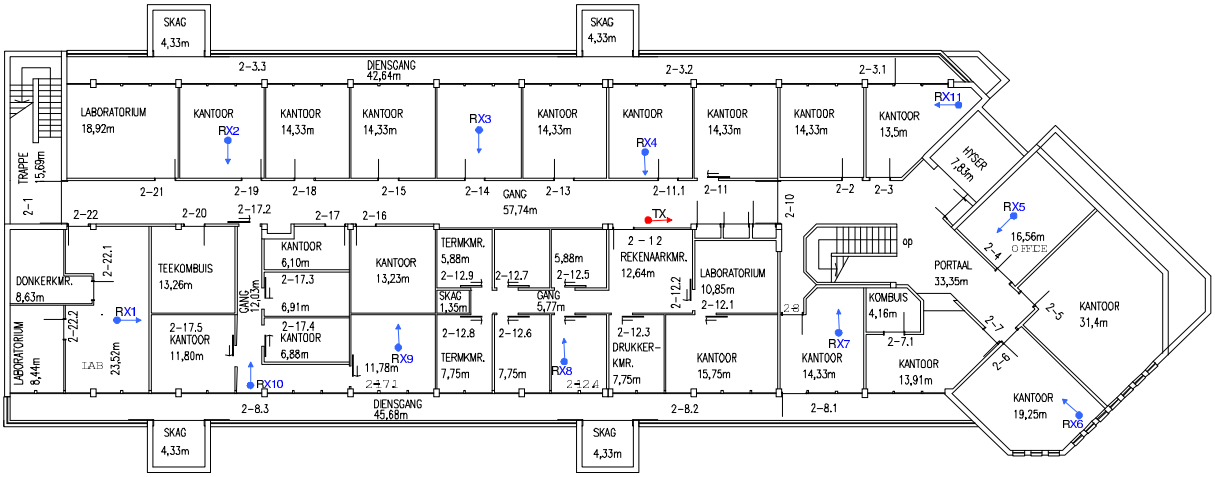

FIGURE 4.5: The CEFIM layout showing the transmitter and the receiver. Rx = n refer to the locations where the receiver was placed.

FIGURE 4.6: The location of the transmitter along the corridor in CEFIM.

FIGURE 4.7: The position of the receiver at location 6.

FIGURE 4.8: The position of the receiver at location 5.

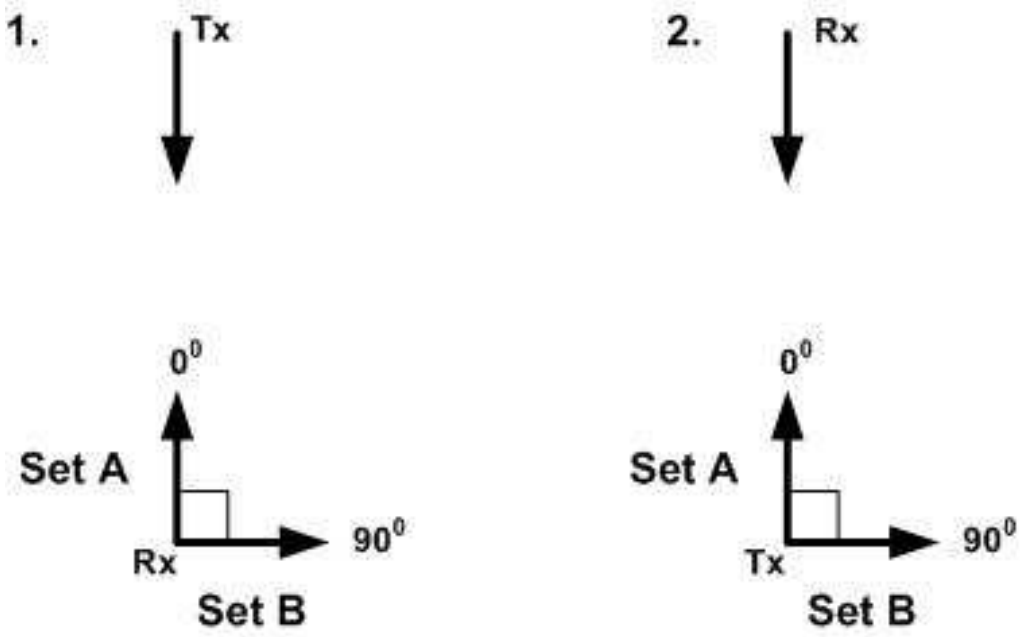

FIGURE 4.9: 1. The orientation of the Rx in relation to the Tx in HML. 2. The orientation of the Tx in relation to the Rx in CEFIM.

different office and laboratory locations. Actual measurement pictures at various locations are given in Figures 4.6 - 4.8.

The CEFIM environment typically consists of drywall partitioning, carpeted floors, wooden doors, and fluorescent lights. The corridors are lined with laminated posters, metallic bins, and chairs. All rooms contain furniture, whiteboards, air conditioners, steel air vents, computer equipment, and large windows covering the width of the room.

In the HML, two Rx orientations were considered (0^0 and 90^0 relative to Tx), and in CEFIM, two Tx orientations were considered (0^0 and 90^0 relative to Rx). These two orientations are referred to as Set A and B respectively (see Figure 4.9). Both the 2.4 GHz and 5.2 GHz measurements were taken at the same positions.

4.2 MEASUREMENT SYSTEM AND DATA REPRESENTATION

The measurement campaign was carried out with a wideband channel sounder, as explained in [59, 60], which is able to probe microwave bands from 2 GHz to 8 GHz using 80 MHz

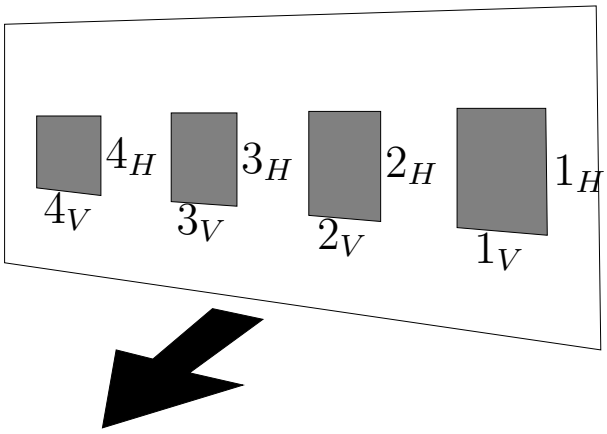

FIGURE 4.10: Dual-polarized patch array employed for measurements. Each element has ports to excite linear vertical (V-pol) and horizontal (H-pol) polarization.

of instantaneous bandwidth with eight transmitters and eight receivers in a switched antenna architecture. The measurements were taken at 2.4 GHz and 5.2 GHz using dual-polarized linear patch arrays, with $\lambda/2$ inter-element spacing at both the transmitter and the receiver. This is shown schematically in Figure 4.10.

The channel data obtained from the measurements can be represented in matrix format as $\mathbf{H}(1:\mathrm{f}, 1:\mathrm{n_{Rx}}, 1:\mathrm{n_{Tx}}, 1:\mathrm{n_S}, 1:\mathrm{n_{Snap}})$ and the size of each of the elements is represented as $\mathbf{H}(1:81, 1:8, 1:8, 1:2, 1:20)$. Considering that such a five-dimensional (5-D) matrix would be too complex to perform calculations on, and based on several factors which are discussed below, a sub-matrix of the channel matrix is extracted.

Two different signal sequences, $\mathrm{n_S}$, are used to carry out the measurements. It was however found that the data from both sequences were similar, thus only one of the sequences is used in the calculations. The frequency bin, f, is a one-to-one representation of the instantaneous bandwidth. Although the measurement system is capable of probing channels with 80 MHz of instantaneous bandwidth, only 30 MHz of bandwidth is used in this study. This is consistent with the limited operation of the narrowband patch elements and therefore only 31 frequency bins are used for the calculations. The $\mathrm{n_{Rx}}$ and $\mathrm{n_{Tx}}$ elements represent the number of receivers and transmitters. At each location in the two environments, 20 channel snapshots, $\mathrm{n_{Snap}}$, are recorded with 200 ms between snapshots. However, as was reported in [59], very little change is noticed over the 4 s acquisition time because the Tx and Rx are stationary during measurements, thus for calculation purposes only a single snapshot is considered. The sub-matrix of the

channel used for calculations is given as $\mathbf{H}(1:31, 1:8, 1:8, 1, 10)$.

4.3 DATA PROCESSING AND ANALYSIS

The various steps involved in the data processing and analysis are shown in Figure 4.11 and are discussed in greater detail below.

4.3.1 Extraction of the Polarization Subsystems

Considering the measurements were taken using dual-polarized antennas at the receiver and transmitter, the 8×8 channel matrix can be represented as:

$$\mathbf{H} = \begin{bmatrix} \mathbf{H_{VV}} & \mathbf{H_{HV}} \\ \mathbf{H_{VH}} & \mathbf{H_{HH}} \end{bmatrix} \tag{4.1}$$

where $\mathbf{H_{IJ}}$ is a subchannel matrix consisting of the polarization I and J at the Rx and Tx, respectively.

For the purpose of analyzing systems employing different polarizations, 4×4 subsets are extracted from the full 8×8 channel matrix. The response of a V-pol or H-pol system is given directly by $\mathbf{H_{VV}}$ and $\mathbf{H_{HH}}$, which use antenna elements $\{1_V, 2_V, 3_V, 4_V\}$ or $\{1_H, 2_H, 3_H, 4_H\}$ respectively. The dual-pol system can be analyzed using either the outer elements, $\{1_H, 1_V, 4_H, 4_V\}$, or the inner elements $\{2_H, 2_V, 3_H, 3_V\}$. For the purposes of this study the outer elements were chosen.

4.3.2 Channel Normalization

In order to preserve changes in the received power with position, channels are normalized to ensure average unit SISO gain for the complete environment (but not for each location). Entries in the channel matrix corresponding to a different polarization than the transmitted polarization will be weaker than entries corresponding to the transmitted and received entries of the same polarization. Thus, to retain the relative power of the various polarizations, co-polarized matrices, and not cross-polarized matrices, are used for the normalization [25, 61].

The normalization is computed as $\tilde{\mathbf{H}}^{(m,n)} = \alpha^{-1/2}\mathbf{H}^{(m,n)}$ with

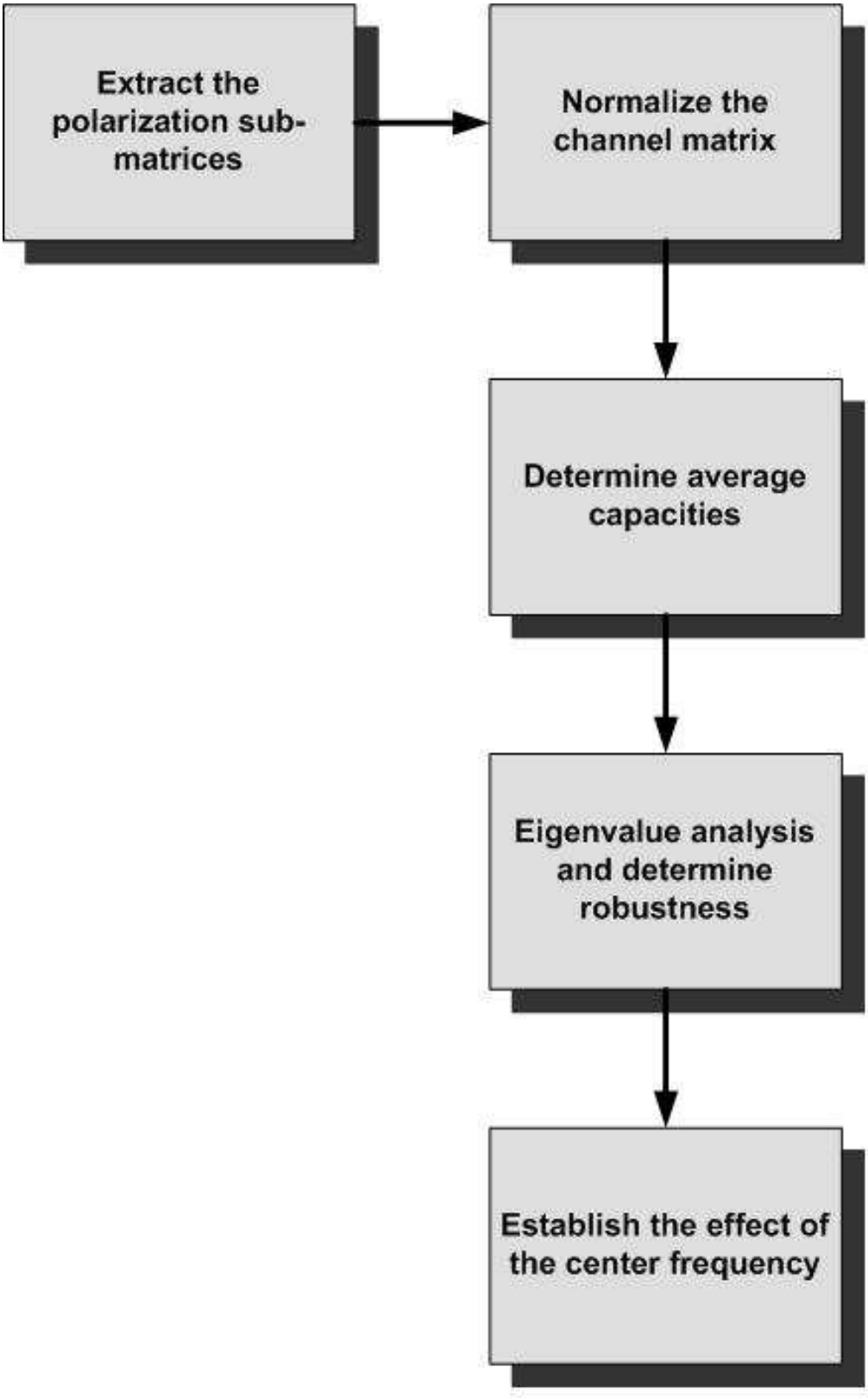

FIGURE 4.11: A flowchart of the measurement data processing.

$$\alpha = \frac{1}{N_r N_t N_f N_l} \sum_{n=1}^{N_l} \sum_{m=1}^{N_f} \left(\left\| \mathbf{H_{VV}}^{(m,n)} \right\|_F^2 + \left\| \mathbf{H_{HH}}^{(m,n)} \right\|_F^2 \right) /2 \tag{4.2}$$

where $\tilde{\mathbf{H}}^{(m,n)}$ and $\mathbf{H}^{(m,n)}$ are the respective measured and normalized channel matrices for the mth frequency bin at location n, $\|\cdot\|_F$ is Frobenius norm, and N_r, N_t, N_f and N_l are the number of receivers, transmitters, frequency bins, and locations respectively.

An example of normalized, 4×4 dual-pol, V-Pol and H-Pol subsystems is given below:

$$\tilde{\mathbf{H}}_{\mathbf{HV}} = \begin{bmatrix} 1.0046 + 0.6531\text{i} & -0.0425 - 0.5620\text{i} & 0.9368 - 0.1110\text{i} & -0.2182 - 0.6226\text{i} \\ -0.6248 - 0.7726\text{i} & -2.3897 - 0.9446\text{i} & 0.0357 - 0.3951\text{i} & -1.4581 - 1.1387\text{i} \\ -0.0956 + 0.3328\text{i} & -0.9051 + 0.1678\text{i} & -0.5259 - 0.5487\text{i} & -0.8710 - 0.4271\text{i} \\ -0.7315 - 0.0479\text{i} & -2.6781 - 0.5956\text{i} & -0.4560 - 0.1212\text{i} & -2.1479 + 1.1832\text{i} \end{bmatrix}$$

$$\tilde{\mathbf{H}}_{\mathbf{VV}} = \begin{bmatrix} 1.0046 + 0.6531\text{i} & -0.0291 - 0.3639\text{i} & -0.5530 + 0.5371\text{i} & 0.9368 - 0.1110\text{i} \\ 0.0095 - 1.2013\text{i} & -0.6571 + 0.8676\text{i} & 1.4872 + 0.1105\text{i} & -0.6274 - 1.0870\text{i} \\ -0.8615 + 0.3488\text{i} & 0.1505 - 0.5917\text{i} & -0.3709 - 0.0314\text{i} & 0.6100 + 0.5492\text{i} \\ -0.0956 + 0.3328\text{i} & -0.1126 + 0.7106\text{i} & 0.5596 - 0.2022\text{i} & -0.5259 - 0.5487\text{i} \end{bmatrix}$$

$$\tilde{\mathbf{H}}_{\mathbf{HH}} = \begin{bmatrix} -2.3897 - 0.9446\text{i} & 1.0443 + 3.1163\text{i} & 1.4775 - 2.0283\text{i} & -1.4581 - 1.1387\text{i} \\ 0.6269 + 2.6120\text{i} & 1.5041 - 2.0263\text{i} & -2.2670 + 0.0657\text{i} & 0.8975 + 1.2177\text{i} \\ 1.7680 - 1.7021\text{i} & -2.0301 - 0.3243\text{i} & 0.9341 + 1.5681\text{i} & 0.4514 - 1.2883\text{i} \\ -2.6781 - 0.5956\text{i} & 0.8563 + 2.6042\text{i} & 0.8501 - 2.3848\text{i} & -2.1479 + 1.1832\text{i} \end{bmatrix}$$

4.3.3 Channel Capacity

This study focuses on the performance of the MIMO system, thus uninformed transmit channel capacity is computed as [16]:

$$C = \log_2 \det \left[\mathbf{I} + \frac{\rho}{N_t} \tilde{\mathbf{H}} \tilde{\mathbf{H}}^{\mathrm{H}} \right], \tag{4.3}$$

where $\mathbf{I}$ is the identity matrix, ρ is the assumed average SISO SNR, $\tilde{\mathbf{H}}$ is the normalized channel matrix, and $(.)^{\mathrm{H}}$ is the conjugate matrix transpose. A reference SNR of 20 dB is used

in the calculations.

For the purposes of this study, the average capacity is used as a performance metric. Two types of average capacities are considered: average capacity at each location and average capacity of the entire environment (which will hereon be referred to as the bulk average capacity). These capacities are calculated for the three polarization subsystems at the different center frequencies and for the two different orientations.

The total capacity of a location is calculated as the sum of the capacities over the m frequency bins at that location:

$$\begin{aligned} C_{\text{Loc}} &= \sum_{m=1}^{N_f} C^{(m)} \\ &= \sum_{m=1}^{N_f} \log_2 \det \left[\mathbf{I} + \frac{\rho}{N_t} \tilde{\mathbf{H}}_{\mathbf{IJ}}^{(m)} (\tilde{\mathbf{H}}_{\mathbf{IJ}}^{(m)})^{\text{H}} \right] \end{aligned} \tag{4.4}$$

where $\tilde{\mathbf{H}}_{\mathbf{IJ}}^{(m)}$ represents the dual-pol, V-Pol or H-Pol channel matrices for the mth frequency bin.

The average capacity at each location is determined by Equation 4.5 and the bulk average capacity is determined as in Equation 4.6:

$$\overline{C}_{\text{Loc}} = \frac{C_{\text{Loc}}}{N_f} \tag{4.5}$$

$$\overline{C}_{\text{Environment}} = \frac{\sum_{n=1}^{N_l} \overline{C}_{\text{Loc}}^{(n)}}{N_l} \tag{4.6}$$

4.3.4 Eigenvalue Analysis and Subsystem Robustness

To further advance the comparisons between the polarization subsystems, the eigenvalue distribution and robustness are determined.

4.3.4.1 Eigenvalue Distribution

The singular value decomposition of the channel matrix is given as follows:

$$\tilde{\mathbf{H}} = \mathbf{U}\mathbf{\Sigma}\mathbf{V}^{\mathrm{H}} \tag{4.7}$$

where $\mathbf{U}$ and $\mathbf{V}$ are the respective unitary matrices of the left and right singular vectors and $\mathbf{\Sigma}$ is a triangular matrix with l singular values on the main diagonal, where $l = \min\{N_r, N_t\}$.

The eigenvalues in dB of the channel are computed as the squares of the singular values of $\tilde{\mathbf{H}}$ as follows:

$$\lambda = 20\log_{10}(\mathbf{\Sigma}) \tag{4.8}$$

where λ contains l eigenvalues. In [41] the lth eigenvalue was shown to represent the power gain of the lth channel.

The rank of the channel is determined by the number of non-zero singular values k, disclosing how many parallel data streams (or subchannels) the channel consists of. The rank of the channel matrix is given by:

$$\mathrm{rank}(\tilde{\mathbf{H}}) = k \leq \min\{N_t, N_r\} \tag{4.9}$$

It has been noted that a rich scattering environment results in high channel rank [6].

When implementing the above equations in this study, the singular values of the channel matrices at each location are found through the singular value decomposition of the channel matrices over the m frequency bins:

$$\mathbf{\Sigma}_{\mathrm{Loc}}^{(m)} = \mathrm{svd}(\tilde{\mathbf{H}}_{\mathbf{IJ}}^{(m)}) \tag{4.10}$$

where $\mathbf{\Sigma}_{\mathrm{Loc}}^{(m)}$ contains l singular values at each mth frequency bin.

The eigenvalues at each location and for each mth frequency bin is calculated as follows:

$$\lambda_{\mathrm{Loc}}^{(m)} = 20\log(\mathbf{\Sigma}_{\mathrm{Loc}}^{(m)}) \tag{4.11}$$

where $\lambda_{\mathrm{Loc}}^{(m)}$ consists of l eigenvalues.

Each of the l eigenvalues is plotted by finding the cdf of the bulk l eigenvalues in the environment. The lth eigenvalue is determined across each of the locations and frequency bins:

$$\lambda^{(l)}_{\text{Environment}} = \text{res}(\lambda^{(l)}_{\text{Loc}}, 1, N_l N_f) \tag{4.12}$$

where the res(A) returns, in this case, a $1 \times N_l N_f$ matrix B whose elements are taken column-wise from A. Only the two dominant eigenvalues are plotted for analysis purposes. Examples of the singular value decomposition and the corresponding eigenvalues of the $\tilde{\mathbf{H}}_{\mathbf{VV}}$ subsystem, shown previously, are given below:

$$\mathbf{\Sigma} = \begin{bmatrix} 3.3315 \\ 1.3629 \\ 0.3222 \\ 0.1942 \end{bmatrix}$$

$$\lambda = \begin{bmatrix} 24.0685 \\ 6.1930 \\ -22.6497 \\ -32.7771 \end{bmatrix}$$

4.3.4.2 Robustness

In [62] it was stated that decorrelated antenna elements make MIMO systems more robust. It was also found that when antenna correlation is low, eigenvalues of the channel are almost equal. To determine the equality of the eigenvalues, the eigenvalue ratio [63] or eigenvalue spread [64] is determined:

$$EV\,Ratio = \frac{\lambda_{\max}}{\lambda_{\min}} \tag{4.13}$$

$$EV\,Spread = \lambda_{\max}[\text{dB}] - \lambda_{\min}[\text{dB}] \tag{4.14}$$

where $\lambda_{\max}$ and $\lambda_{\min}$ are the largest and smallest eigenvalues of the channel. If the eigenvalue spread or ratio is small the signals are approximately uncorrelated.

In this study a robust system can be defined as one that can provide at least two subchannels (as only the two dominant eigenvalues are taken into consideration for analysis purposes) of almost equal gain. The robustness of the subsystems is determined by the ratio of the first two dominant eigenvalues at the mth frequency bin, as given by:

$$\lambda^{(m)}_{\text{Loc\_Spacing}} = 10\log(\lambda_1^{(m)} \Big/ \lambda_2^{(m)}) \tag{4.15}$$

Thus the lower the spacing, the more robust the system is. The cdf of the bulk ratios is found similar to Equation 4.12.

4.3.5 Correlation of the Center Frequency Capacities

The effect of center frequency compares the performance of the systems at the two center frequencies namely 2.4 GHz and 5.2 GHz. It also determines whether frequency scaling can be applied.

As part of the frequency scaling study, the similarity of the capacities at 2.4 GHz and 5.2 GHz is evaluated by calculating the correlation coefficient of the capacities at the two frequencies as follows:

$$\rho = \frac{\sum_{m=1}^{N_l} \left(C_{2.4}^{(m)} - \overline{C}_{2.4}\right)\left(C_{5.2}^{(m)} - \overline{C}_{5.2}\right)}{\sqrt{\left[\sum_{m=1}^{N_l} \left(C_{2.4}^{(m)} - \overline{C}_{2.4}\right)^2\right]\left[\sum_{m=1}^{N_l} \left(C_{5.2}^{(m)} - \overline{C}_{5.2}\right)^2\right]}}, \tag{4.16}$$

where ρ is the correlation coefficient, N_l is the number of locations in each environment, $C_{2.4}^{(m)}$ is the average capacity for each location at 2.4 GHz, $C_{5.2}^{(m)}$ represents the average capacities at 5.2 GHz, and $\overline{C}_{2.4}$ and $\overline{C}_{5.2}$ refers to the average capacity over all N_l locations.

This study also involves the comparison of the measured data with the Kronecker and Weichselberger models. However, the channel matrix data used in the model evaluation are different from the data used in the above equations, thus analysis of the models will be discussed in Chapter 6.

4.4 CHAPTER SUMMARY

This chapter focuses on the measurement activities of this study. As the actual measurement campaign is part of another study, only a brief description of the measurement equipment and the measurement campaign was provided. An 8×8 dual-polarized MIMO system, employing linear patch antennas, was used to carry out measurements in an office and industrial environment.

The office measurements were conducted in CEFIM by placing the transmitter at a fixed position along the corridor and placing the receiver at eleven different positions throughout the building. The environment typically consists of drywall partitioning, carpeted floors, wooden doors, and fluorescent lights. The corridors are lined with laminated posters, metallic bins, and chairs. All rooms contain furniture, whiteboards, air conditioners, steel air vents, computer equipment, and large windows covering the width of the room.

The industrial measurements were conducted in HML by placing the transmitter at a fixed location at the entrance of the lab, and the receiver at six different locations within the lab. The environment is mainly comprised of brick walls, concrete floors, wooden doors (except for the entrance which consists of a glass door), and fluorescent lights. The equipment in the lab comprises machinery, a Gaussian cage, and metallic work benches with rubber surfaces.

The dual-polarized channel matrix was extracted from the 5-D measured data was represented as $\mathbf{H}(1:\mathrm{f}, 1:\mathrm{n_{Rx}}, 1:\mathrm{n_{Tx}}, 1:\mathrm{n_S}, 1:\mathrm{n_{Snap}})$, where f, is the number of frequency bins; $\mathrm{n_{Rx}}$ and $\mathrm{n_{Tx}}$ represent the number of receivers and transmitters; $\mathrm{n_S}$ is the signal sequence used; and $\mathrm{n_{Snap}}$ is the number of snapshots. The channel matrix was then normalized across the entire environment from which the measurements were taken using the co-polarized (single-pol) matrix entries, as was shown in Equation 4.2. For comparison, three 4×4 subsystems were extracted from the channel matrices i.e. H-pol, V-pol and Dual-pol. Considering that the focus of the study is on the performance of the MIMO system, the capacity was computed as in Equations 4.4 - 4.6. The eigenvalue analysis was performed using Equations 4.10 - 4.12. Robustness was determined with Equation 4.15. The effects of frequency scaling were studied using Equation 4.16.

CHAPTER FIVE
MIMO SYSTEM PERFORMANCE

The results from the measurement campaign described in Chapter 4 are discussed in this section.

5.1 AVERAGE CAPACITIES AT CEFIM AND HML

The bulk average capacities of the measurement MIMO system in the HML and CEFIM environment are given in Table 5.1 and Table 5.2 respectively. The capacities are represented in terms of the center frequency, polarization, and antenna orientation.

None of the bulk average capacities achieved the ideal capacity of a 4×4 i.i.d. Gaussian channel (27 bits/s/Hz), but rather only provided 45% to 70% of this maximum value. For the single V-pol and H-pol cases, the reduced capacity indicates limited multipath and higher spatial correlation. Although the dual-pol array increases the conditioning of the channel (as will be shown later), the capacity level is not significantly different from the single-pol cases due to the reduced receiving power gain, which is a result of the weak cross-pol subchannels. In other words, when using dual-polarization, the increase in rank and the reduction in power appear to approximately cancel one another out.

The capacity performances of HML and CEFIM are similar, however the main difference occurs with frequency dependence. Performance at 5.2 GHz is better than performance at 2.4 GHz for HML, and performance at 2.4 GHz is better than performance at 5.2 GHz for CEFIM. This could partially be due to the different nature of propagation in the two environments. In CEFIM, transmission through walls should be significant and transmitted waves would likely suffer more attenuation at 5.2 GHz, which could perhaps lead to less total multipath at the

Table 5.1: Bulk average capacities in HML with respect to antenna polarization and orientation, and carrier frequency.

		2.4GHz [b/s/Hz]	5.2GHz [b/s/Hz]
Dual-Pol	Set A	15.0	17.1
	Set B	16.9	17.9
V-Pol	Set A	14.3	13.9
	Set B	14.4	14.9
H-Pol	Set A	15.0	16.6
	Set B	17.0	18.9

Table 5.2: Bulk average capacities in CEFIM with respect to antenna polarization and orientation, and carrier frequency.

		2.4GHz [b/s/Hz]	5.2GHz [b/s/Hz]
Dual-Pol	Set A	18.1	14.8
	Set B	18.0	15.0
V-Pol	Set A	16.7	12.6
	Set B	16.2	11.8
H-Pol	Set A	18.9	16.0
	Set B	18.0	16.1

receiver. In HML, on the other hand, propagation mainly consists of reflected and diffracted waves. This is because of the large metal obstacles which remove any differences due to frequency-dependent transmissions through the walls.

The average capacities at each of the the six locations for HML is given in Table 5.3 and Table 5.4 for measurements at 2.4 GHz and 5.2 GHz respectively. The average capacities at each of the eleven locations for CEFIM is given in Table 5.5 and Table 5.6 for measurements at 2.4 GHz and 5.2 GHz respectively.

Observing the channel rank for both CEFIM and HML as shown in Figure 5.1 at locations where high capacity is attained, it can be observed that a channel rank of up to 3 can be achieved. However, at locations of low capacity, as shown in Figure 5.2, a channel rank of

TABLE 5.3: Average capacities at each of the six locations in HML at 2.4 GHz.

Location	Dual-Pol [b/s/Hz]	V-Pol [b/s/Hz]	H-Pol [b/s/Hz]
1	15.06	13.84	14.10
2	13.46	10.71	11.05
3	18.72	17.62	18.19
4	13.15	9.95	14.38
5	14.95	15.07	17.06
6	23.09	18.91	21.44

TABLE 5.4: Average capacities at each of the six locations in HML at 5.2 GHz.

Location	Dual-Pol [b/s/Hz]	V-Pol [b/s/Hz]	H-Pol [b/s/Hz]
1	12.07	9.87	11.91
2	14.59	8.99	12.06
3	21.30	19.10	22.05
4	15.59	14.89	16.37
5	18.59	16.25	23.73
6	22.87	17.41	20.47

only 1 can be attained. The rank of the channel is determined by the number of eigenvalues, disclosing how many parallel data streams (or subchannels) the channel consists of and what the power gains of these subchannels are.

Although the capacities achieved in both CEFIM and HML are not very high, channel ranks of up to 3 can be achieved. This suggests that the MIMO system is suitable for use in both office and industrial environments.

5.1.1 Antenna Polarization and Orientation

The bulk average capacity values for HML in Table 5.1 suggest that the systems can be ranked in order of decreasing performance as H-pol, dual-pol, and V-pol. The same ranking is also found for CEFIM. These results are somewhat opposite to previous work [25, 32], where it has been found that the V-pol suffers less attenuation and exhibits higher capacity. It is likely that

TABLE 5.5: Average capacities at each of the eleven locations in CEFIM at 2.4 GHz.

Location	Dual-Pol [b/s/Hz]	V-Pol [b/s/Hz]	H-Pol [b/s/Hz]
1	14.59	13.83	15.30
2	17.69	16.71	17.93
3	18.12	17.10	19.19
4	25.78	21.54	24.67
5	16.53	14.84	14.26
6	16.76	15.95	15.82
7	16.36	12.23	17.74
8	18.92	15.71	18.65
9	20.12	18.21	20.57
10	18.13	18.10	21.27
11	16.64	16.96	17.87

TABLE 5.6: Average capacities at each of the eleven locations in CEFIM at 5.2 GHz.

Location	Dual-Pol [b/s/Hz]	V-Pol [b/s/Hz]	H-Pol [b/s/Hz]
1	4.65	4.68	4.78
2	15.16	12.61	14.07
3	18.13	16.07	22.42
4	24.31	20.75	26.10
5	14.07	10.86	13.96
6	12.24	13.87	8.22
7	19.62	12.94	20.93
8	18.34	12.66	18.87
9	11.18	8.45	14.02
10	9.19	7.44	11.73
11	17.24	14.24	19.16

the difference stems from the radiation patterns of the antennas. For the square patches that were employed, H-pol elements have a wider 3 dB beamwidth ($120°$) in the azimuthal plane than V-pol ($90°$) elements, meaning that the amount of multipath and total collected power for

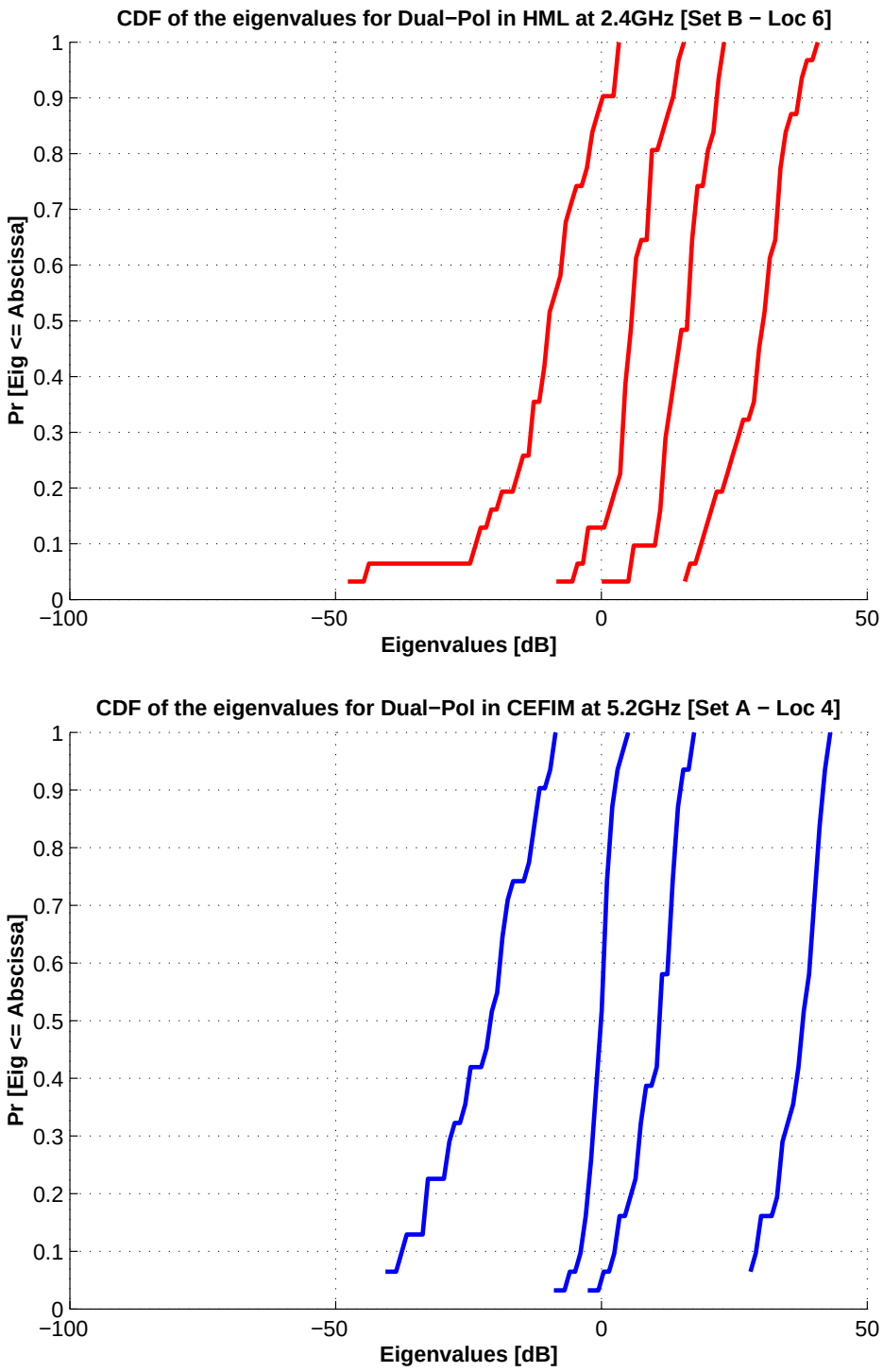

FIGURE 5.1: The channel rank of locations, in HML and CEFIM respectively, with high capacity.

H-pol should be higher, if any differences due to polarization-dependent effects of the channel, are ignored.

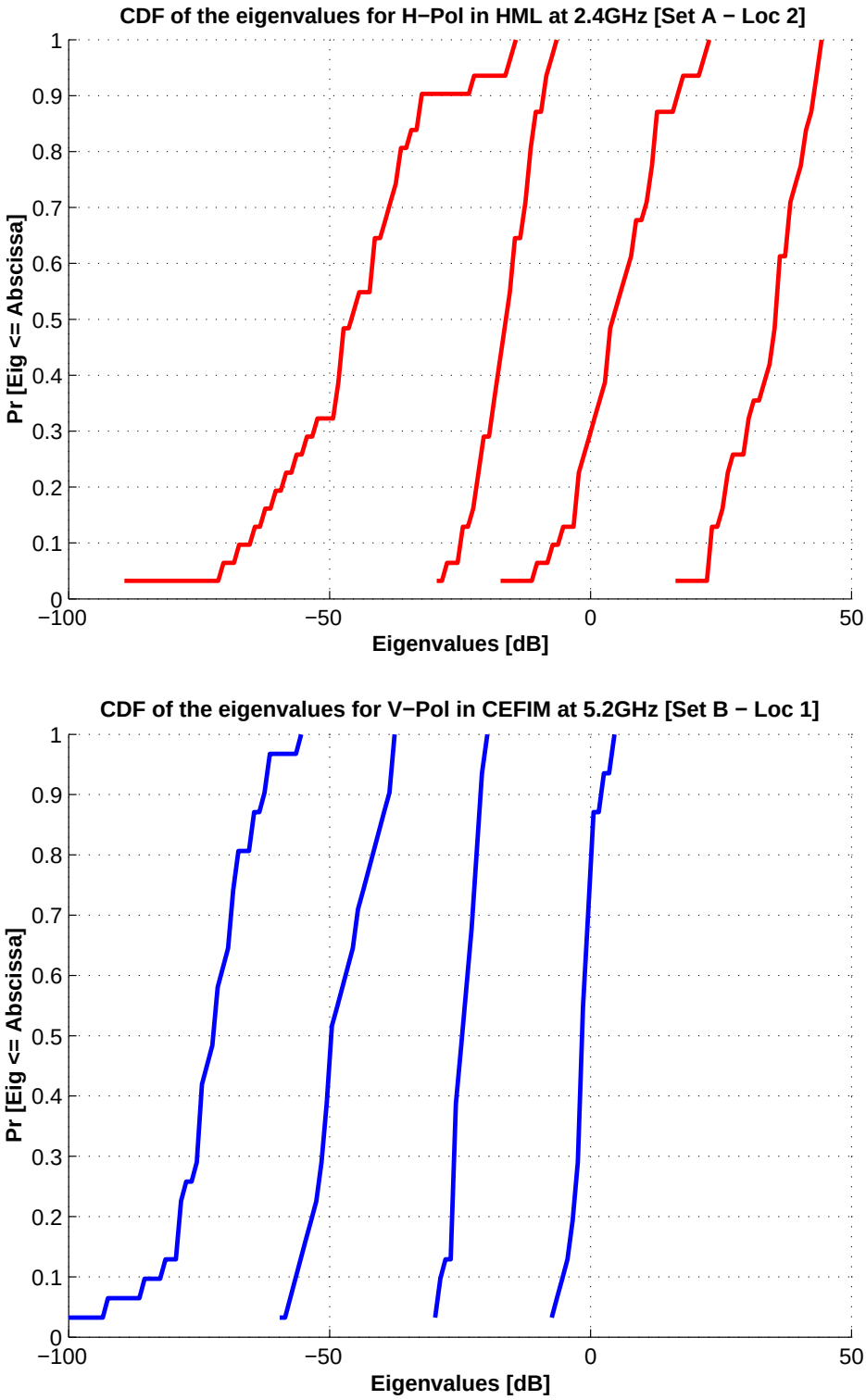

FIGURE 5.2: The channel rank of locations, in HML and CEFIM respectively, with low capacity.

Since the average capacity values are not sufficient indicators to suggest which polarization system is more suitable in either environment, the eigenvalue distributions were obtained, as depicted in Figures 5.3 - 5.4 for HML and Figures 5.5 - 5.6 for CEFIM, in order to further analyze the polarization systems and their effect on capacity. Only the first two eigenvalues are shown, since the other eigenvalues are quite weak and are considered not to significantly contribute to the capacity.

It is evident from the figures that the dual-pol system suffers from a power loss relative to the single polarizations in both HML and CEFIM. The power loss is also evident from the 10% (indicates 10% outage performance) and 50% (indicates on average which system performs better) CDF levels as shown in Tables 5.7 - 5.8. This power loss is to be expected, because most indoor environments exhibit depolarization ratios (defined here as the ratio of the average receiving power of same-pol to cross-pol) in the order of 3 to 10 dB.

Table 5.7: The 10% and 50% levels for the dominant eigenvalue for HML at 2.4 GHz and 5.2 GHz respectively.

		2.4GHz		5.2GHz	
		10% [dB]	50% [dB]	10% [dB]	50% [dB]
Dual-Pol	Set A	3	11	4	13
	Set B	4	12	7	18
V-Pol	Set A	1	15	4	17
	Set B	3	17	3	16
H-Pol	Set A	11	38	11	25
	Set B	12	22	15	26

Thus far the H-pol system still performs better on average and the dual-pol system appears to not offer an advantage over the single-pol systems. To take the eigenvalue investigation one step further, the robustness of the systems is also determined. In the present context, a robust MIMO system is one that can provide at least two parallel subchannels that have almost equal quality (equal gain), almost all of the time. To study this idea concretely, the ratio of the first two channel eigenvalues in dB is computed, which is referred to as the “eigenvalue spacing.”

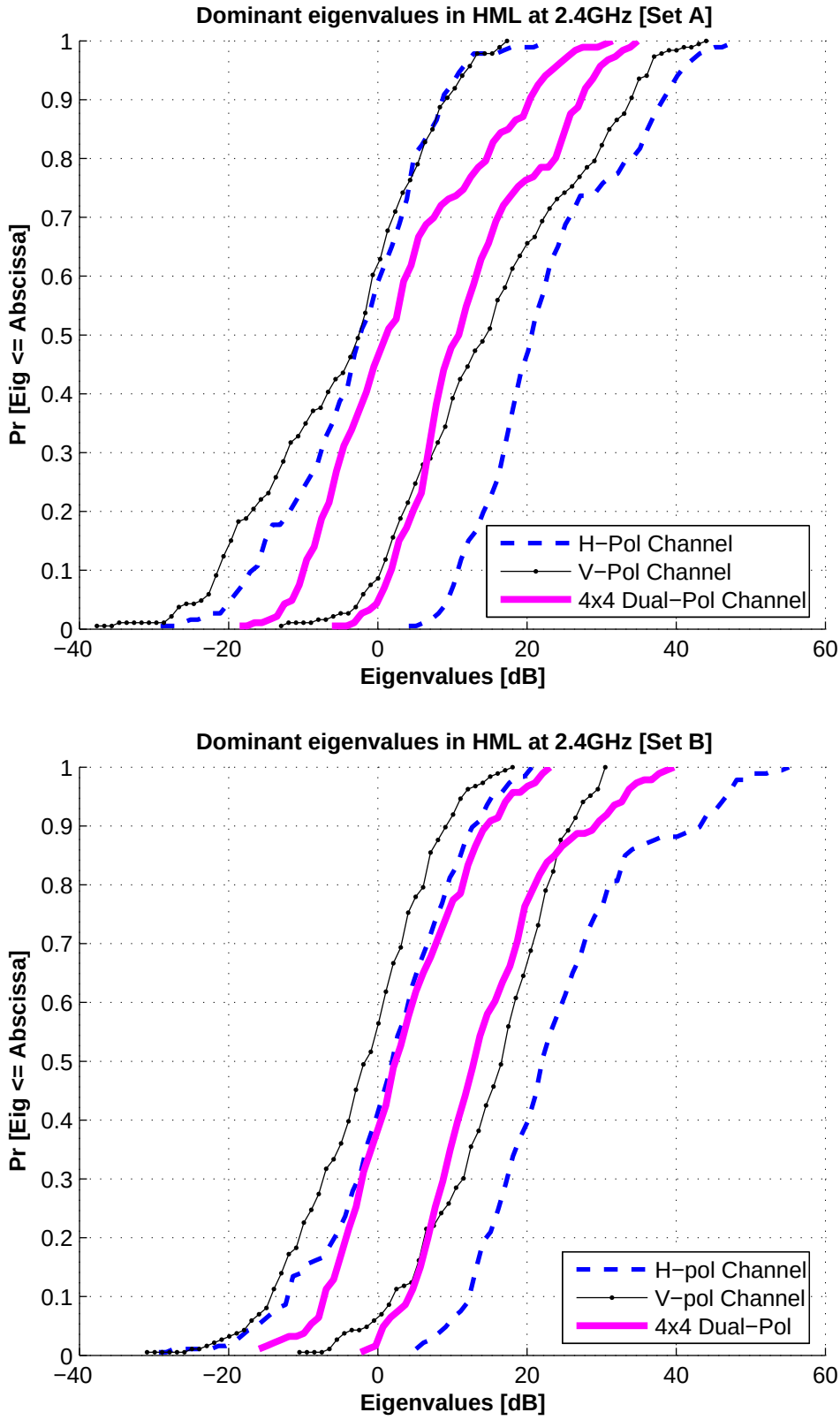

FIGURE 5.3: The performance of the V-Pol, H-Pol and Dual-Pol channels in HML at 2.4 GHz for Set A and Set B, respectively.

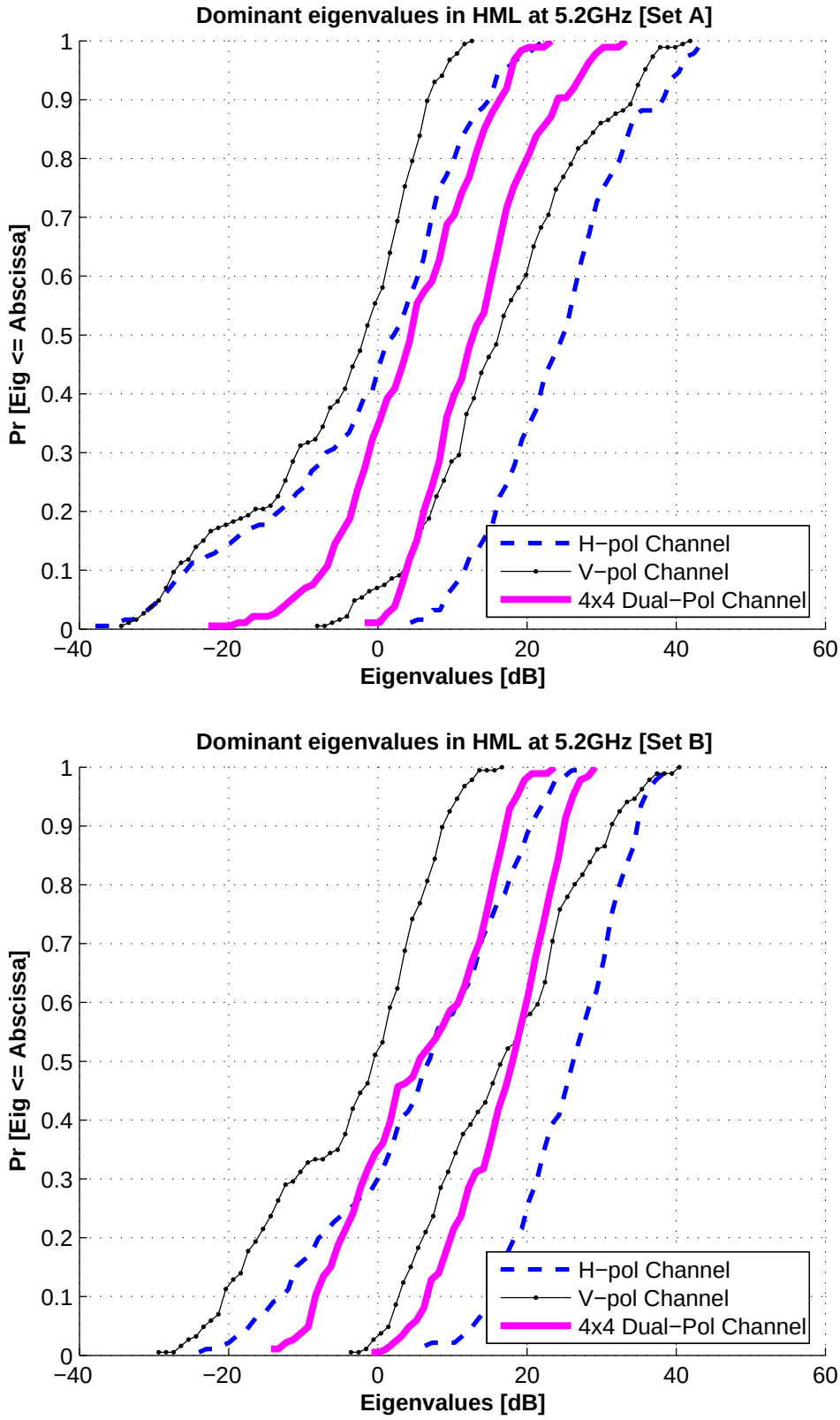

FIGURE 5.4: The performance of the V-Pol, H-Pol and Dual-Pol channels in HML at 5.2 GHz for Set A and Set B, respectively.

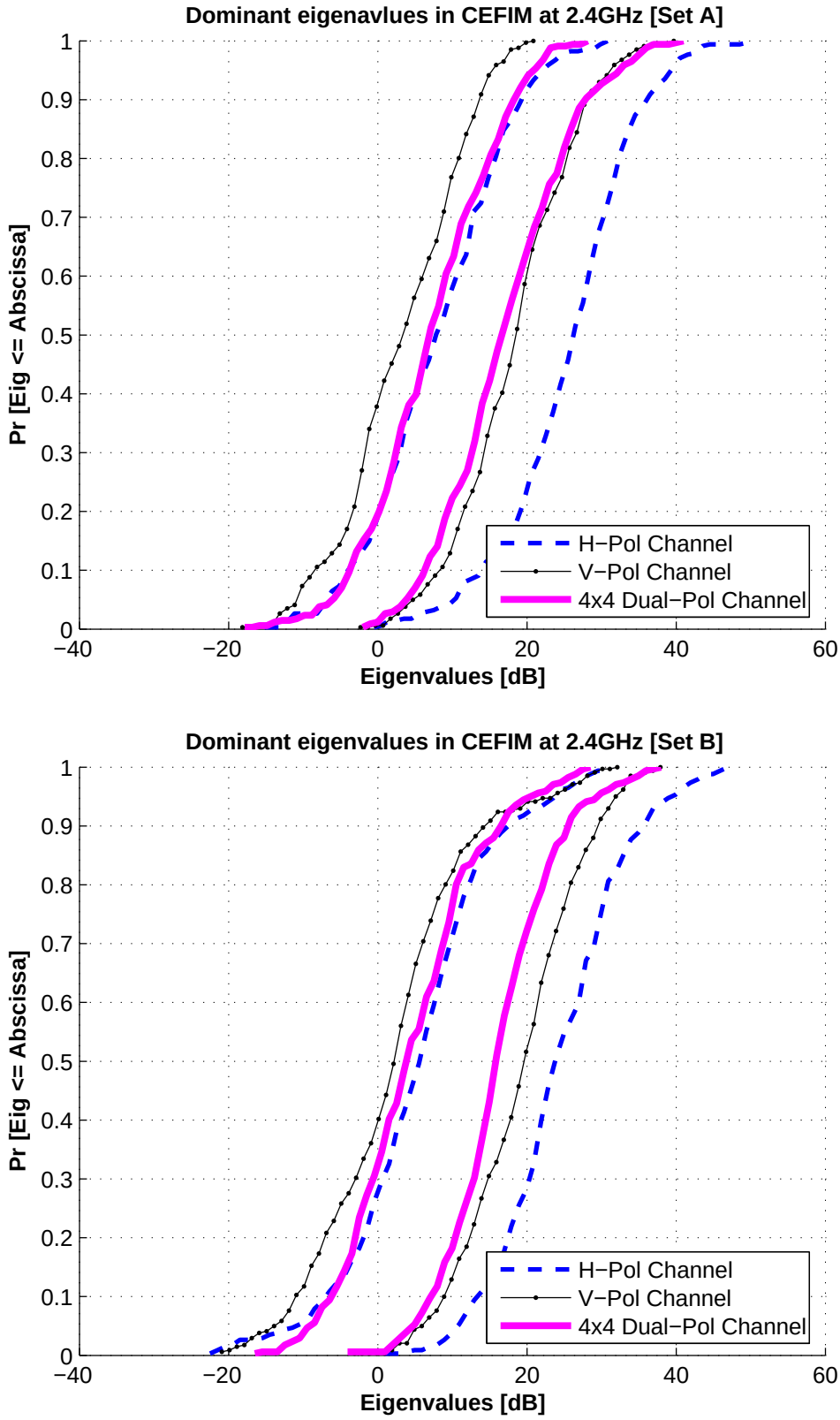

FIGURE 5.5: The performance of the V-Pol, H-Pol and Dual-Pol channels in CEFIM at 2.4 GHz for Set A and Set B, respectively.

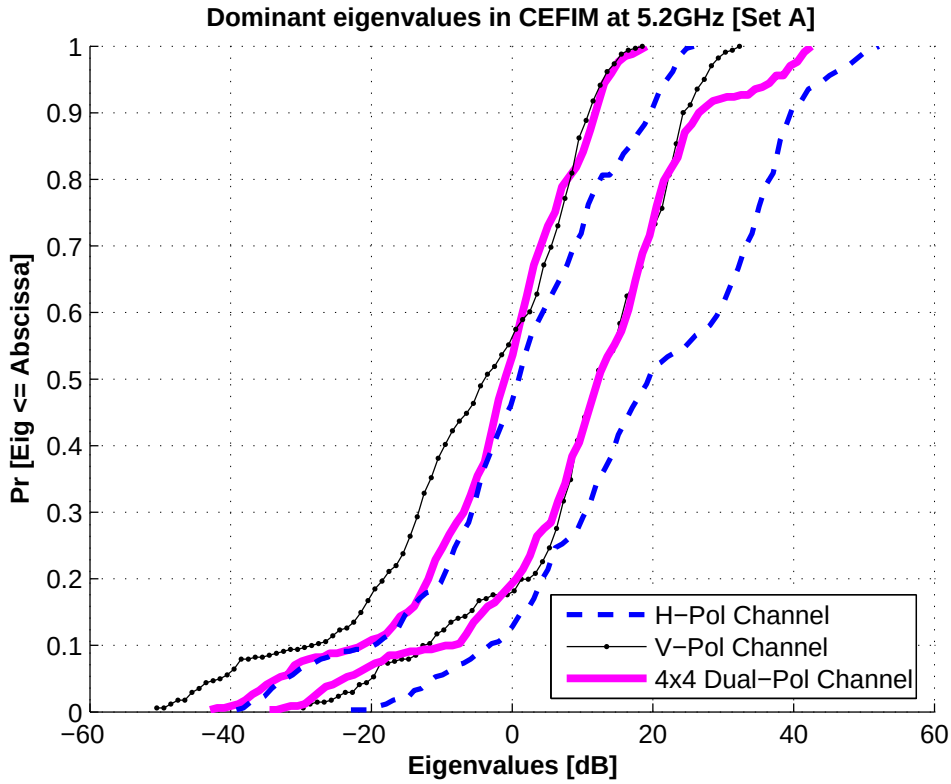

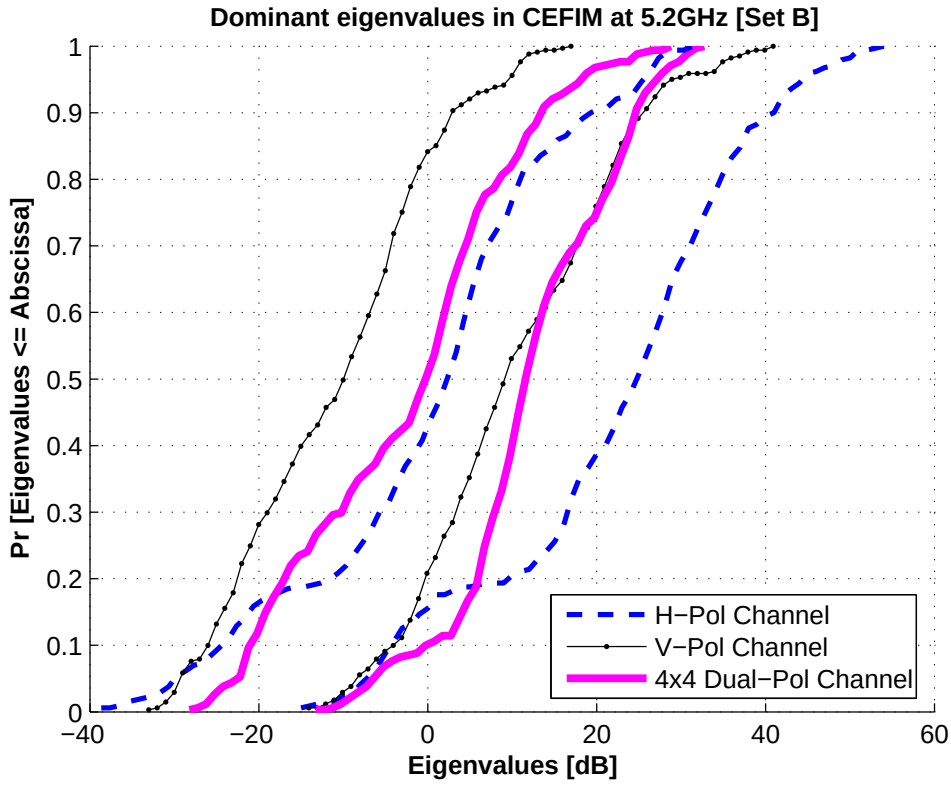

FIGURE 5.6: The performance of the V-Pol, H-Pol and Dual-Pol channels in CEFIM at 5.2 GHz for Set A and Set B, respectively.

Table 5.8: The 10% and 50% levels for the dominant eigenvalue for CEFIM at 2.4 GHz and 5.2 GHz respectively.

		2.4GHz		5.2GHz	
		10% [dB]	50% [dB]	10% [dB]	50% [dB]
Dual-Pol	Set A	6	17	-10	11
	Set B	8	16	0	11
V-Pol	Set A	9	19	-12	11
	Set B	9	20	-4	9
H-Pol	Set A	14	27	-2	20
	Set B	13	23	-4	25

Note that in the results that follow, lower eigenvalue spacing is found to be better, indicating more similar channel gains. CDFs of the eigenvalue spacing for the different antenna systems are plotted in Figures 5.7 - 5.10 for the two environments.

In each CDF, the 50% level roughly indicates which system has lower spacing on average, while the 90% level indicates which system has lower spacing most of the time, since only 10% of the cases would have higher (worse) eigenvalue spacing. The 50% and 90% levels are tabulated in Tables 5.9 and 5.10, showing that the dual-pol system offers a 10-20 dB improvement in eigenvalue spacing both on average and for low outage levels. This result suggests that dual polarization is more robust with respect to the operating environment, as long as the somewhat reduced average power gain can be tolerated.

The effect of the orientation of the transmitters and receivers is investigated to determine whether more scattering occurs in one orientation than in another. When looking at the effect of the Set A and Set B orientations on the capacities attained in both environments, it can be seen from Table 5.1 and Table 5.2 that Set B capacities appear to be slightly higher than the Set A capacities. However, as with the polarizations above, the difference is not significant enough to favor one orientation over another. The eigenvalue analysis as depicted in Figure 5.11 further confirms this.

The capacities of the orientations and polarizations in both HML and CEFIM appear to not be

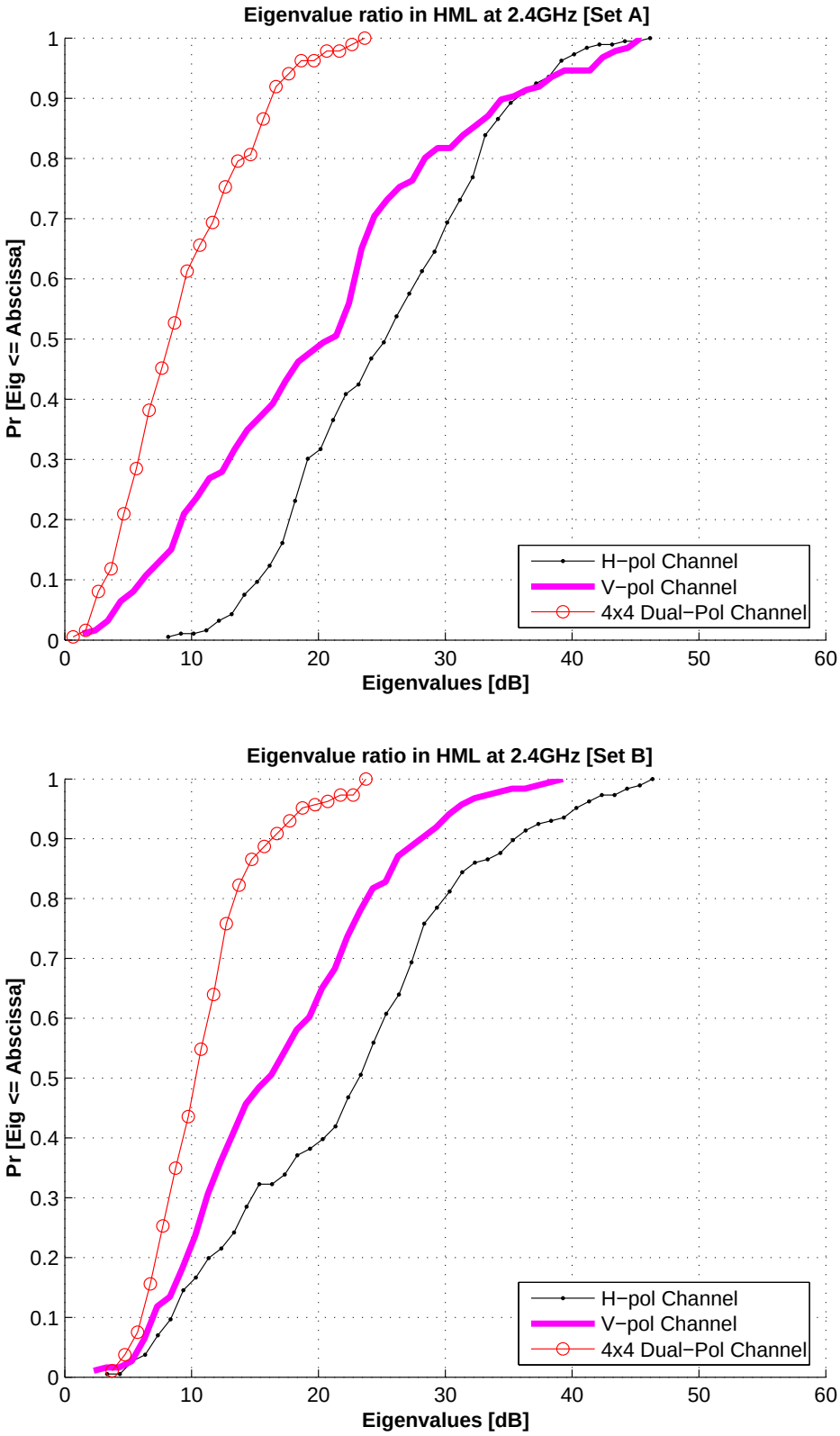

FIGURE 5.7: CDF of the spacings between the dominant eigenvalues for HML at 2.4 GHz for Set A and Set B respectively.

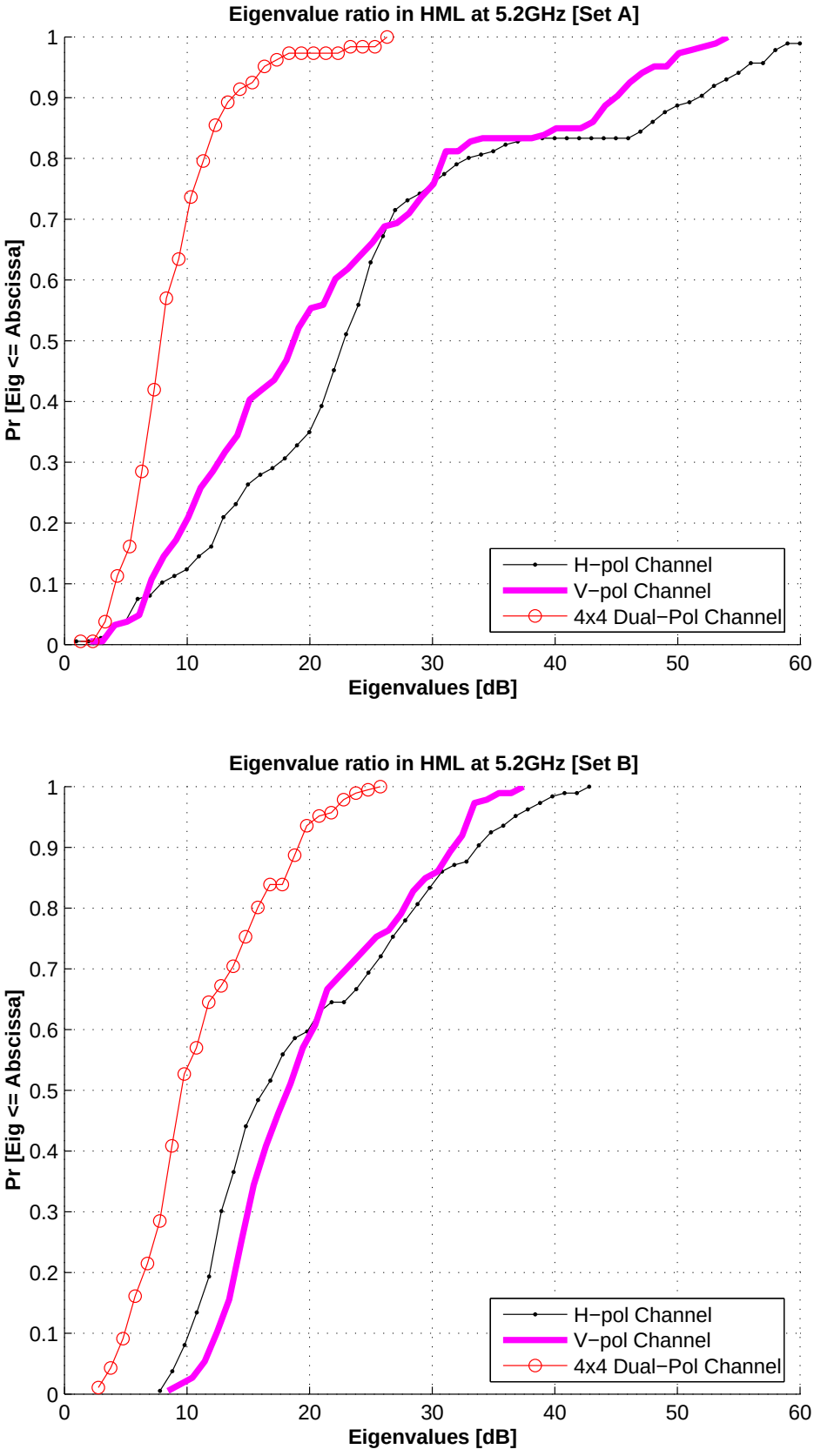

FIGURE 5.8: CDF of the spacings between the dominant eigenvalues for HML at 5.2 GHz for Set A and Set B respectively.

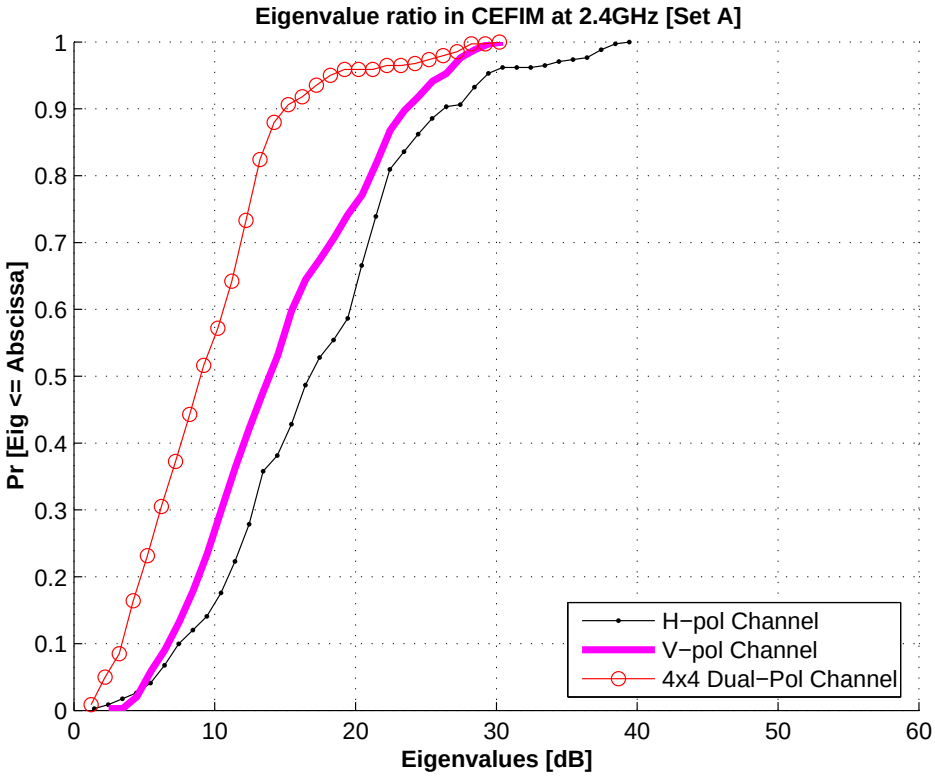

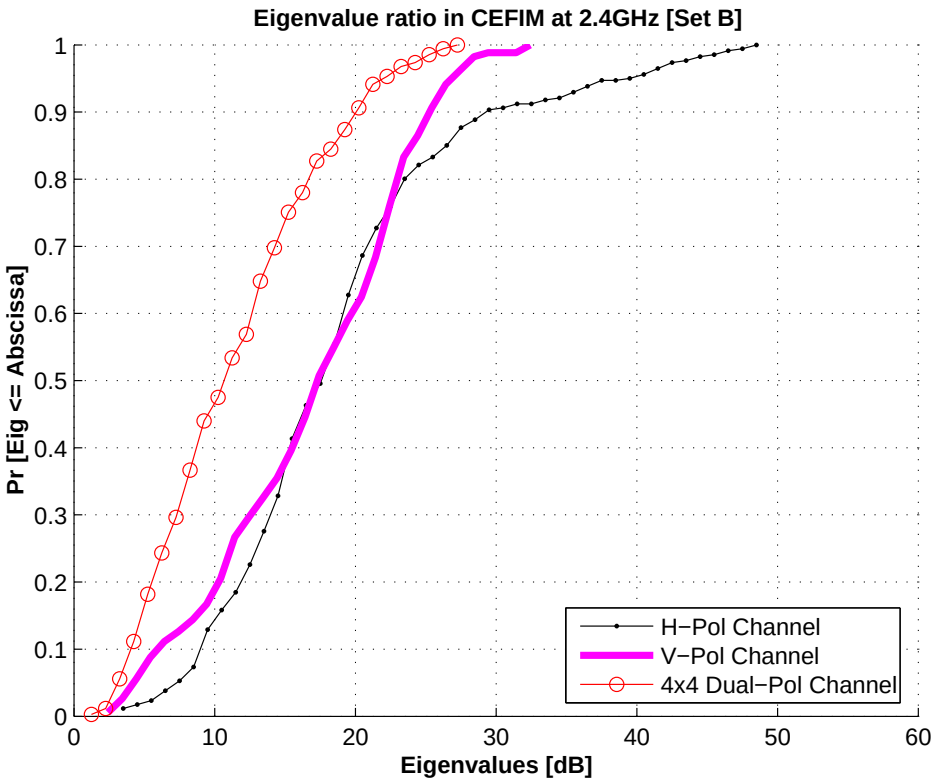

FIGURE 5.9: CDF of the spacings between the dominant eigenvalues for CEFIM at 2.4 GHz for Set A and Set B respectively.

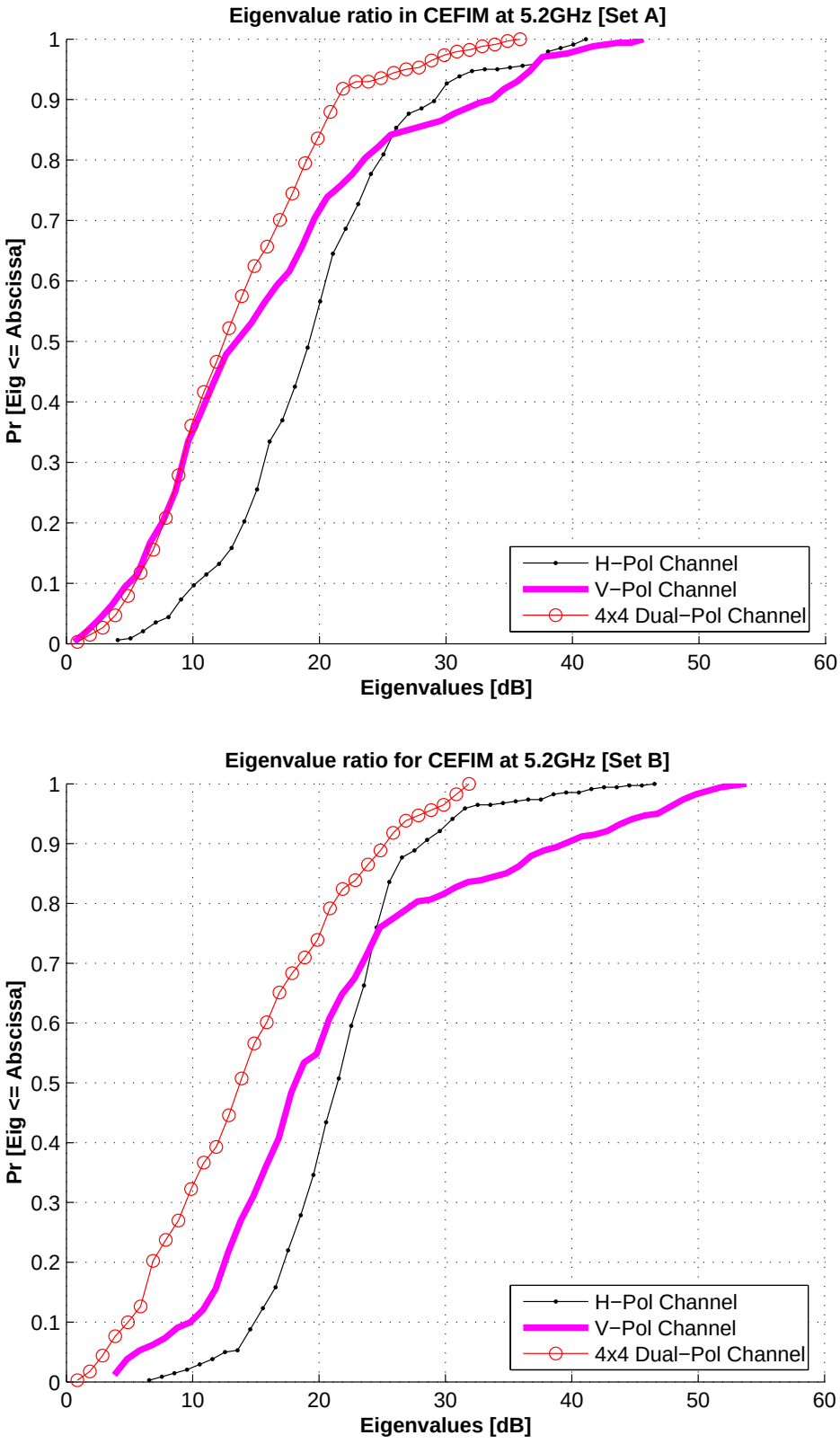

FIGURE 5.10: CDF of the spacings between the dominant eigenvalues for CEFIM at 5.2 GHz for Set A and Set B respectively.

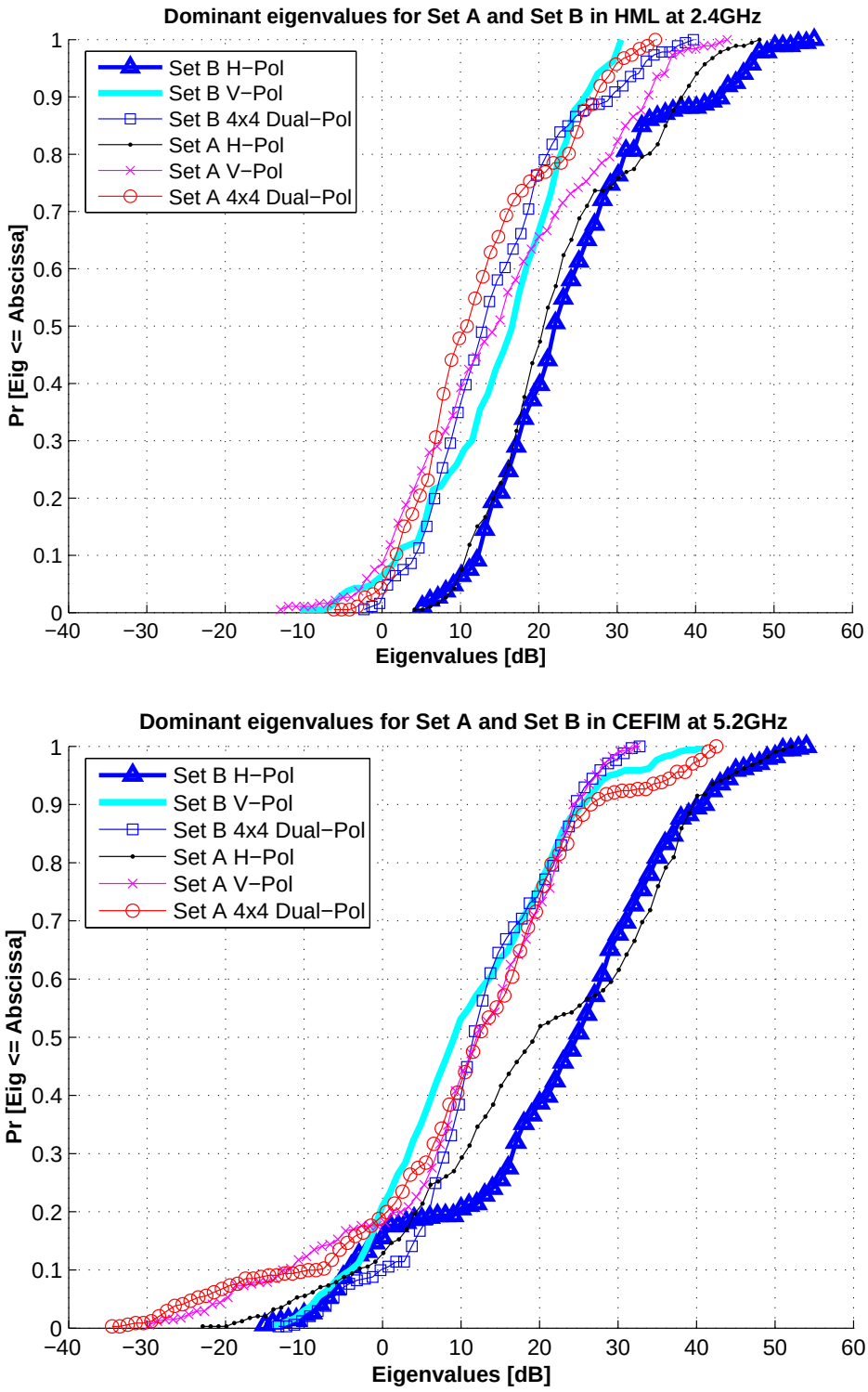

FIGURE 5.11: Comparison of Set A and Set B eigenvalues in HML and CEFIM respectively.

Table 5.9: The 50% and 90% levels of the spacing between the first two eigenvalues for HML at 2.4 GHz and 5.2 GHz respectively.

		2.4GHz		5.2GHz	
		50% [dB]	90% [dB]	50% [dB]	90% [dB]
Dual-Pol	Set A	8	16	9	13
	Set B	10	17	9	19
V-Pol	Set A	20	35	19	45
	Set B	16	28	18	32
H-Pol	Set A	25	36	22	51
	Set B	23	35	16	34

Table 5.10: The 50% and 90% levels of the spacing between the first two eigenvalues for CEFIM at 2.4 GHz and 5.2 GHz respectively.

		2.4GHz		5.2GHz	
		50% [dB]	90% [dB]	50% [dB]	90% [dB]
Dual-Pol	Set A	12	21	9	15
	Set B	14	25	11	20
V-Pol	Set A	14	34	14	24
	Set B	19	40	17	25
H-Pol	Set A	19	29	17	26
	Set B	21	25	17	29

significantly different. Considering also that channel ranks of up to 3 can be achieved in some of the locations, it could suggest that both environments are sufficiently richly scattered.

5.1.2 Center Frequency and Frequency Scaling

As already mentioned above, HML capacity performance at 5.2 GHz is better than at 2.4 GHz (Figure 5.12) and for CEFIM performance at 2.4 GHz is better than at 5.2 GHz (Figure 5.13).

Frequency scaling is investigated to determine whether the characteristics of the system at one frequency can be estimated at another frequency. In [65] frequency scaling of the spatial

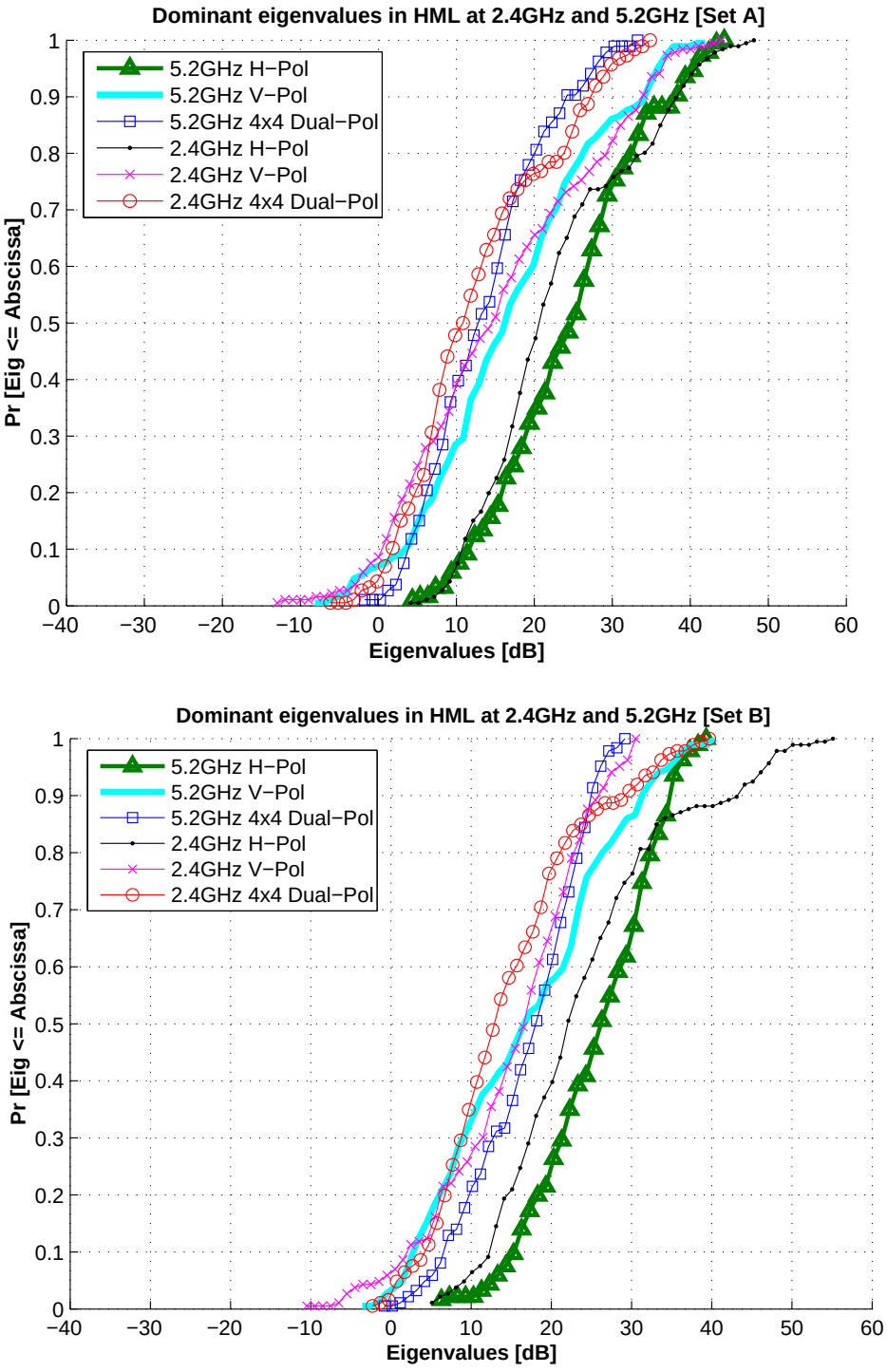

FIGURE 5.12: Comparison of the eigenvalues at 2.4 and 5.2 GHz in HML for Set A and Set B respectively.

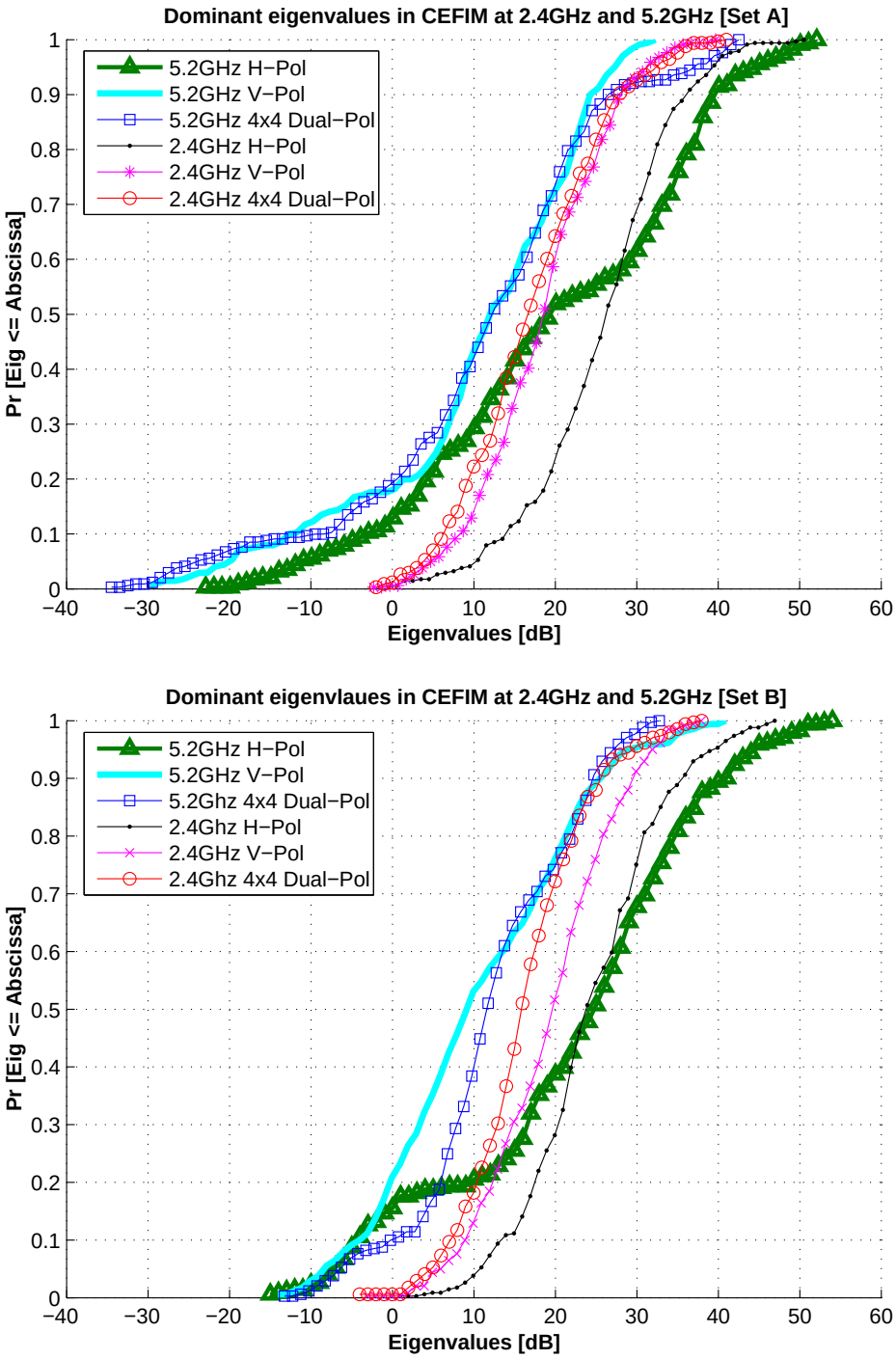

FIGURE 5.13: Comparison of the eigenvalues at 2.4 and 5.2 GHz in CEFIM for Set A and Set B respectively.

Table 5.11: Correlation of capacities at 2.4 GHz and 5.2 GHz and the standard deviation of a linear fit for HML with respect to antenna polarization and array orientation.

		Correlation ρ	Standard Dev. σ
Dual-Pol	Set A	0.91	1.74
	Set B	0.42	3.85
V-Pol	Set A	0.70	2.56
	Set B	0.53	4.50
H-Pol	Set A	0.93	1.69
	Set B	0.60	3.94

Table 5.12: Correlation of capacities at 2.4 GHz and 5.2 GHz and the standard deviation of a linear fit for CEFIM with respect to antenna polarization and array orientation.

		Correlation ρ	Standard Dev. σ
Dual-Pol	Set A	0.05	5.65
	Set B	0.56	4.63
V-Pol	Set A	0.16	4.91
	Set B	0.50	3.62
H-Pol	Set A	0.50	0.58
	Set B	0.54	5.90

correlation coefficients is discussed. An exponential correlation model was found to describe the measurements collected at both 2.4 GHz and 5.2 GHz, and a simple linear dependence was found to exist between the decorrelation at the two center frequencies. The study in this dissertation looks at the relationship between the capacities at the two center frequencies. From Table 5.11, only in the Set A orientation for HML does there appear to be a good correlation between the two frequencies. In CEFIM though, as shown in Table 5.12, neither orientations show a good correlation. Figure 5.14 depicts the correlations between the two frequencies in the two environments.

As already mentioned above, work done in [59] and [65] using 8-element linearly polarized monopole arrays in the CEFIM environment showed that frequency scaling could be achieved. However the low correlation between the two center frequencies in this study suggests that

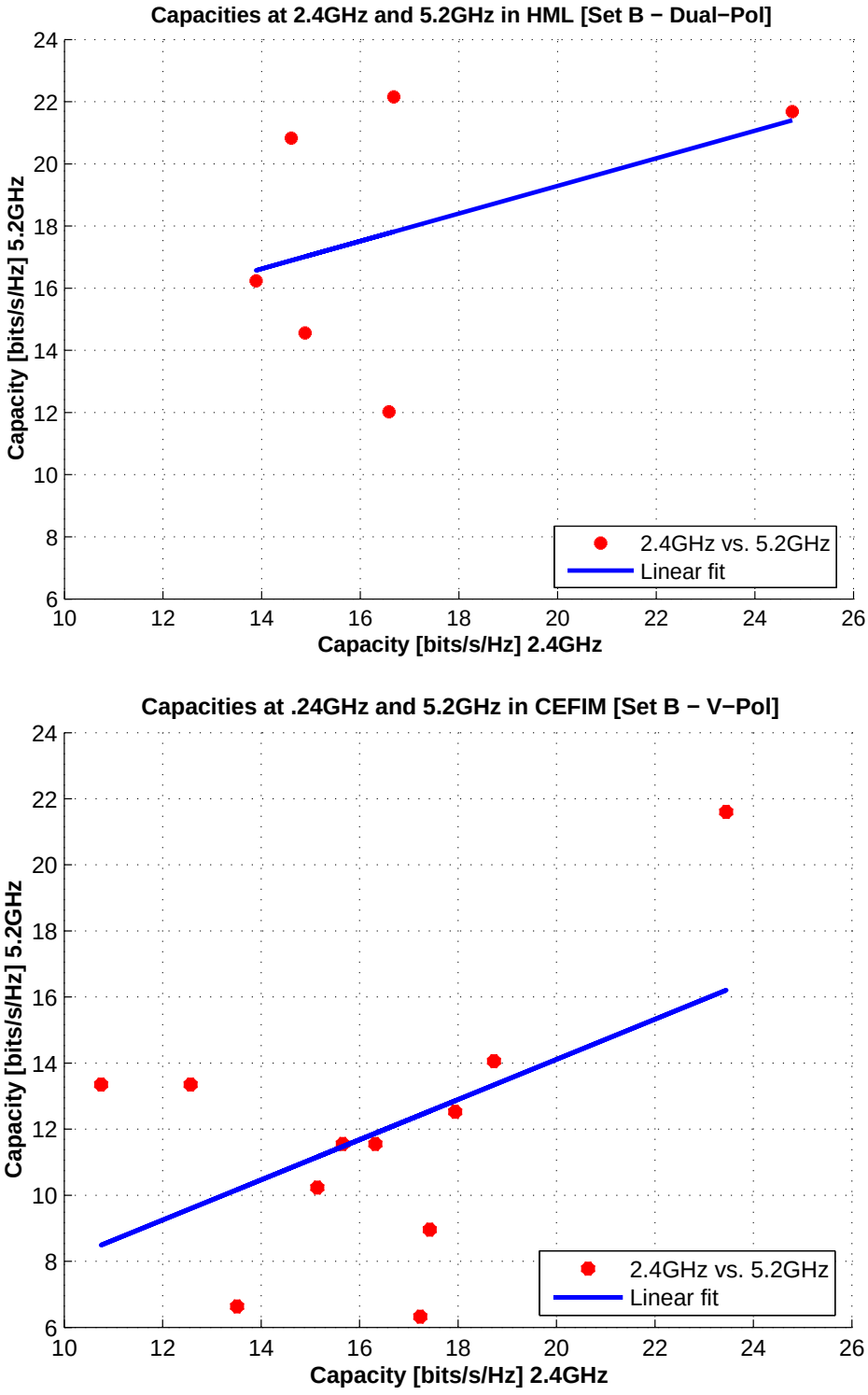

FIGURE 5.14: Correlations between the capacities at 2.4 GHz and 5.2GHz in HML and CEFIM respectively.

frequency scaling cannot be applied to either the HML or CEFIM environments using patch antennas. This could indicate that the type of antenna used plays a factor in achieving frequency scaling.

5.2 CHAPTER SUMMARY

This chapter covered the results of the measurement analysis carried out in the HML and CEFIM environment, based on the capacities attained, the effect of polarization, orientation, and center frequency.

In terms of the average capacities achieved, both CEFIM and HML yielded capacities that are between 40% and 75% of the maximum ideal. In locations where high capacity was attained, channel ranks of 3 exist, whereas for locations where low capacity is achieved, a channel rank of only 1 exists.

Studying the polarization systems, it was seen that the dual-polarization system does not offer a significant performance advantage over the single-pol systems. Analyzing the 10% and 50% CDF levels of the eigenvalue distributions, it was seen that the dual-pol system suffers from a power loss relative to the single-pol systems. However, when observing the 50% and 90% of the ratio of the dominant eigenvalues, it was seen that the dual-pol system is more robust than the single-pol systems.

The orientation of the receiver relative to the transmitter in HML, or the orientation of the transmitter relative to the receiver in CEFIM, did not have a significant effect on the capacities attained. This result, along with the effect of the polarization effect on capacity, and the high channel ranks achieved in certain locations, suggest that the environments are richly scattered.

The HML environment was found to be more reflective because performance at 5.2 GHz was slightly better than that at 2.4 GHz, while the CEFIM environment was found to be more absorptive because performance at 2.4 GHz was slightly better than that at 5.2 GHz. The low correlation between the two frequencies in both environments suggests that frequency scaling cannot be applied using patch antennas.

CHAPTER SIX

ANALYTICAL MIMO MODELS

The results from the comparison of the measured data with that of the i.i.d. Gaussian, Kronecker and Weichselberger models are presented in this chapter.

The Kronecker and Weichselberger models have been discussed in Chapter 2. However, they will be briefly described here again.

6.1 THE KRONECKER MODEL

The Kronecker model is based on the second-order moments of the MIMO channel, describing the covariance structure [51], and can be described as [42, 49]:

$$\mathbf{R}_{\mathrm{H}} = \mathbf{R}_{\mathrm{H}}^{\mathrm{Tx}} \otimes \mathbf{R}_{\mathrm{H}}^{\mathrm{Rx}} \tag{6.1}$$

where $\mathbf{R}_{\mathrm{H}}^{\mathrm{Tx}}$ and $\mathbf{R}_{\mathrm{H}}^{\mathrm{Rx}}$ are the respective covariance matrices at the transmitter and receiver side and $\mathbf{R}_{\mathrm{H}}$ is the channel covariance matrix. Any transmit signal results in one and the same receiving correlation.

The covariance matrices can be defined as shown below:

$$\mathbf{R}_{\mathrm{H}} = \frac{1}{N}\sum_{r=1}^{N}[\mathrm{vec}(\mathbf{H}(r))\mathrm{vec}(\mathbf{H}(\mathrm{r}))^{*}] \tag{6.2}$$

$$\mathbf{R}_{\mathrm{Rx}} = \frac{1}{N}\sum_{r=1}^{N}\mathbf{H}(r)\mathbf{H}^{*}(r) \tag{6.3}$$

$$\mathbf{R}_{\mathrm{Tx}} = \frac{1}{N}\sum_{r=1}^{N}\left(\mathbf{H}^{*}(r)\mathbf{H}(r)\right)^{\mathrm{T}} \tag{6.4}$$

where N is the number of channel realizations.

The channel can be modeled [42, 43, 50] as:

$$\mathbf{H}_{\mathrm{Kron}} = \frac{1}{\sqrt{\mathrm{tr}\{\mathbf{R}_{\mathrm{Rx}}\}}}\mathbf{R}_{\mathrm{Rx}}^{1/2}\mathbf{G}(\mathbf{R}_{\mathrm{Tx}}^{1/2})^{\mathrm{T}} \tag{6.5}$$

where $\mathbf{G}$ is the Gaussian i.i.d. matrix with zero-mean complex normal entries with unit variance.

6.1.1 Implementation of the Kronecker Model

As shown in Chapter 4, the channel data in this study is represented as $\tilde{\mathbf{H}}(1:31, 1:8, 1:8, 1, 10)$. For the modeling purpose the entire 8×8 channel matrix consisting of both co- and cross-polarized elements is used.

The first step of the implementation involves finding the full channel correlation matrix for each location and at the mth frequency bin. The 8×8 channel matrix is reshaped into a 1×64 matrix:

$$\tilde{\mathbf{H}}_{\mathrm{Loc}}^{(m)} = \mathrm{res}(\tilde{\mathbf{H}}^{(m)}, 1, 64) \tag{6.6}$$

The full channel correlation matrix is then calculated as follows:

$$\mathbf{R}_{\mathrm{f}}^{(m)} = \tilde{\mathbf{H}}_{\mathrm{Loc}}^{(m)}(\tilde{\mathbf{H}}_{\mathrm{Loc}}^{(m)})^{\mathrm{H}} \tag{6.7}$$

where $\mathbf{R}_{f}^{(m)}$ represents the 64×64 correlation matrix for the mth frequency bin.

Unlike in Equation 6.3 and Equation 6.4, the 8×8 receiver and transmitter covariance matrices are found through the decomposition of the full correlation matrix:

$$\mathbf{R}_{\mathrm{Tx\_Loc}}^{(j,k)} = \sum_{i=1}^{N_t}\mathbf{R}_{\mathrm{f}}^{(m)}(i + N_t(j-1), i + N_t(k-1)) \tag{6.8}$$

$$\mathbf{R}_{\mathrm{Rx\_Loc}}^{(j,k)} = \sum_{i=1}^{N_r}\mathbf{R}_{\mathrm{f}}^{(m)}(j + N_r(j-1), k + N_r(k-1)) \tag{6.9}$$

where $1 \leq j \leq 8$ and $1 \leq j \leq 8$.

The Kronecker channel matrix for each location and at each mth frequency bin is calculated, with reference to Equation 6.5, as:

$$\tilde{\mathbf{H}}^{(m)}_{\text{Kron\_Loc}} = \frac{1}{\sqrt{\text{tr}\{\mathbf{R}^{(m)}_{\text{Rx\_Loc}}\}}}(\mathbf{R}^{(m)}_{\text{Rx\_Loc}})^{1/2}\mathbf{G}((\mathbf{R}^{(m)}_{\text{Tx\_Loc}})^{1/2})^{\text{T}} \tag{6.10}$$

Once the Kronecker channel matrix has been determined the capacity of the channel can be found as follows:

$$C^{(m)}_{\text{Kron\_Loc}} = \log_2 \det\left[\mathbf{I} + \frac{\rho}{N_t}\tilde{\mathbf{H}}^{(m)}_{\text{Kron\_Loc}}(\tilde{\mathbf{H}}^{(m)}_{\text{Kron\_Loc}})^{\text{H}}\right] \tag{6.11}$$

Plots of the cdfs of the capacities of the models are used to see how well they fit the measured data. To obtain the cdf, the capacities are first reshaped into a $1\times(N_l N_f)$ matrix :

$$C_{\text{Environment}} = \text{res}(C^{(m)}_{\text{Kron\_Loc}}, 1, N_l N_f) \tag{6.12}$$

The bulk average capacity is used to compare the performances of the different models. First the average capacity for each location is determined :

$$\overline{C}_{\text{Kron\_Loc}} = \frac{\sum_{m=1}^{N_f} C^{(m)}_{\text{Kron\_Loc}}}{N_f} \tag{6.13}$$

The bulk average capacity is then calculated as follows:

$$\overline{C}_{\text{Kron\_Environment}} = \frac{\sum_{n=1}^{N_l} \overline{C}^{(n)}_{\text{Kron\_Loc}}}{N_l} \tag{6.14}$$

6.2 THE WEICHSELBERGER MODEL

The Weichselberger channel model [7] can be written as

$$\mathbf{H}_{\text{Weichsel}} = \mathbf{U}_{\text{A}}\left(\tilde{\mathbf{\Omega}} \odot \mathbf{G}\right)\mathbf{U}^{\text{T}}_{\text{B}} \tag{6.15}$$

where $\mathbf{G}$ is a random matrix with i.i.d. zero-mean complex normal entries with unit variance, $\mathbf{U}_{\text{A}}$ and $\mathbf{U}_{\text{B}}$ are the spatial eigenbases of side A and side B respectively, $\tilde{\mathbf{\Omega}}$ is the element-wise square root of the coupling matrix $\mathbf{\Omega}$ given by

$$[\mathbf{\Omega}]_{\mathrm{m,n}} = \mathrm{E}_{\mathbf{H}} \left\{ \left| \mathbf{u}_{\mathrm{A,m}}^{\mathrm{H}} \mathbf{H} \mathbf{u}_{\mathrm{B,n}}^{*} \right|^2 \right\} \tag{6.16}$$

where $\mathbf{u}_{\mathrm{A,m}}$ is the mth eigenvector of side A and $\mathbf{u}_{\mathrm{B,n}}$ is the nth eigenvector of side B.

The spatial eigenbases can be obtained as follows:

$$\mathbf{R}_{\mathrm{Rx}} = \mathbf{U}_{\mathrm{Rx}} \mathbf{\Lambda}_{\mathrm{Rx}} \mathbf{U}_{\mathrm{Rx}}^{\mathrm{H}} \tag{6.17}$$

$$\mathbf{R}_{\mathrm{Tx}} = \mathbf{U}_{\mathrm{Tx}} \mathbf{\Lambda}_{\mathrm{Tx}} \mathbf{U}_{\mathrm{Tx}}^{\mathrm{H}} \tag{6.18}$$

and the estimated power coupling matrix is obtained by

$$\mathbf{\Omega}_{\mathrm{Weichsel}} = \frac{1}{N} \sum_{r=1}^{N} \left(\mathbf{U}_{\mathrm{Rx}}^{\mathrm{H}} \mathbf{H}(r) \mathbf{U}_{\mathrm{Tx}}^{*} \right) \odot \left(\mathbf{U}_{\mathrm{Rx}}^{\mathrm{T}} \mathbf{H}(r) \mathbf{U}_{\mathrm{Tx}} \right) \tag{6.19}$$

where N is the number of channel realizations.

6.2.1 Implementation of the Weichselberger Model

The 8×8 co-and cross-polarized channel matrix is also used in the Weichselberger model. The transmitter and receiver covariance matrices computed in the section above are also used for computations in this section.

First the spatial eigenbases of the transmitter and receiver, for each location and at each frequency bin, are obtained from the eigenvalue decomposition of the transmitter and receiver covariance matrices:

$$\mathbf{U}_{\mathrm{Rx\_Loc}}^{(m)} = \mathrm{eig}(\mathbf{R}_{\mathrm{Rx\_Loc}}^{(m)}) \tag{6.20}$$

$$\mathbf{U}_{\mathrm{Tx\_Loc}}^{(m)} = \mathrm{eig}(\mathbf{R}_{\mathrm{Tx\_Loc}}^{(m)}) \tag{6.21}$$

where $\mathrm{eig}(.)$ performs the eigenvalue decomposition.

The coupling matrix is then calculated as follows:

$$\mathbf{\Omega}_{\text{Weichsel\_Loc}^{(m)}} = \left((\mathbf{U}^{(m)}_{\text{Rx\_Loc}})^{\text{H}}\tilde{\mathbf{H}}^{(m)}(\mathbf{U}^{(m)}_{\text{Tx\_Loc}})^{*}\right) \odot \left((\mathbf{U}^{(m)}_{\text{Rx\_Loc}})^{\text{T}}\tilde{\mathbf{H}}^{(m)}(\mathbf{U}^{(m)}_{\text{Tx\_Loc}})\right) \tag{6.22}$$

The element-wise square root of the coupling matrix is given by:

$$\tilde{\mathbf{\Omega}}^{(m)}_{\text{Weichsel\_Loc}} = \sqrt{\mathbf{\Omega}^{(m)}_{\text{Weichsel\_Loc}}} \tag{6.23}$$

The Weichselberger channel matrix is then calculated as follows:

$$\tilde{\mathbf{H}}_{\text{Weichsel\_Loc}^{(m)}} = \mathbf{U}^{(m)}_{\text{Rx\_Loc}}\left(\tilde{\mathbf{\Omega}}^{(m)}_{\text{Weichsel\_Loc}} \odot \mathbf{G}\right)(\mathbf{U}^{(m)}_{\text{Tx\_Loc}})^{\text{T}} \tag{6.24}$$

From the channel matrix above the capacity for the Weichselberger model can be calculated:

$$C^{(m)}_{\text{Weichsel\_Loc}} = \log_2 \det\left[\mathbf{I} + \frac{\rho}{N_t}\tilde{\mathbf{H}}^{(m)}_{\text{Weichsel\_Loc}}(\tilde{\mathbf{H}}^{(m)}_{\text{Weichsel\_Loc}})^{\text{H}}\right] \tag{6.25}$$

The cdf of the bulk capacities and the bulk average capacities are calculated as in Equations 6.12 - 6.14 the section above.

6.3 AVERAGE CAPACITIES OF THE KRONECKER AND WEICHSELBERGER MODELS

Unlike with the polarization and robustness evaluations discussed in the previous chapter, the individual polarization systems were not used. Instead the entire measured 8×8 dual-pol channel matrix was utilized. The Kronecker and Weichselberger models were compared with CDFs of the average capacities of the measured data and with an 8×8 i.i.d. Gaussian model. As can be seen from Figures 6.1 - 6.4, the Weichselberger model performs better than the Kronecker model. However, both underestimate the measured data, and the Gaussian model outperforms the models as well as the measured data.

The average capacities attained for the measured data and the models for HML are shown in Table 6.1, and for CEFIM it is shown in Table 6.2. The capacity for an ideal 8×8 MIMO system is 53.3 b/s/Hz and the average capacity of the measured data was found to be between 45% and 60% of this value. The capacities for the Weichselberger model are on average 5 b/s/Hz lower than the measured average capacities, while the capacities for the Kronecker model are

Table 6.1: Average capacities in HML for the different models with respect to antenna polarization and orientation, and carrier frequency.

		2.4GHz [b/s/Hz]	5.2GHz [b/s/Hz]
Measured data	Set A	25.5	26.6
	Set B	28.0	29.8
Kronecker Model	Set A	16.0	17.6
	Set B	18.2	18.6
Weichselberger Model	Set A	20.7	21.7
	Set B	23.0	24.6

Table 6.2: Average capacities in CEFIM for the different models with respect to antenna polarization and orientation, and carrier frequency.

		2.4GHz [b/s/Hz]	5.2GHz [b/s/Hz]
Measured data	Set A	31.3	24.7
	Set B	29.9	23.8
Kronecker Model	Set A	20.5	16.6
	Set B	19.3	15.4
Weichselberger Model	Set A	26.0	20.0
	Set B	24.7	19.1

Table 6.3: Root Mean Square Errors of the models with respect to the measured data in HML.

		2.4GHz [b/s/Hz]	5.2GHz [b/s/Hz]
Kronecker Model	Set A	6.63	6.64
	Set B	5.74	6.03
Weichselberger Model	Set A	2.84	3.92
	Set B	3.49	4.60

on average 9 b/s/Hz lower. The results hold for both the CEFIM and HML environments.

The comparisons of the capacities for the measured data and models are shown in Figures 6.5 - 6.8. Once again the results show that the Weichselberger model performs better than the

Table 6.4: Root Mean Square Errors of the models with respect to the measured data in CEFIM.

		2.4GHz [b/s/Hz]	5.2GHz [b/s/Hz]
Kronecker Model	Set A	7.07	7.02
	Set B	7.24	6.81
Weichselberger Model	Set A	4.31	4.76
	Set B	4.10	4.35

Kronecker model, and the Weichselberger model fits the measured data better.

To further measure how well the models fit the measured data, the Root Mean Square Error (RMSE) is calculated. The RMSE is a measure of the differences between values predicted by a model and the actual values under observation and is measured in the same units as the the data. The RMSE is calculated as follows:

$$\mathrm{RMSE} = \sqrt{\frac{1}{N_l}\sum_{n=1}^{N_l}\left(\bar{C}_{\mathrm{Loc}}^{(n)} - \bar{C}_{\mathrm{Model\_Loc}}^{(n)}\right)^2} \tag{6.26}$$

where $\bar{C}_{\mathrm{x}}$ refers to the average capacity at each location for the measured or modeled data.

The RMSE of the Kronecker and Weichselberger models with respect to the measured data capacities in HML and CEFIM are given in Table 6.3 and Table 6.4, respectfully. The lower the error, the better the fit.

In [7] and as shown by Figure 3.10, the Weichselberger model fits the measured data almost exactly. The results here show that although the Weichselberger model performs better than the Kronecker model, it does not fit the measured data exactly. This could partly be attributed to parts of the channel not fading enough, so much so that the zero-mean Gaussian assumption is not valid. The performance of the Kronecker model is as expected for large antenna array sizes [51].

6.4 CHAPTER SUMMARY

This chapter looked at the capacities of the Kronecker and Weichselberger models and their relation to the measured data.

For the evaluation of the models, the entire 8×8 dual-pol measured channel matrix was utilized. The Weichselberger model performed better than the Kronecker model, although it still fits the measured data poorly. Kronecker models have been known to perform poorly for large antenna sizes. The performance of the Weichselberger model could be attributed to certain parts of the channel not fading enough and thus the zero-mean Gaussian assumption does not hold.

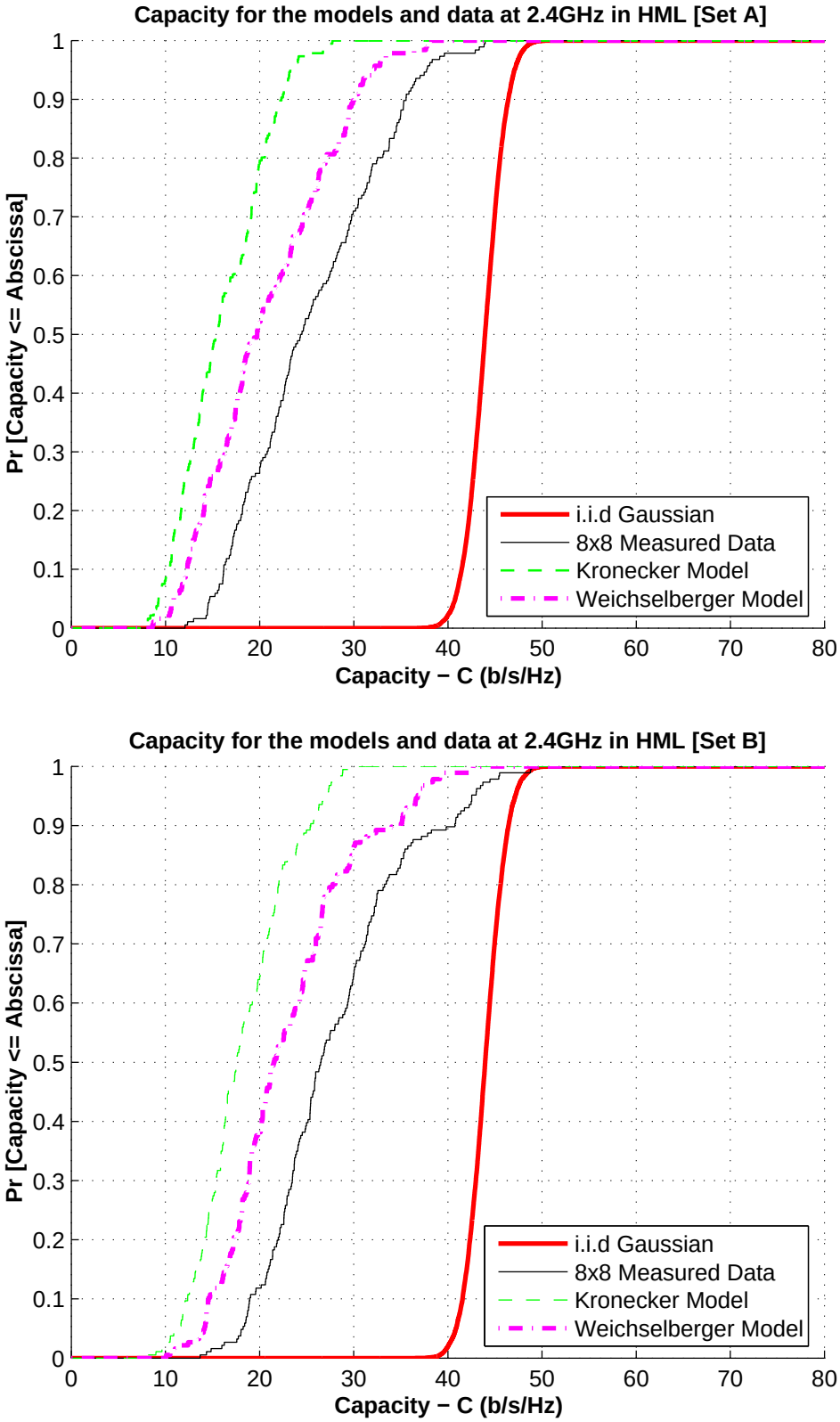

FIGURE 6.1: The CDF of the capacities for the models in HML at 2.4 GHz for Set A and Set B respectfully.

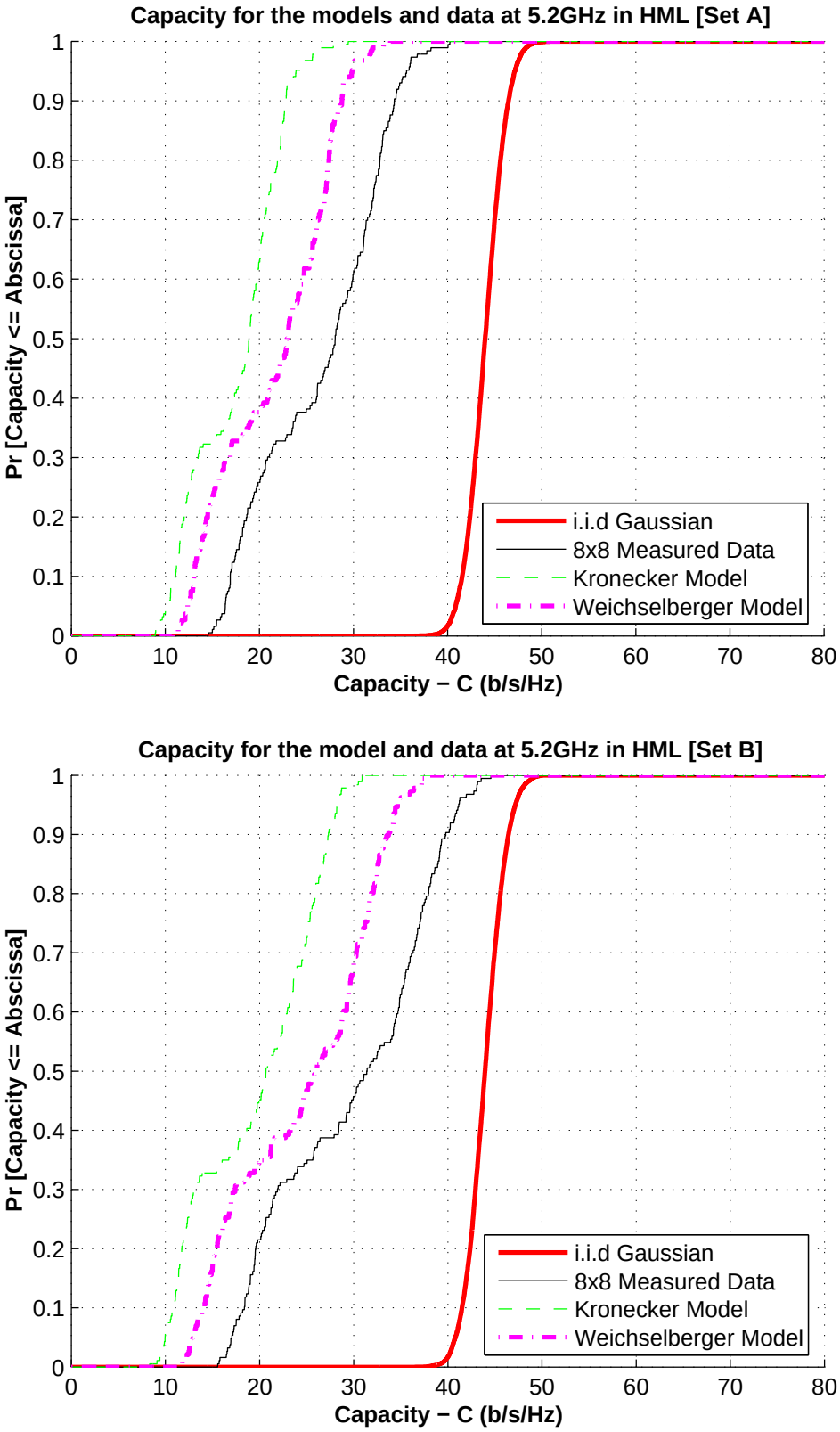

FIGURE 6.2: The CDF of the capacities for the models in HML at 5.2 GHz for Set A and Set B respectively.

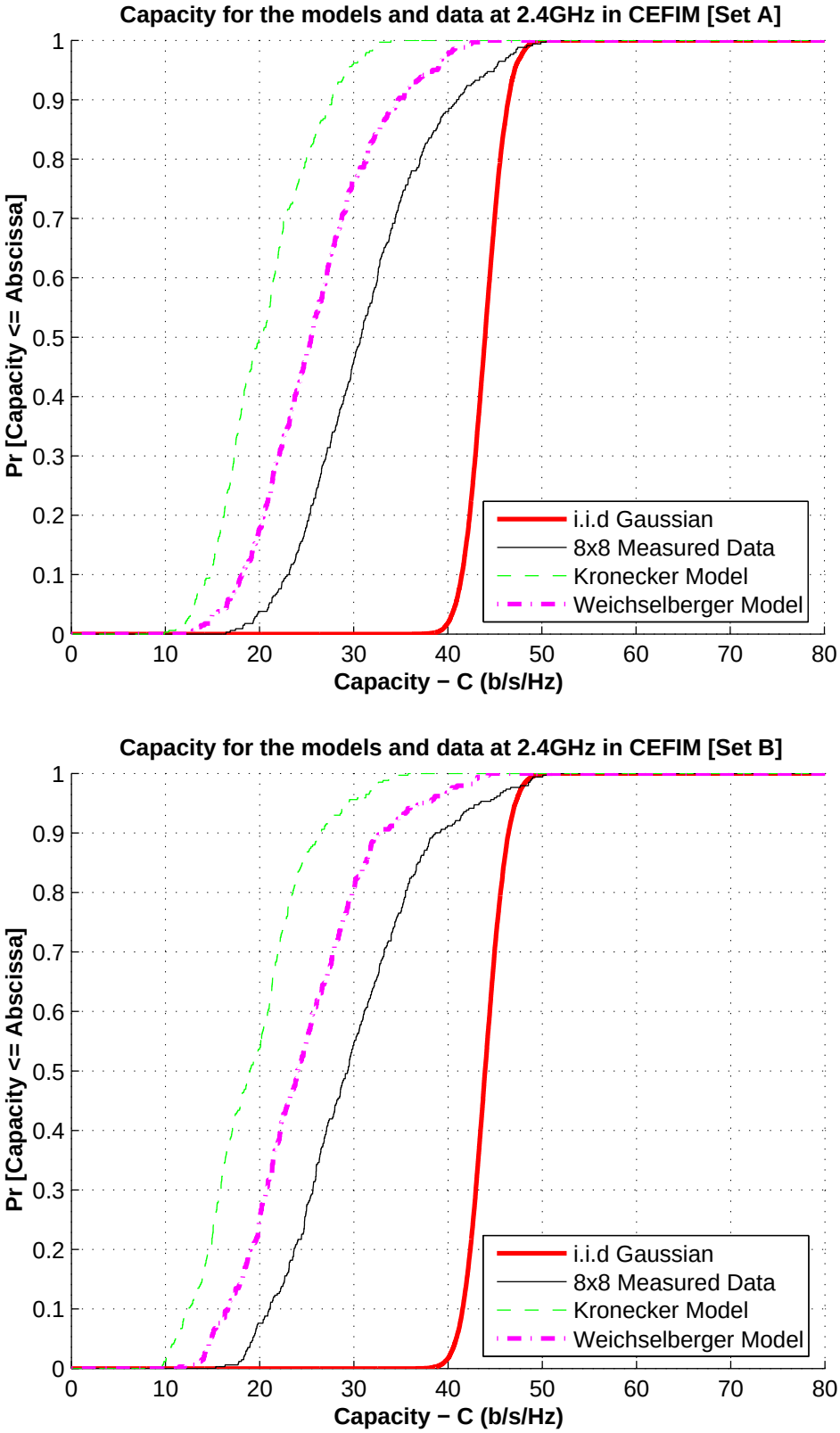

FIGURE 6.3: The CDF of the capacities for the models in CEFIM at 2.4 GHz for Set A and Set B respectively.

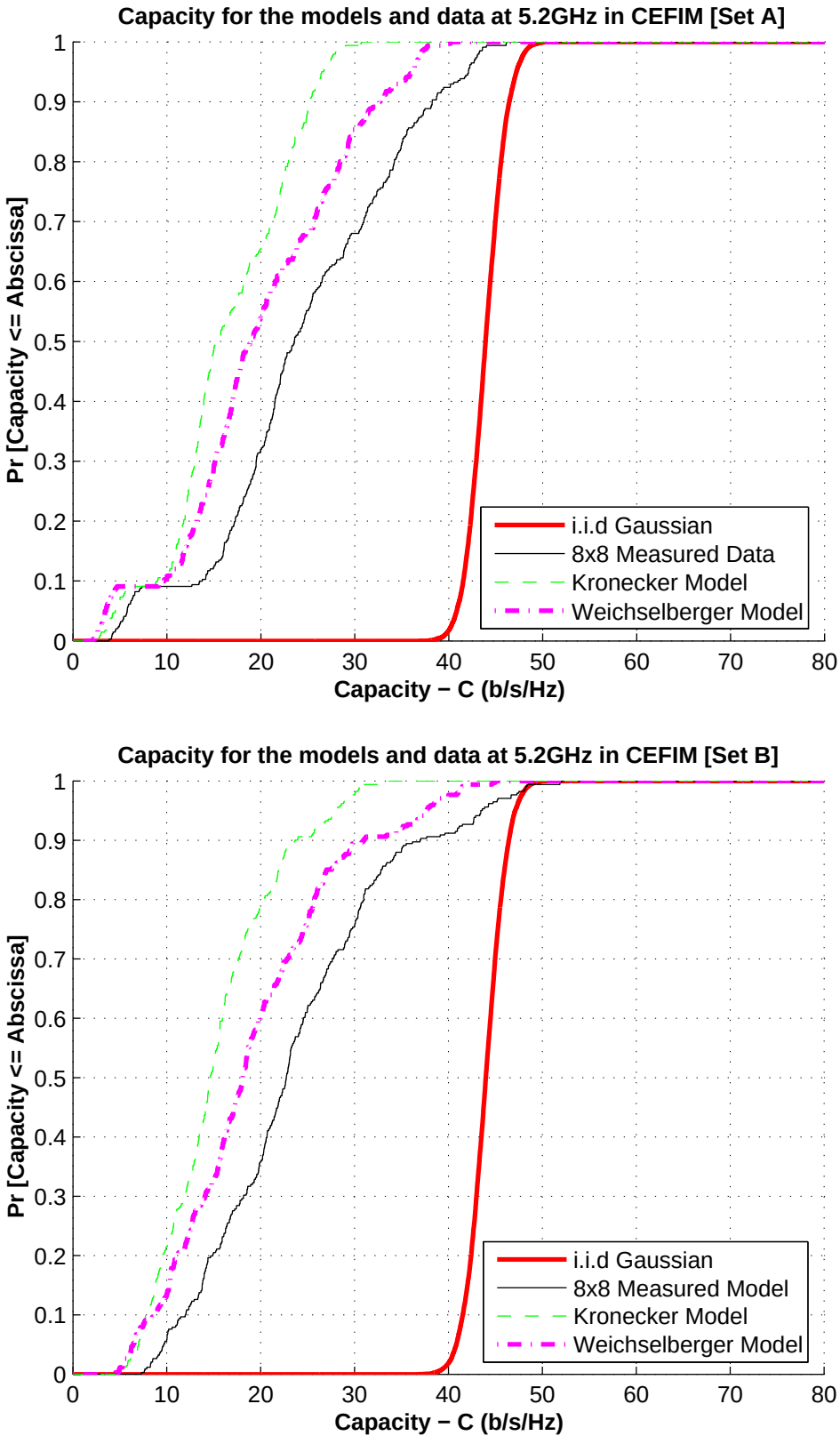

FIGURE 6.4: The CDF of the capacities for the models in CEFIM at 5.2 GHz for Set A and Set B respectively.

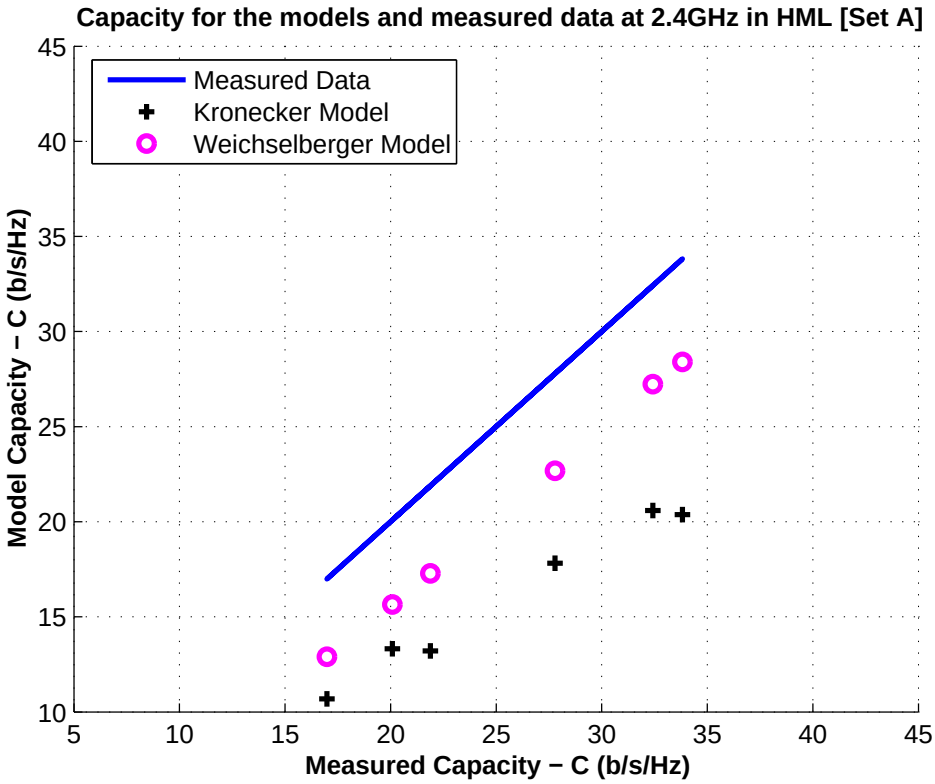

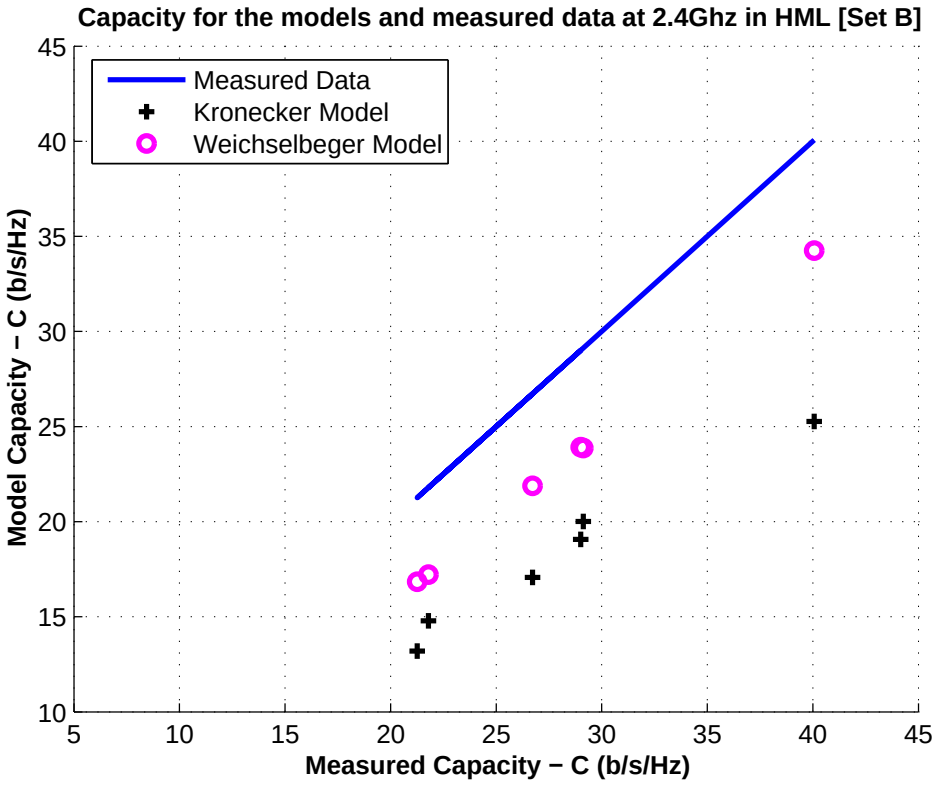

FIGURE 6.5: Average capacities for the models in HML at 2.4 GHz for Set A and Set B respectively.

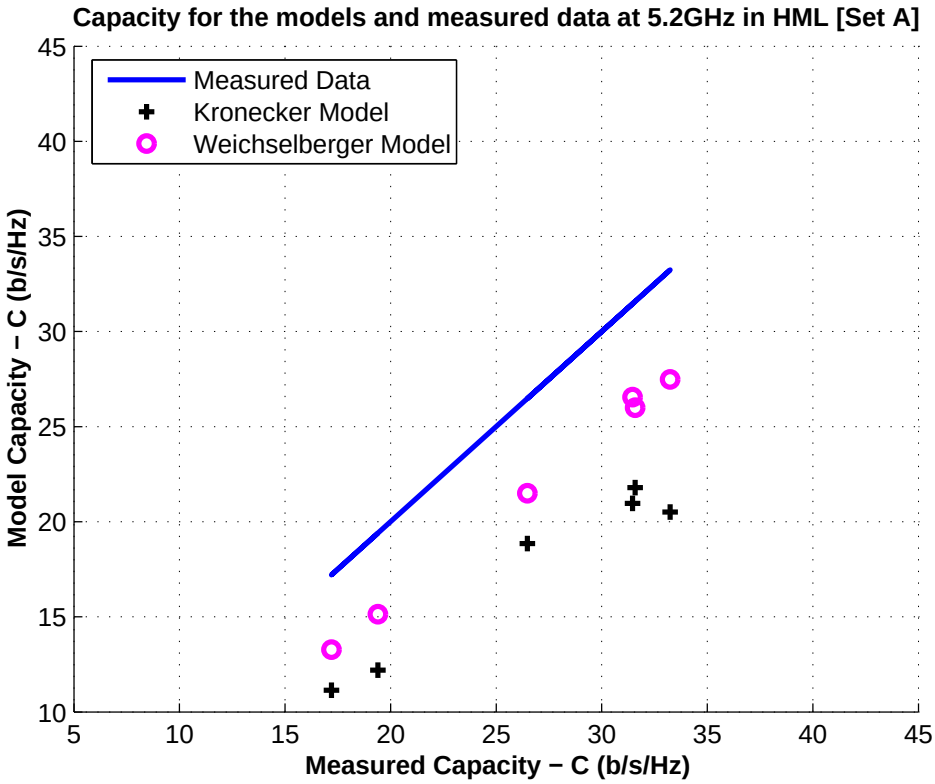

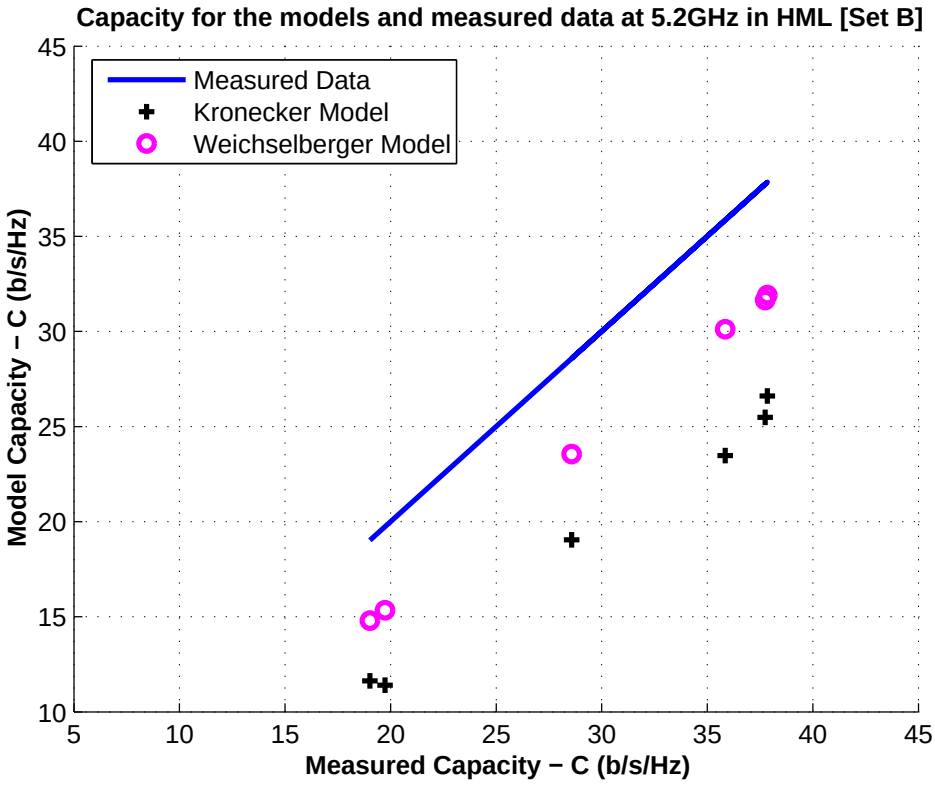

FIGURE 6.6: Average capacities for the models in HML at 5.2 GHz for Set A and Set B respectively.

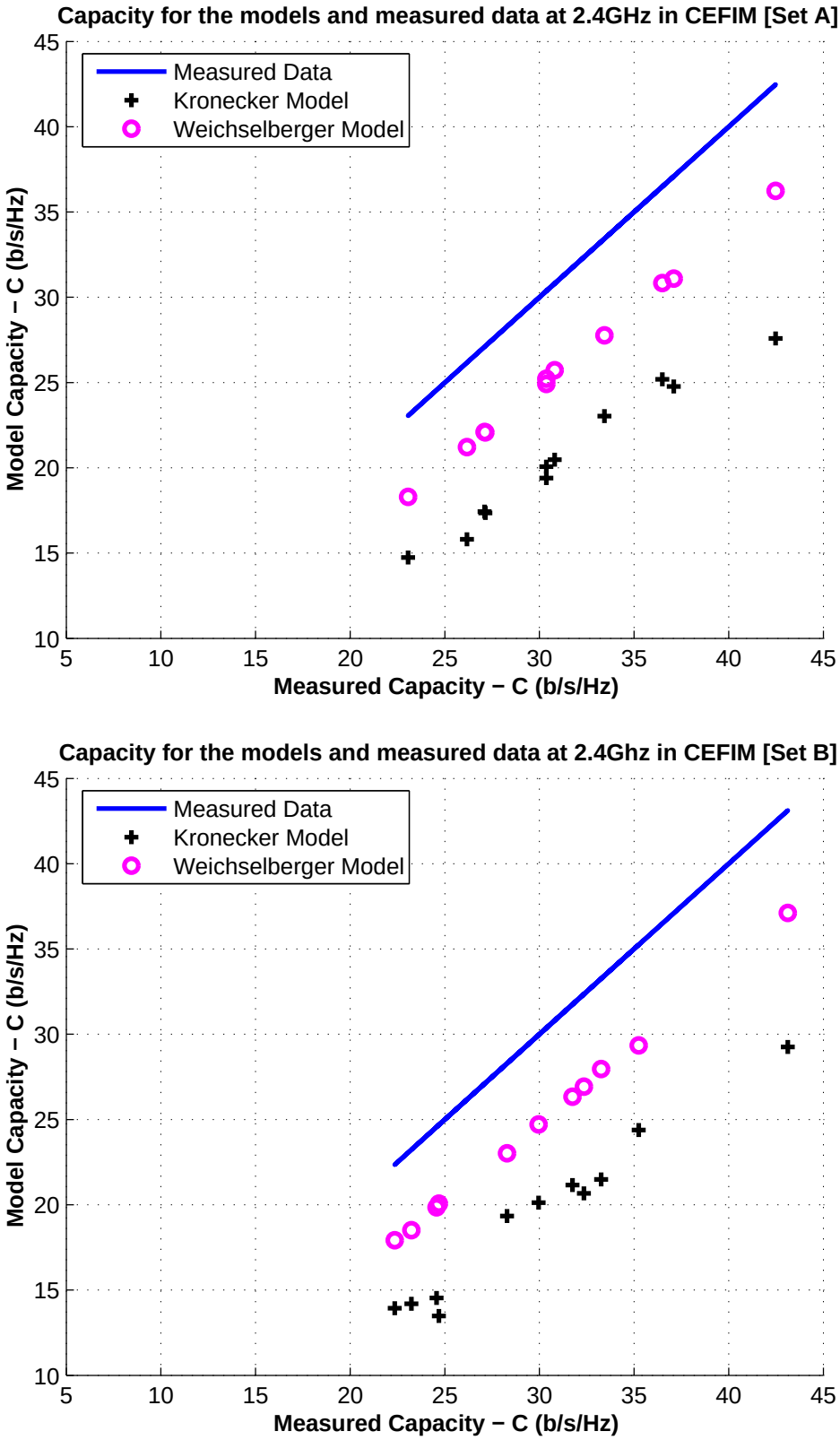

FIGURE 6.7: Average capacities for the models in CEFIM at 2.4 GHz for Set A and Set B respectively.

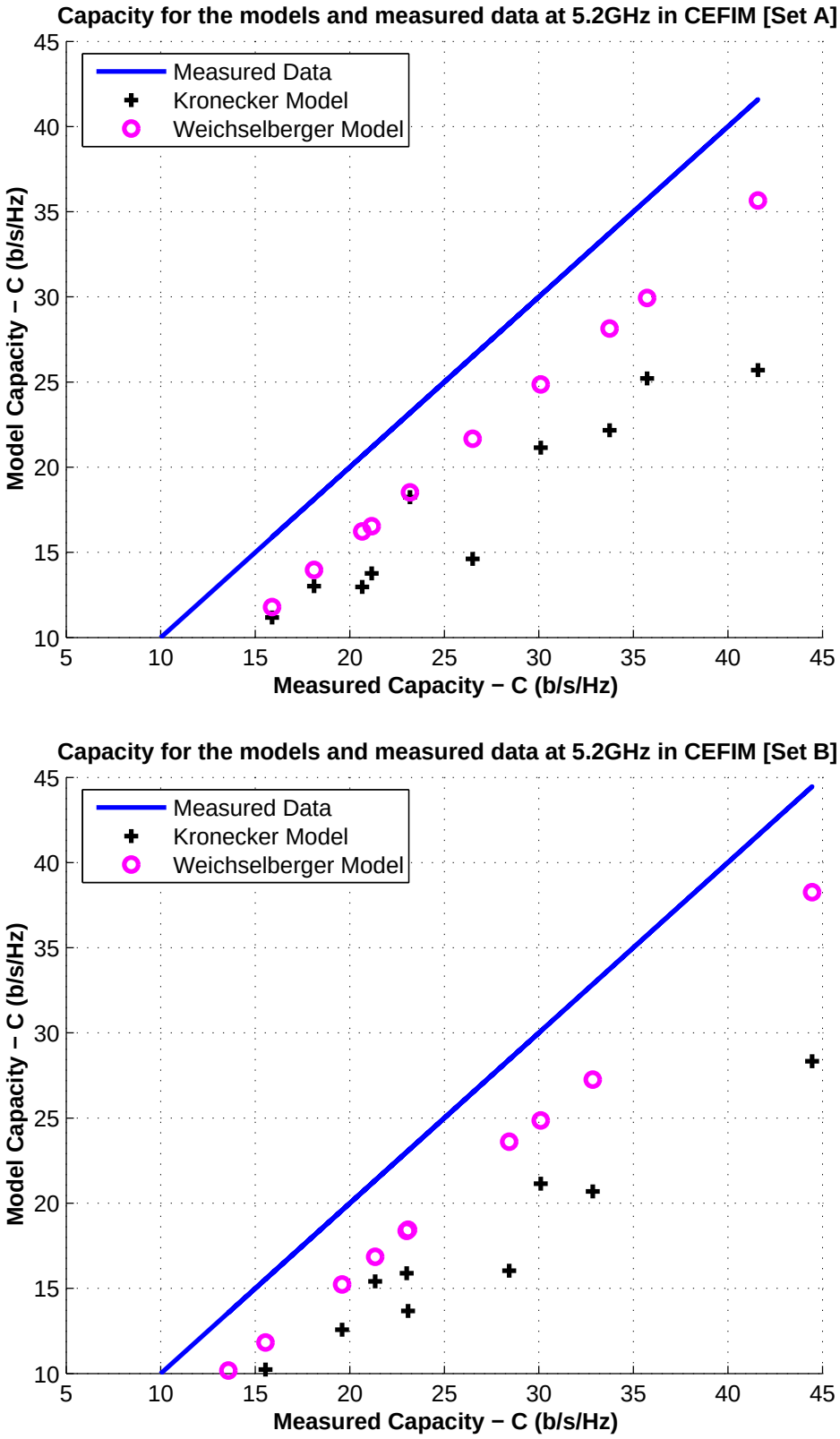

FIGURE 6.8: Average capacities for the models in CEFIM at 5.2 GHz for Set A and Set B respectively.

CHAPTER SEVEN
CONCLUSION

The study in this dissertation involved using the data of a measurement campaign to characterize the MIMO channel in two distinct environments.

An 8×8 dual-pol MIMO system employing patch antennas was used to carry out measurements at 2.4 GHz and 5.2 GHz in an office and industrial environment at the University of Pretoria. The office measurements were conducted in CEFIM (Carl and Emily Fuchs Institute of Microelectronics), while the industrial measurements were conducted in HML (Heavy Machinery Lab). In CEFIM, the measurements were taken at eleven receiver locations, while in HML, measurements were taken at six receiver locations. The channel matrices from the measurements, within a 30 MHz bandwidth and with a reference SNR of 20 dB, were used for the capacity computations.

The channel matrices were normalized for the entire environment (of a specific environment) using the co-polar channel matrices. To determine the suitability of the dual-pol MIMO system in both environments, three 4×4 subsystems were extracted from the 8×8 channel matrix represents the single-polarization matrices namely H-pol and V-pol, and the dual-pol matrices. The capacities for each of the subsystems in both environments were determined. The eigenvalues of the channels were also analyzed and to determine the robustness of the systems, the ratio between the dominant eigenvalues were determined. Considering that measurements were taken at two center frequencies, the relationship between the capacities between the two frequencies were established to determine whether frequency scaling could be applied. The final analysis of the study involved modeling the data using two analytical models namely the Kronecker and Weichselberger models.

The summary of the results of the above-mentioned campaign is discussed below.

7.1 SUMMARY OF THE RESULTS

The average capacities in CEFIM and HML were found to be between 45% and 70% of the ideal maximum, indicating somewhat reduced channel quality compared to an ideal i.i.d. Gaussian channel. The results were similar for both CEFIM and HML.

In terms of increasing average capacity performance, the subsystems could be ranked as: H-pol, dual-pol, and V-pol. The dual-pol system does not perform better than the single-pol systems, as would have been expected. This could possibly be attributed to the fact that when analyzing the eigenvalue distributions, the dual-pol system exhibits a power loss relative to the single-pol system, basically offsetting the increased capacity from improved channel conditioning.

The robustness of single- versus dual-pol systems with respect to a changing environment was studied by looking at the eigenvalue spacing of the first two channel eigenvalues. Results indicate a 10-20 dB reduction in the spacing when dual polarization is employed, suggesting that dual-polarization does offer an advantage over single-pol systems, and is a good candidate for demanding industrial applications.

The capacities of the orientations and polarizations in both HML and CEFIM appear to not be significantly different. Considering also that channel ranks of up to 3 can be achieved in certain locations, it could suggest that both environments are sufficiently richly scattered.

Although capacities in both CEFIM and HML were found to be similar, the results of the capacities at 2.4 GHz and 5.2 GHz suggest that the nature of the scattering is important. The HML environment was found to be more reflective because performance at 5.2 GHz was slightly better than that at 2.4 GHz, while the CEFIM environment was found to be more absorptive because performance at 2.4 GHz was slightly better than that at 5.2 GHz. The low correlation between the two frequencies in both environments suggest that frequency scaling cannot be applied using linear dual- or single-polarized patch antennas and is dependent on the antenna type used.

The Weichselberger model performed better than the Kronecker model in terms of average capacity, but it also fits the measured data poorly. The Kronecker model has been known to perform poorly for large antenna sizes [51]. The performance of the Weichselberger model could be attributed to certain parts of the channel not fading enough and thus the zero-mean Gaussian assumption does not hold.

7.2 FUTURE WORK

As this is the first work of this kind (to the author's knowledge), concerning the the use of polarization diversity and the modeling of the channel using analytical models, conducted in an industrial environment , the results that have been obtained cannot be generalized. Thus more work needs to be done both in terms of measurement analysis and modeling of the indoor industrial channel.

In terms of the work involved in this study, it was found that for the eigenvalue analysis of the 4×4 subsystems, only two dominant eigenvalues existed. Perhaps more studies can be done using 2×2 subsystems, as there are only two "good" channels, and it could allow for better averaging. In terms of the metrics that were looked at, the focus of the study was on capacity. Therefore other metrics could be determined for both the comparisons between the two environments and for the modeling.

7.3 CONCLUDING REMARKS

The analysis of the work done in this dissertation drew on work that already exists in literature. However, investigation of the performance of the single- and dual-polarized MIMO systems in the industrial environment, and consequently the comparison with the performances in the office environment, provide new insights into the operation of MIMO systems in such environments. The computation of actual capacities that can be attained and the modeling of the measured data enable us to understand the nature of the scattering and propagation of the signals within each environment. Considering that most previous measurement studies have been conducted in indoor office environments, the results from this study will broaden the generalization of the existing studies.

REFERENCES

[1] I. Brodsky. (2005, June 1) Using MIMO-OFDM Technology to Boost Wireless LAN Performance Today. [Online]. Available: www.datacommresearch.com/Whitepapers/Downloads/MIMO-OFDM_for_Wireless_LANs_White_Paper_1.0.pdf

[2] A. Paulraj, D. Gore, R. Nabar, and H. Bolcskei, "An Overview of MIMO Communications A Key to Gigabit Wireless," *Proc. IEEE*, vol. 92, pp. 198–218, Feb. 2004.

[3] A. Molisch. (2004, June 17) Recent Results in MIMO Channel Measurement and Modeling. [Online]. Available: http://www.s2.chalmers.se/costworkshop/tutorial_mimo/molisch.pdf

[4] P. Almers, E. Bonek, A. Burr, N. Czink, M. Debbah, V. Degli-Esposti, P. Kyosti, D. Laurenson, G. Matz, A. Molisch, C. Oestges, and H. Özcelik. (2006, Nov. 15) Survey of Channel and Radio Propagation Models for Wireless MIMO Systems. [Online]. Available: http://www.eurecom.fr/util/popuppubli.fr.htm?page=detail&id=2162

[5] A. Molisch, "A Generic Model for MIMO Wireless Propagation Channels," *IEEE Trans. Signal Processing*, vol. 52, pp. 61–71, Jan. 2004.

[6] D. Gesbert, H. Bölcskei, D. Gore, and A. Paulraj, "MIMO Wireless Channels: Capacity and Performance Prediction," in *Proc. 2004 IEEE 15th Intl. Symp. on Personal, Indoor and Mobile Radio Comm.*, Nov. 2004, pp. 1827–1831.

[7] W. Weichselberger, M. Herdin, H. Özcelik, and E. Bonek, "A Stochastic MIMO Channel Model with Joint Correlation of Both Link Ends," *IEEE Trans. Wireless Commun.*, vol. 5, pp. 90–100, Jan. 2006.

[8] A. Sayeed, "Deconstructing Multiantenna Fading Channels," *IEEE Trans. Signal Processing*, vol. 50, pp. 2563–2579, Oct. 2002.

[9] D. Hampicke, A. Richter, A. Schneider, G. Sommerkorn, R. Thomä, and U. Trautwein, "Characterization of the Directional Mobile Radio channel in Industrial Scenarios, Based on Wide-Band Propagation Measurements," in *Proc. 1999 IEEE Fall Veh. Technol. Conf.*, Sept. 1999, pp. 2258–2262.

[10] R. S. Thomä, D. Hampicke, A. Richter, G. Sommerkorn, A. Schneider, U. Trautwein, and W. Wirnitzer, "Identification of Time-Variant Directional Mobile Radio Channels," *IEEE Trans. Instrum. Meas.*, vol. 49, pp. 357–364, Apr. 2000.

[11] J. Karedal, S. Wyne, P. Almers, F. Tufvesson, and A. Molisch, "UWB Channel Measurements in an Industrial Environment," in *Proc. 2004 IEEE Global Telecomm. Conf.*, Nov-Dec 2004, pp. 3511–3516.

[12] S. Kjesbu. (2001, Oct. 30) Radio Wave Propagation in Industrial Environments. [Online]. Available: http://www.stanford.edu/group/wcs/KjesbuTalk.pdf

[13] T. Rappaport, *Wireless Communications Principles and Practice*, 2nd ed. Upper Saddle River, New Jersey: Prentice Hall, 2002, ch. 4, pp. 157–158.

[14] M. Khalighi, K. Raoof, and G. Jourdain, "Capacity of Wireless Communication Systems Employing Antenna Arrays, A Tutorial Study," *Wireless Personal Commun.*, vol. 23, pp. 321–352, Dec. 2002.

[15] I. Teletar, "Capacity of Multi-antenna Gaussian Channels," *European Trans. on Commun.*, vol. 6, pp. 585–585, Nov. 1998.

[16] G. J. Foschini and M. J. Gans, "On Limits of Wireless Communications in a Fading Environment when Using Multiple Antennas," *Wireless Personal Commun.*, vol. 6, pp. 311–335, Mar. 1998.

[17] S. Schindler. (2006, June 13) Introduction to MIMO Systems. [Online]. Available: http://www.rohde-schwarz.com

[18] B. Holter, "On the Capacity of the MIMO Channel - A Tutorial Introduction," in *Proc. of the IEEE Norwegian Symp. on Signal Processing*, Oct. 2001, pp. 167–172.

[19] A. Goldsmith, S. Jafar, N. Jindal, and S. Vishwanath, "Capacity Limits of MIMO Channels," *IEEE J. Selected Areas Commun.*, vol. 21, pp. 684–702, June 2003.

[20] Nortel. (2007, March 10) MIMO Technology. [Online]. Available: http://www.nortel.com/mimo

[21] J. Proakis and M. Salehi, *Communication Systems Engineering*, 2nd ed. Upper Saddle River, New Jersey: Prentice Hall, 2002, ch. 6, pp. 267–285.

[22] M. Jensen and J. Wallace, "A Review of Antennas and Propogation for MIMO Wireless Communications," *IEEE Trans. Antennas Propag.*, vol. 52, pp. 2810–2824, Nov. 2004.

[23] R. Nabar, V. Erceg, H. Bölcskei, and A. Paulraj, "Performance of Multi-Antenna Signaling Strategies Using Dual-Polarized Antennas: Measurement Results and Analysis," *IEEE Trans. Signal Processing*, vol. 23, pp. 31–44, Oct. 2002.

[24] R. Best. (2002, Sept. 23) Antenna Polarization Considerations in Wireless Communications Systems. [Online]. Available: http://www.cushcraft.com/comm/support/pdf/Antenna-Polarization-14B32.pdf

[25] V. R. Anreddy and M. A. Ingram, "Capacity of Measured Ricean and Rayleigh Indoor MIMO Channels at 2.4 GHz with Polarization and Spatial Diversity," vol. 2, 3-6 Apr. 2006, pp. 946–951.

[26] C. Degen and W. Keugsen, "Performance Evaluation of MIMO Systems Using Dual-Polarized Antennas," in *Proc. IEEE 10th Intl. Conf. on Telecomms*, Mar. 2003, pp. 1520–1525.

[27] J. Wallace and M. Jensen, "Modeling the Indoor MIMO Wireless Channel," *IEEE Trans. Antennas Propag.*, vol. 50, pp. 591–599, May 2002.

[28] H. Bölcskei, R. U. Nabar, V. Erceg, D. Gesbert, and A. J. Paulraj, "Performance of Spatial Multiplexing in the Presence of Polarization Diversity," in *Proc. 2001 IEEE Intl. Conf. Acoustics, Speech, and Signal Processing*, May 2001, pp. 2437–2440.

[29] J. Wallace and M. Jensen, "Characteristics of Measured 4x4 and 10x10 MIMO Wireless Channel Data at 2.4 GHz," in *Proc. 2001 IEEE Antennas and Propag. Society Intl. Symp.*, July 2001, pp. 96–99.

[30] Q. Huang and X. Shi, "Channel Capacity of Indoor MIMO Systems in the Presence of Polarization Diversity," in *Proc. IEEE 2005 Asia-Pacific Microwave Conf.*, Dec. 2005, pp. 4–8.

[31] J. Valenzuela-Valdés, M. García-Fernández, A. Martínez-González, and D. Sánchez-Hernández, "The Role of Polarization Diversity for MIMO Systems Under Rayleigh-Fading Environments," *IEEE Commun. Lett.*, vol. 5, pp. 534–536, Nov. 2006.

[32] P. Kyritsi, D. Cox, R. Valenzuela, and P. Wolniansky, "Effect of Antenna Polarization on the Capacity of a Multiple Element System in an Indoor Environment," *IEEE J. Selected Areas Commun.*, vol. 20, pp. 1227–1239, Aug. 2002.

[33] A. González and B. Lindmark, "The Effect of Antenna Orientation and Polarization on MIMO Capacity," in *Proc. 2005 IEEE Antennas and Propag. Society Intl. Symp.*, July 2005, pp. 434–437.

[34] D. G. Landon and C. M. Furse, "Recovering Handset Diversity and MIMO Capacity with Polarization-Agile Antennas," *IEEE Trans. Antennas Propag.*, vol. 55, pp. 3333–3340, Nov. 2007.

[35] A. Pal, B. S. Lee, P. Rogers, G. Hilton, M. Beach, and A. Nix, "Effect of Antenna Element Properties and Array Orientation on Performance of MIMO Systems," in *Proc. Intl. Symp. on Wireless Communications*, Sept. 2004, pp. 120–124.

[36] W. Kotterman, G. Sommerkorn, and R. Thomä, "Cross-Correlation Values for Dual-Polarised Indoor MIMO Links and Realistic Antenna Elements," in *Proc. Intl. Symp. on Wireless Communications*, Sept. 2006, pp. 505–509.

[37] P. Goud Jr., C. Schlegel, W. Krzymien, R. Hang, Z. Bagely, S. Messerly, M. Nham, and V. Rajamani, "Indoor MIMO Channel Measurements Using Dual Polarized Patch Antennas," in *Proc. 2003 IEEE Pacific Rim Conf. on Communications, Computers and Signal Processing*, Aug. 2003, pp. 752–755.

[38] A. Molisch, M. Steinbauer, M. Toeltsch, E. Bonek, and R. Thomä, "Measurement of the Capacity of MIMO Systems in Frequency-Selective Channels," in *Proc. 2001 IEEE 53rd Veh. Technol. Conf.*, May 2001, pp. 204–208.

[39] J. Nielsen, J. Andersen, P. Eggers, G. Pedersen, K. Oelsen, and H. Suda, "Measurements of Indoor 16x32 Wideband MIMO Channels at 5.8 GHz," in *Proc. IEEE 8th Intl. Symp. on Spread Spectrum Techniques and Applications*, Sept. 2004, pp. 864–868.

[40] H. Xu, D. Chizhik, H. Huang, and R. Valenzuela, "A Wave-Based Wideband MIMO Channel Modelling Technique," in *Proc. 2002 IEEE 13th Intl. Symp. on Personal, Indoor and Mobile Radio Comm.*, Sept. 2002, pp. 1626–1630.

[41] J. Kermoal, L. Schumacher, P. Mogensen, and K. Pedersen, "Experimental Investigation of Correlation Properties of MIMO Radio Channels for Indoor Picocell Scenarios," in *Proc. 2000 IEEE 52nd Veh. Technol. Conf.*, Sept. 2000, pp. 14–21.

[42] K. Yu, M. Bengsston, B. Ottersten, D. McNamara, P. Karlsson, and M. Beach, "Second Oorder Statistics of NLOS Indoor MIMO Channels Based on 5.2 GHz Measurements," in *Proc. 2001 IEEE Global Telecomm. Conf.*, Nov. 2001, pp. 156–160.

[43] ——, "A Wideband Statistical Model for NLOS Indoor MIMO Channels," in *Proc. 2002 IEEE 55th Veh. Technol. Conf.*, May 2002, pp. 370–374.

[44] H. Nguyen, J. Andersen, and G. Pedersen, "A Stochastic Model for the Spatio-Temporally Correlated Narrowband MIMO Channel Based on Indoor Measurements," in *Proc. 2004 IEEE 15th Intl. Symp. on Personal, Indoor and Mobile Radio Comm.*, Sept. 2004, pp. 1827–1831.

[45] D. Gesbert, M. Shafi, D.-S. Shui, P. Smith, and A. Naguib, "From Theory to Practice: An Overview of MIMO Space-time Coded Wireless Systems," *IEEE J. Selected Areas Commun.*, vol. 21, pp. 281–302, Apr. 2003.

[46] J. Wallace and M. Jensen, "Statistical Characteristics of Measured MIMO Wireless Channel Data and Comparison to Conventional Methods," in *Proc. 2001 IEEE 54th Veh. Technol. Conf.*, Oct. 2001, pp. 1078–1082.

[47] C. Oestges, V. Erceg, and A. Paulraj, "A Physical Scattering Model for MIMO Macrocellular Broadband Wireless Channels," *IEEE J. Selected Areas Commun.*, vol. 21, pp. 721–729, June 2003.

[48] A. Saleh and R. Valenzuela, "A Statistical Model for Indoor Multipath Propagation," *IEEE J. Selected Areas Commun.*, vol. 5, pp. 128–137, Feb. 1987.

[49] K. Pedersen, J. Andersen, J. Kermoal, and P. Mogensen, "A Stochastic Multiple-Input-Multiple-Output Radio Channel Model for Evaluation of Space-Time Coding Algorithms," *IEEE Trans. Wireless Commun.*, vol. 4, pp. 893–905, May 2000.

[50] D. Shui, G. Foschini, M. Gans, and J. Kahn, "Fading Correlation and its Effect on the Capacity of Multielement Antenna Systems," *IEEE Trans. Commun.*, vol. 48, pp. 502–513, Mar. 2000.

[51] R. Stridh, K. Yu, B. Ottersten, and P. Karlsson, "MIMO Channel Capacity and Modeling Issues on a Measured Indoor Radio Channel at 5.8 GHz," *IEEE Trans. Wireless Commun.*, vol. 4, pp. 895–903, May 2005.

[52] H. Özcelik, M. Herdin, W. Weichelberger, J. Wallace, and E. Bonek, "Deficiencies of Kronecker MIMO Radio Channel Model," *Electronics Letters*, vol. 29, pp. 1209–1210, Aug. 2003.

[53] E. Bonek. (2005, June 6) Experimental Validation of Analytical MIMO Channel Models. [Online]. Available: http://publik.tuwien.ac.at/files/pub-et_10481.pdf

[54] H. Özcelik, N. Czink, and E. Bonek, "What Makes a Good MIMO Channel?" in *Proc. 2005 IEEE 61st Veh. Technol. Conf.*, May 2005, pp. 156–160.

[55] A. Burr, "Capacity Bounds and Estimates for the Finite Scatterers MIMO Wireless Channel," *IEEE J. Selected Areas Commun.*, vol. 21, pp. 812–818, June 2003.

[56] M. Debbah and R. Muller, "MIMO Channel Modeling and the Principle of Maximum Entropy," *IEEE Trans. Inf. Theory*, vol. 51, pp. 1667–1690, May 2005.

[57] Techincal Specification Group Radio Access Network, "Spatial Channel Model for Multiple Input Multiple Output (MIMO) Simulations," 3GPP TR 25.996, Tech. Rep., 2003-2009.

[58] V. Erceg, L. Schumacher, P. Kyritsi, A. Molisch, D. Baum, A. Gorokhov, C. Oestges, Q. Li, K. Yu, N. Tal, D. Dijkstra, A. Jagannatham, C. Lanzl, V. Rhodes, J. Medbo, D. Michelson, and M. Webster, "Tgn Channel Models," IEEE P802.11 Wireless LANs, Tech. Rep., 2004.

[59] B. Maharaj, L. Linde, J. Wallace, and M. Jensen, "A Cost-Effective Wideband MIMO Channel Sounder and Initial Co-Located 2.4 GHz and 5.2 GHz measurements," in *Proc. 2005 IEEE Intl. Conf. Acoustics, Speech, and Signal Processing*, March 2005, pp. 981–984.

[60] B. Maharaj, J. Wallace, and M. Jensen, "A Low-Cost Open-Hardware Wideband Multiple-Input Multiple-Output (MIMO) Wireless Channel Sounder," *IEEE Trans. Instrum. Meas.*, vol. 57, pp. 2283–2289, Oct. 2008.

[61] C. Oestges, V. Erceg, and A. J. Paulraj, "Propagation Modeling of MIMO Multipolarized Fixed Wireless Channels," *IEEE Trans. Veh. Technol.*, vol. 53, pp. 644–654, May 2004.

[62] J. Kermoal, P. Mogensen, S. Jensen, and J. Andersen, "Experimental Investigation of Multipath Richness for Multi-Element Transmit and Receive Antenna Arrays," in *Proc. 2000 IEEE 52nd Veh. Technol. Conf.*, Sept. 2000, pp. 2004–2008.

[63] N. Herscorici and C. Christodoulou, "On Eigenvalue Distribution of Smart-Antenna Arrays in Wirless Communication Systems," *IEEE Antennas and Propag. Magazine*, vol. 46, pp. 158–167, Aug. 2004.

[64] K. Sulonen, P. Suvikunnas, L. Vuokko, and P. Vainikainen, "Study of Different Mechanisms Providing Gain in Mimo Systems," in *Proc. 2000 IEEE 52nd Veh. Technol. Conf.*, Sept. 2003, pp. 352–356.

[65] B. Maharaj, J. Wallace, L. Linde, and M. Jensen, "Frequency Scaling of Spatial Correlation from Co-Located 2.4 and 5.2 GHz Wideband Indoor MIMO Cchannel Measurements," *Electronics Letters*, vol. 41, pp. 336–337, Mar. 2005.